UNIVERSITÀ DEGLI STUDI DI ROMA "TOR VERGATA"

FACOLTA' DI INGEGNERIA

DOTTORATO DI RICERCA IN
INGENERIA DEI MICROSISTEMI

XXII CICLO

SVILUPPO E APPLICAZIONE DI MICROSENSORI DI DIAMANTE CVD PER MISURE RADIOTERAPICHE

Salvatore Almaviva

A.A. 2009/2010

Docente Guida/Tutor: Prof. Enrico Milani

Coordinatore: Prof. Aldo Tucciarone

A Stefano e Michela

Index

INTRODUCTION **8**

Chapter 1 : OVERVIEW ON MICROSYSTEMS

1.1 MICROSYSTEMS: FROM THE ORIGINS TO NOWADAYS **11**
1.2 APPLICATION AND ADVANTAGES OF MICROSYSTEMS **13**
1.3 THE PHYSICS OF MICROSYSTEMS **15**
1.4 OVERWIEV OF MICROSYSTEMS FABRICATION PROCESSES **18**
1.5 MATERIALS INVOLVED IN MICROSYSTEMS FABRICATION **19**
1.6 BULK MICROMACHINING **22**
1.7 WET ETCHING **23**
1.8 DRY ETCHING **28**
1.9 WAFER BONDING **30**
1.10 SURFACE MICROMACHINING **31**
1.11 LAYER DEPOSITION **32**
1.12 DESIGN LIMITATIONS **34**
1.13 MICROSTRUCTURE RELEASE **36**
1.14 DRIE MICROMACHINING **38**
1.15 OTHER MICROFABRICATION TECHNIQUES **41**
1.16 POLYMER MEMS **42**
BIBLIOGRAPHY **43**

Chapter 2 : DIAMOND PROPERTIES AND GROWTH

2.1 INTRODUCTION **46**
2.2 DIAMOND STRUCTURE **46**
2.3 SOME CURRENT APPLICATIONS FOR DIAMOND **48**
2.3.1 Electronic applications **50**
2.3.2. Thermal and optical applications **50**
2.4 CVD DIAMOND GROWTH **53**
2.5 HIGH PRESSURE HIGH TEMPERATURE METHOD (HPHT) **54**
2.6 LOW PRESSURE GROWTH METHODS **55**
2.6.1 Hot Filament method **57**
2.6.2 Combustion Flame and Plasma Jet Deposition **58**
2.7 MICROWAVE PLASMA ENHANCED CVD **59**
2.7.1 Gas mixtures , C/H/O diagram and CVD diamond growth **61**
2.8 CVD DIAMONDS FOR MICROSYSTEMS **62**
BIBLIOGRAPHY **65**

Chapter 3 : DOSIMETRIC PRINCIPLES QUANTITIES AND UNITS

3.1 INTRODUCTION **68**
3.2 PHOTON FLUENCE AND ENERGY FLUENCE **68**
3.3 KERMA **70**
3.4 CEMA **71**
3.5. ABSORBED DOSE **71**
3.6. STOPPING POWER **72**
3.7. RELATIONSHIPS BETWEEN DOSIMETRIC QUANTITIES **78**
3.7.1. Energy fluence and kerma (photons) **78**
3.7.2. Fluence and dose (electrons) **80**
3.7.3. Kerma and dose (charged particle equilibrium) **82**
3.7.4. Collision kerma and exposure **84**
3.8. CAVITY THEORY **85**

3.8.1. Bragg–Gray cavity theory **85**
3.8.2. Spencer–Attix cavity theory **86**
3.8.3. Considerations in the application of cavity theory to ionization chamber calibration and dosimetry protocols **89**
3.8.4. Large cavities in photon beams **91**
3.8.5. Burlin cavity theory for photon beams **92**
3.8.6. Stopping power ratios **94**
BIBLIOGRAPHY **96**

Chapter 4 : RADIATION DOSIMETERS

4.1.INTRODUCTION **98**
4.2. PROPERTIES OF DOSIMETERS **99**
4.2.1. Linearity **99**
4.2.2. Dose rate dependence **99**
4.2.3. Energy dependence **100**
4.2.4. Directional dependence **100**
4.2.5. Spatial resolution and physical size **101**
4.2.6. Readout convenience **101**
4.2.6. Convenience of use **101**
4.3. IONIZATION CHAMBERS DOSIMETRY SYSTEMS **102**
4.3.1. Chambers and electrometers **102**
4.3.2. Cylindrical (thimble type) ionization chambers **103**
4.3.3. Parallel-plate (plane-parallel) ionization chambers **104**
4.3.4. Brachytherapy chambers **105**
4.3.5. Extrapolation chambers **106**
4.4. FILM DOSIMETRY **106**
4.4.1. Radiographic film **106**
4.4.2. Radiochromic film **110**
4.5. SEMICONDUCTOR DOSIMETRY **111**
4.5.1. Silicon diode dosimetry systems **111**
4.5.2. MOSFET dosimetry systems **112**
4.6.OTHER DOSIMETRY SYSTEMS **114**
4.6.1. Alanine/electron paramagnetic resonance dosimetry system **114**
BIBLIOGRAPHY **115**

Chapter 5 : SYNTHETIC SINGLE CRYSTAL DIAMOND FOR RADIOTHERAPIC DOSIMETRY

5.1 INTRODUCTION **118**
5.2 SCD DOSIMETER FABRICATION **120**
5.3 DOSIMETRIC CHARACTERIZATION **122**
5.3.1 Preliminary tests **122**
5.3.2 Tests at San Filippo Neri Hospital **123**
5.4 APPLICATION IN A REAL IMRT PLAN **132**
5.5 EXPERIMENTAL DETAILS **133**
5.6 RESULTS **135**
BIBLIOGRAPHY **139**

Chapter 6 : CONCLUSIONS

CONCLUSIONS **141**

Ringraziamenti

Questa Tesi è stata svolta presso il Dipartimento di Ingegneria Meccanica dell'Università degli Studi di Roma "Tor Vergata". Essa è stata resa possibile grazie al supporto di tutto il personale che ha contribuito, direttamente o indirettamente, alla realizzazione del lavoro.

Un ringraziamento particolare va al Prof. Aldo Tucciarone, al Prof. Enrico Milani, al Prof. Marco Marinelli e al Dott. Gianluca Verona Rinati per avermi pazientemente introdotto nel campo dei microsistemi e della fisica del diamante in particolare, aiutandomi ad affrontare una materia per me nuova che, fondendo in maniera inscindibile teoria ed esperimento, mi ha consentito di acquisire nuove conoscenze da utilizzare nelle mie attività future. Il Loro supporto scientifico continuo ha contribuito in maniera essenziale allo svolgimento di questo lavoro di Tesi,

Un ringraziamento sentito va anche all'Ing. Mario Pillon e al Dott. Maurizio Angelone del Centro Ricerche ENEA di Frascati per l'insostituibile disponibilità a proposito delle misure con neutroni termici e veloci effettuate al generatore FNG (Frascati Neutron Generator) e al reattore a fusione nucleare JET (Joint European Torus) sito in Culham (Oxford, UK). Sebbene l'applicazione illustrata in questa tesi esuli dalla collaborazione sviluppata con loro, il loro supporto ha contribuito in maniera considerevole a creare le premesse per l'ottenimento dei risultati raggiunti nello sviluppo del detector qui discusso.

Ulteriori ringraziamenti vanno alla D.ssa Rosa Maria Montereali del Centro ricerche ENEA di Frascati e al suo staff, che hanno sempre manifestato interesse per questa attività di ricerca e hanno contribuito alla realizzazione di alcuni dispositivi per la rivelazione dei neutroni termici e veloci e alle D.sse Isabella Ciancaglioni e Rita Consorti, per il loro entusiasmo e dinamicità che hanno reso possibili i test dei dispositivi presso L'Ospedale San Filippo Neri di Roma.

Infine, un ringraziamento a tutte le persone che mi sono state vicine nel periodo di svolgimento del Dottorato, ai miei genitori *in primis* e ai colleghi Dott. Claudio Verona, Ing. Giuseppe Prestopino, che mi hanno aiutato a maturare non solo dal punto di vista scientifico ma anche (e forse soprattutto) dal punto di vista umano. Questo lavoro è per tutti Voi, con gratitudine.

INTRODUCTION

The development of microelectronics based on the concept of “smaller and smaller” has been enabled from the evolution of the lithographic techniques currently used for the production of electronic circuits and has found its fundamentals in the silicon physical properties. This development led to the opportunity of integrating microelectronics technologies with those used to obtain mechanical, chemical, biological, optical components and so on, opening the possibility to realize smaller and more complex structures capable to perform more sophisticated functions, usually task of bigger dimensions systems.

Usually the word “microsystem” is used to define complex systems able to perform the functions of sensor, analyzer and actuator in several fields (electronics, mechanics, chemistry, biology and so on). These complex systems integrate different kinds of technologies in mechanical, electronic, informatic engineering and so on. A microsystems is thus a miniaturized system, of the same dimensions of electronic microcircuits (and smaller and smaller in future) made of sensors who detect and measure various kinds of physical quantities by means of highly integrated electronic circuits.

The signal obtained is sent to the actuator which gives the desired function.

It should be stated that each of the three main parts (sensor, analyzer and actuator) can be a microsystem itself. To this respect, one of the major current challenge consists in reaching an higher integration and interconnection among the various parts that often have very different needs.

In conclusion, the main characteristics of a microsystem must be the reduced size, an higher reliability, a considerable integration among the various parts, low cost and ease of use. The development of this systems requires first an high knowledge of microtechnologies and then multidisciplinar knowledge in various fields for which the microsysem is thought.

The current line is to realize these structures starting from well known physical principles properly adapted to the particular needs and requests using or developing "*ad hoc*" technologies. Nowadays the utilization of silicon substrates remains fundamental for the realizations and applications of a large number microsystems. Silicon microsystems have large use in automotive, in biology and in mechanics. Nevertheless the employment of silicon strictly reduce some possible applications. It is well known infact that silicon has remarkable mechanic and electric properties but presents a lot of problems in harsh environments applications like, for example, corrosive environments, high temperature environments, high radiation fields environments and so on. This problems impose severe limits to the use of silicon-based microsystems precisely where they would be very useful. It is thus necessary to study new materials that can overcome these limitations having superior electric and mechanic properties while remaining easily handled for the purposes of realization of microsystems. One of the materials to be consider alternative to silicon is synthetic diamond, particularly in the form of thin films produced with the CVD *(Chemical Vapour Deposition*) technique.

This thesis is part of the activities of production and development of synthetic diamond films produced by CVD technique, conducted at the Department of Mechanical Engineering of the University "Tor Vergata" of Rome. These activities specifically include the production and development of different types of microsensors to be applied in various fields.

The work presented an overview of activities carried out during the reference period (2006-2009) for the course of Ph.D. in microsystems technology, 22^{th} cycle. The thesis is divided into five chapters, the first is devoted to discuss briefly the meaning of the term microsystem and the production techniques of silicon microsystems.

In chapter 2 is then introduced the physics and properties of diamond, both natural and artificial, comparing the latter to those of silicon. It is also reported the various techniques

of production and growth of artificial diamonds in particular with regard to CVD (Chemical Vapor Deposition) technique and some recent examples of synthetic diamond based microdevices. In the third chapter it is shown the physical principles of dosimetry in radiotherapy thus deepening the theoretical basis that underpins the principles of operation of the devices used in this area. Chapter four is devoted to current detectors used in radiotherapy dosimetry, highlighting the advantages that may offer the synthetic diamond as based material for such devices. Chapters five reports the actual activities conducted during the three years of the PhD program. The work can be divided into two parts which practically coincide with the chronological order of the conducted activities . In fact during the first two years the job has been primarily directed towards the study of growth parameters of CVD diamond, the optimization of the device geometry and the improvement of the electronic properties, convinced that only a significant deepening of these aspects may lead to the effective use of the device in radiotherapy. In the third year the activity has focused on the realization of several prototypes, testing their actual capabilities such radioterapic dosimeters and comparing their performances with those of commercially available devices specifically designed for that use.

Chapter 1

OVERVIEW ON MICROSYSTEMS

1.1 MICROSYSTEMS: FROM THE ORIGINS TO NOWADAYS

The term microsystem identifies micro miniaturized systems consisting of sensors that reveal and measure quantities of various kinds (physical, chemical, biological etc.) thereby producing a signal that is properly prepared with the integrated electronic sensor system (control-preparation system) and then sent to an actuator that performs the command wanted. The control system may be a software, a set of software-hardware, both internal and external to the microsystem and able to control the various parts and functions of the microsystem, performing, if requested, feedback functions both on the sensor and on the actuator. Key feature of the microsystem is to have the three functions of sensor, processing and implementation of integrated control in a single element. Each of the various functions can in turn be performed by a micro very small on the scale of the most integrated electronic circuits. It is not a coincidence, in fact, that the technology for the realization of microsystems has developed from the technologies of miniaturization of electronic circuits and components and then use as base material silicon.The history of microsystems and their development is in practice recently, having occurred mainly in the last twenty - twenty five years. On the other hand, the idea of establishing systems of various kinds and for various uses dates back to the early fifties of last century. In 1959, during the meeting of the American Physical Society (APS), the Nobel prize R. Feynman gave a famous speech ("There's Plenty of Room at the Bottom") during which he stated that in principle there was no physical reason that prohibited to realize and operate the systems with dimensions of atomic or molecular scale.

In this speech Feynman also raised what microsystems could be, why they were needed, what technologies to use to build them, and especially pointed out how the physics of cars made at the microscopic level was different from the physics of machines operating at the macroscopic level.

From a practical point of view it was in 1966 that the technology of selective etching began to be used to realize tridimensional microsensors.

In the early seventies this technique became known as "micromachining" (today is used the term "bulk micromachining") that was used for the production of diagnostic neural, pressure sensors and other kind of microsystems. In the early seventies also the technique of "wafer bonding" began to be used to create three-dimensional structures. In the early eighties was introduced the technique of "sacrificial etching" to obtain surface treatments (surface-micromachined) that have allowed the development of new sensors and microactuators. In recent years there has been a strong development of techniques of integration of the various parts constituent the microsystems [1,2] (sensors, microactuators and electronic circuits) on a single silicon substrate. These efforts have produced ever-smaller devices, reliable and economical.

1.2 APPLICATION AND ADVANTAGES OF MICROSYSTEMS

The microsystems are now widely applied in autronics (think of lambda sensors for the muffler's catalysts or pressure microsensors for air-bags), in mechanics and robotics (realization of microsystems that can perform operations in parts otherwise inaccessible [3], in biology, medicine (it is recently introduced in Britain the use of a microsystem with a CCD camera, the overall size of 8-10 mm to perform endoscopies, see e.g. [3].), in agriculture, environmental monitoring, not to mention the many and certainly not advertised applications in military field. The latter is the study of microsystems, the size of a button or even less, which are real biological laboratories to be used on the uniforms of the soldiers to signal the presence of toxic elements in the event of biological and / or chemical warfare (studies in progress at the Livermore laboratories U.S. [4]), the study of microsatellite spy, who would also have the advantage of not requiring especially costly carriers for the placement in orbit. The use of microsystems therefore offers a number of

advantages both in terms of applicative and economic point of view. The benefits derived from the concept of microsystem that allows to integrate functions that otherwise would need completely different equipment dimensions. Think about the various less invasive probes for medical diagnosis, or the various probes "smart" for the dose of insulin in diabetic patients. Turning to other areas we could quote the possibility to introduce micro-cameras in a pipeline that allow visual inspections of the same and possibly introduce microrobot able to perform micro-weldings [3]. Another advantage of microsystems is to have a flexible production. To this respect, few changes in the apparatus are often enough to make another microsystem with features and performances significantly different. All at very low costs because, for the production of microsystems, we typically use the methods and processes of microelectronics. One could go on the list of advantages and increasingly feasible applications of microsystems [5,6], however, just this huge and very recent development has revealed the limits of the current technology based on the use silicon. In particular, silicon, while having excellent physical, mechanical, electrical properties [7] presents serious problems when used in hostile environments, like, for example, intense radiation fields, high temperatures, and corrosive environments. These limits of silicon reduces the area of application of microsystems precisely where they would be more necessary. For this reason, new materials are being studied for the realization of microsystems and among them, synthetic diamond obtained through the so-called CVD (*Chemical Vapor Deposition*) technique seems to be one of the most promising in several applications. The development and implementation of CVD diamond films, the study of its physical properties and application in some fields such as measures of certain types of radiation used in radiotherapy are the subject of this thesis.

1.3 THE PHYSICS OF MICROSYSTEMS

The large decrease in size during miniaturization, that in some case can reach 1 or 2 orders of magnitude, has a tremendous impact on the behavior of microobject when compared to their larger size cousin. We are already aware of some of the most visible implications of miniaturization. Actually nobody will be surprised to see a crumb stick to the rubbed surface of a plastic rod, whereas the whole bread loaf is not. Everybody will tell that it works with the crumb and not with the whole loaf because the crumb is lighter. Actually it is a bit more complicated than that. The force that is attracting the crumb is the electrostatic force, which is proportional to the amount of charge on the surface of the crumb, which in turn is proportional to its surface. Thus when we shrink the size and go from the loaf to the crumb, we not only decrease the volume and thus the mass but we also decrease the surface and thus the electrostatic force. However, because the surface varies as the square of the dimension and the volume as the cube, this decrease in the force is relatively much smaller than the drop experienced by the mass. Thus finally not only the crumb mass is smaller, but, what is more important, the force acting on it becomes proportionally larger making the crumb really fly.

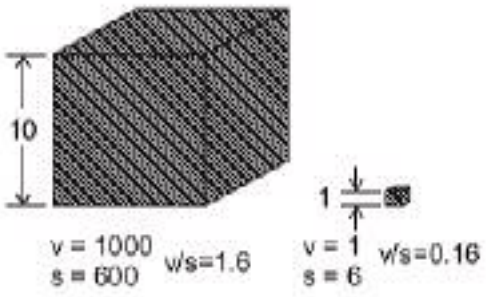

Fig. 1.1: Scaling effect on volume, surface and volume/surface ratio.

To get a better understanding, we can refer to Fig. 1.1 and consider a cube whose side goes from a length of 10 to a length of 1. The surface of the bigger cube is 6×10×10 =

600 whereas its volume is 10×10×10 = 1000. But now what happen to the scaled down cube? Its surface is 6×1×1 = 6 and has been divided by 100 but its volume is 1 × 1 × 1 = 1 and has been divided by 1000. Thus the volume/surface ratio has also shrunk by a factor of 10, making the surface effect proportionally 10 times larger with the smaller cube than with the bigger one. This decrease of volume/surface ratio has profound implications for the design of microsystems. Actually it means that at a certain level of miniaturization, the surface effect will start to be dominant over the volume effects. For example, friction force (proportional to surface) will become larger than inertia (proportional to mass hence to volume), heat dissipation will become quicker and heat storage reduced: energy storage will become less attractive than energy coupling...

Then of course we can dwell into a more elaborate analysis of nature laws and try to see apart from geometrical factor what happens when we shrink the scale? Following an analysis pioneered by W. Trimmer [8], we may describe the way physical quantities vary with scale as a power of an arbitrary scale variable, s. We have just seen that volume scale as s^3, surface as s^2 and the volume/surface ratio as s^1. In the same vein we may have a look at different forces and see how they scale down (Table 1.1).

Force	Scaling law
Surface tension	s^1
Electrostatic, Pressure, Muscle	s^2
Magnetic	s^3
Gravitational	s^4

Table 1.1: Scaling of nature forces.

From this table it appears that some forces that are insignificant at large scale becomes predominant at smaller scale. For example we see that gravity, which scales as s^4 (that is decrease by a factor 10,000 when the scale is shrunk by 10) will be relatively weak at

micro-scale. However a more favorable force will be the tension force, which decrease as s^1 making it an important (and often annoying for non-fluidic application) force at micro-scale. The table also reveals that the electrostatic force will become more interesting than the magnetic force as the scale goes down. Of course this simple description is more qualitative than quantitative. Actually if we know that as the size shrinks the electrostatic force will finally exceed the magnetic force, a more detailed analysis is needed to find if it is at a size of 100 μm, 1 μm or 10 nm. In that particular case it has been shown that the prediction becomes true when the dimensions reach a few μm, right in the scale of microsysetms devices. This has actually been the driver behind the design of the first electrostatic motors by R. Howe and R. Muller [9].

A more surprising consequence of miniaturization is that, contrary to what we would think at first, the relative manufacturing accuracy is sharply decreasing. This was first formalized by M. Madou [10] and it is indeed interesting to see that the relative accuracy of a microsystems device is at a few % not much better than standard masonry. Actually, if it is true that the absolute accuracy of microsystems patterning can reach 1 μm, the microsystems size is in the 10 μm-100 μm, meaning a relative patterning accuracy of 1%-10% or even less. We are here very far from single point diamond turning or the manufacturing of large telescope mirror that can both reach a relative accuracy of 0.0001%. So, ok, we have a low relative accuracy, but what does that mean in practice? Let's take as an example the stiffness of a cantilever beam. From solid mechanics the stiffness, k, depends on the beam cross-section shape and for a rectangular cross-section it is proportional to:

$$k = \frac{E}{4}\frac{h\omega^3}{L^3}$$

where E is the elasticity modulus, h is the beam thickness, ω its width and L its length. For a nominal beam width of 2 μm with an absolute fabrication accuracy of ±0.2 μm the

relative accuracy is ±10%. The stiffness for bending along the width direction varies as a power of 3 of the width and will thus have a relative accuracy of ±30%. For a stiffness nominal value of 1N/m, it means that the expected value can be anywhere between 0.7N/m and 1.3N/m – this is almost a variation by a factor of two! Our design needs to be tolerant to such variation, or the yield will be very low. In this particular case, one could improve the relative accuracy by taking advantage of the relatively constant absolute fabrication accuracy and increase the beam width nominal value to 4 μm - of course it also means doubling its length if one wants to keep the same spring constant.

1.4 OVERWIEV OF MICROSYSTEMS FABRICATION PROCESSES

Micro-fabrication is the set of technologies used to manufacture micro-sized structures. This task can unfortunately not rely on the traditional fabrication techniques such as milling, drilling, turning, forging and casting because of the scale. The fabrication techniques had thus to come from another source. As microsystems devices have about the same feature size as integrated circuits, their fabrication technology quickly took inspiration from microelectronics. Techniques like photolithography, thin film deposition by chemical vapor deposition (CVD) or physical vapor deposition (PVD), thin film growth by oxidation and epitaxy, doping by ion implantation or diffusion, wet etching, dry etching, etc. have all been adopted by the microsystems technologists. Standard book on microelectronics describe in details these techniques but, as microsystems and integrated circuits fabrication goals are different, some of these techniques have evolved as they were applied to microsystems and we will detail here their new capabilities. Moreover, microsystems has spurred many unique fabrication techniques that we will also describe in our panorama of microsystems fabrication introducing bulk micromachining, surface micromachining, LIGA, etc [11].

In general, microsystems fabrication tries to be a batch process to benefit from the same economy of scale that is so successful in reducing cost of ICs. As such, the fabrication process often starts with a wafer (silicon, polymer, glass...) that may play an active role in the final device or may only be a substrate on which the microsystems is built. This wafer is processed with a succession of processes that add, modify or remove selectively materials. A short classification of different techniques used in microfabrication is given in Table 1.2

Additive process	Modifying process	Substractive process
Evaporation	Oxydation	Wet etching
Sputtering	Doping	Dry etching
CVD	Annealing	Lift-off
Spin-coating	UV exposure	Development
...	...	...

Table 1.2: Process classification

1.5 MATERIALS INVOLVED IN MICROSYSTEMS FABRICATION

The choice of a good material for microsystems application is no more based like in microelectronics on carrier mobility, but on more mechanical aspect: small or controllable internal stress, low processing temperature, compatibility with other materials, possibility to obtain thick layer, patterning possibilities...

In addition, depending on the field of application, the material often needs to have extra properties. RF Microsystems will want to be based on material with small loss tangent (for example high resistivity silicon), optical microsystems may need a transparent substrate, Biomicrosystems will need bio-compatibility, if not for the substrate, for a coating adhering well to the substrate, sensor application will need a material showing piezoresistance or piezoelectricity, etc.

Actually, because the issue of material contamination is much less important in microsystems than in IC fabrication, the microsystems designer often tries to use the material presenting the best properties for his unique application. Still, from its microelectronics' root microsystems has retained the predominant use of silicon and its compounds, silicon (di)oxide (SiO2) and silicon nitride (SixNy). But actually, it was not purely coincidental, silicon is, as K. Petersen explained in a famous paper [12], an excellent mechanical material. Actually, silicon is almost as strong but lighter than steel, has large critical stress and no elasticity limit at room temperature as it is a perfect crystal ensuring that it will recover from large strain. Unfortunately it is brittle and this may pose problem in handling wafer, but it is rarely a source of failure for microsystems components. For sensing application silicon has a large piezoresitive coefficient, and for optical microsystems it is transparent at the common telecommunication wavelengths. In addition silicon has a stable oxide easy to grow at elevated temperature that is transparent and thermally and electrically insulating. Actually this oxide has the smallest coefficient of thermal expansion of all known materials. Those properties are often put to good use during microsystems fabrication, where oxide support will be used to thermally insulate a pixel of an thermal camera for example.

Recently, a new substrate based on silicon and coming from IC industry has made its entry in the microsystems material list: the SOI (Silicon On Insulator) wafer. This substrate is composed of a thick silicon layer of several hundred μm (the handle), a thin layer of oxide of 1 or 2μm and on top another silicon layer, the device layer. The thickness of this last layer is what differentiates the IC and the MEMS SOI wafers: in the first case it will reach at most a few μm where in the later case, the thickness can reach 100 μm or more.

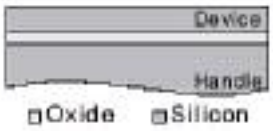

Fig. 1.2: Structure of SOI wafer.

The high functionality of this material has allowed producing complete devices with very simple process, like the optical switch produced by Sercalo fabricated with its mobile mirror, actuator and fiber alignment feature with one single process step!

Another interesting compound is silicon nitride (SixNy), which is stronger than silicon and can be deposited in thin layer with an excellent control of stress to produce 1 μm thick membrane of several cm2. In general stoichiometric nitride film (Si3N4) will show tensile stress, but increasing the Si content will invariably ends in obtaining a compressive stress. A good control of stress is also obtained during deposition of poly-crystalline silicon. During LPCVD deposition, increasing the temperature from 560_C to 620_C lowers the as-deposited stress, changing the compressive stress usually present in polysilicon films to tensile stress [13]. A subsequent high temperature (>950°C) anneal result in layer with very low stress, making Poly-Si the material of choice for building multi-layered structure on silicon surface. For example the Sandia National Lab's 'Summit V' process stacks five layer of poly-silicon allowing an unparalleled freedom of design for complex MEMS structure. Closing the list of silicon compound we can add a newcomer, silicon carbide SiC. SiC has unique thermal properties (albeit not yet on par with diamond) and has been used in high temperature sensor. But silicon and its derivative is not the only choice for MEMS, many other materials are also used because they posses some unique properties. For example, other semiconductors like InP have also been micromachined mainly to take advantage of their photonics capabilities and serve as tunable laser source. Quartz crystal has strong piezoelectric effect that has been

put into use to build resonant sensors like gyroscope or mass sensors. Biocompatibility will actually force the use of a limited list of already tested and approved material, or suggest the use of durable coating. Glass is only second to silicon in its use in MEMS fabrication because it can easily form tight bond with silicon and also because it can be used to obtain bio-compatible channels for BioMEMS. Polymers are also often used for BioMEMS fabrication where they can be tailored to provide biodegradability or bioabsorbability. The versatility of polymers makes them interesting for other MEMS application, and for example the reflow appearing at moderate temperature has been used to obtain arrays of spherical microlenses for optical MEMS. This thermoplastic property also allows molding, making polymer MEMS a cheap alternative to silicon based system, particularly for micro-fluidic application. Recently the availability of photosensitive polymers like SU8 [14] than can be spun to thickness exceeding 100µm and patterned with vertical sides has further increased the possibility to build polymer structure.This quick introduction to MEMS materials needs to mention metals. If their conductivity is of course a must when they are used as electrical connection like in IC, metals can also be used to build structures. Actually, their ability to be grown in thin-films of good quality at a moderate temperature is what decided Texas Instrument to base the complete DLP micro-mirror device on a multi-layer aluminum process. In other applications, electroplated nickel will produce excellent micro-molds, whereas gold reflective properties are used in optical MEMS and nitinol (NiTi), presenting a strong shape memory effect, becomes actuator.

1.6 BULK MICROMACHINING

Bulk micromachining refers to the formation of micro structures by removal of materials from bulk substrates. The bulk substrate in wafer form can be silicon, glass, quartz, crystalline Ge, SiC, GaAs, GaP or InP. The methods commonly used to remove

excess material are wet and dry etching, allowing varying degree of control on the profile of the final structure.

1.7 WET ETCHING

Wet etching is obtained by immersing the material in a chemical bath that dissolves the surfaces not covered by a protective layer. The main advantages of the technique are that it can be quick, uniform, very selective and cheap. The etching rate and the resulting profile depend on the material, the chemical, the temperature of the bath, the presence of agitation, and the etch stop technique used if any. Wet etching is usually divided between isotropic and anisotropic etching. Isotropic etching happens when the chemical etches the bulk material at the same rate in all directions, while anisotropic etching happens when different etching rate exists along different directions.

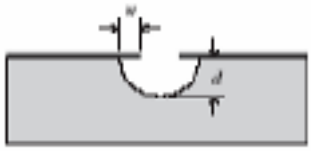

Fig. 1.3: Lateral and vertical etching.

However the etching rate never reaches 0, and it is actually impossible to obtain etching in only one direction. This is commonly quantified by estimating the overetch (w/d), that is the lateral etch with respect to the vertical etch, as shown in the Fig.. This parameter may range between 1 for isotropic etching to about 0.01 for very anistropic etch, obtained for example by etching Silicon in a KOH bath. For substrates made of homogeneous and amorphous material, like glass, wet etching must be isotropic, although faster surface etching is sometimes observed. However, for crystalline materials, e.g. silicon, the etching is either isotropic or anisotropic, depending on the type of chemical used. In general, isotropic etchants are acidic, while anisotropic etchants are alkaline.

Fig1.4 compares isotropic and anisotropic wet etching of silicon. The topleft inset shows isotropic etching of silicon when the bath is agitated ensuring that fresh chemical constantly reaches the bottom of the trench and resulting in a truly isotropic etch. Isotropic wet etching is used for thin layer or when the rounded profile is interesting, to obtain channels for fluids for example. For silicon, the etchant can be HNA, which is a mixture of hydrofluoric acid (HF), nitric acid (HNO_3), and acetic acid (CH_3COOH). In HNA the nitric acid acts as an oxidant and HF dissolves the oxide by forming the water soluble H_2SiF_6. The two steps of the simplified reaction are:

$$Si + HNO_3 + H_2O \rightarrow SiO_2 + HNO_2 + H_2$$

$$SiO_2 + 6HF \rightarrow H_2SiF_6 + 2H_2O$$

The etching rate for silicon can reach 80 μm/min, and oxide can be used as mask material as his etch rate is only 30 to 80 nm/min. Etching under the mask edge or underetch is unavoidable with isotropic wet etching. Moreover, the etch rate and profile

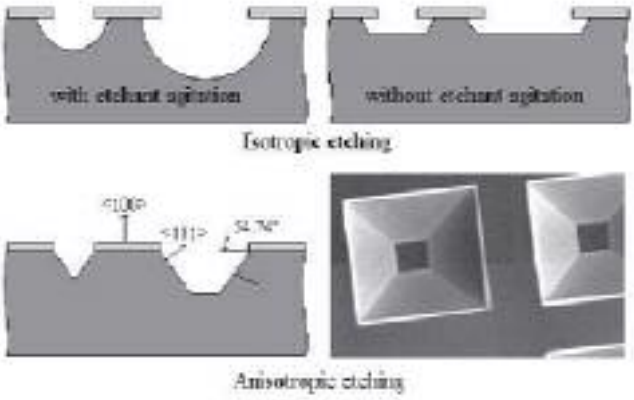

Fig. 1.4: Isotropic and Anisotropic wet etching

are sensitive to solution agitation and temperature, making it difficult to control the geometries of the deep etch usually needed for MEMS. Anisotropic etching developed in the late 60s can overcome these problems. The lower part of Fig. 3.1 shows features

obtained by etching a (100) wafer with a KOH solution. The etched profile is clearly anisotropic, reveling planes without rounded shape and very little underetch. Potassium hydroxide (KOH), tetramethyl ammonium hydroxide (TMAH) and ethylene diamine pyrocatechol (EDP) are common chemicals used for anisotropic etching of silicon. The etching anisotropy has its roots in the different etch rates appearing for different crystal planes because they have different density of electrons. Three important crystal planes, the (100) plane, (110) plane and (111) plane have been illustrated in Fig. 1.5. The three orientations <100>, <110>, and <111> are the respective directions normal to these planes.The anisotropy can be very large and for example, for silicon and KOH, theetching rate ratio can reach 400 between (100) and (111) planes and 600 between (110) and (111) planes - effectively allowing to consider the (111) plane as an etch stop. With different combinations of wafer orientations and mask patterns, very sophisticated structures such as cavities, grooves, cantilevers, through holes and bridges can be fabricated. For example, if the (100) wafers in Fig. 3.2 shows an angle of 54.7° between the (111) plane and the surface, typically producing V-grooves, (110) oriented wafer will present an angle of 90° between these planes resulting in U-grooves with vertical walls. To obtain these grooves, the mask pattern edges need to be aligned with the edge of the (111) planes. For a (100) wafer it is simple because the groove edge are along the <110> direction, that is parallel to the main wafer flat. Moreover the four (111) planes intersect on the (100) surface at 90° and a rectangular pattern will immediately expose four sloping (111) planes and provide a simple way to obtain precisely defined pits and membrane.

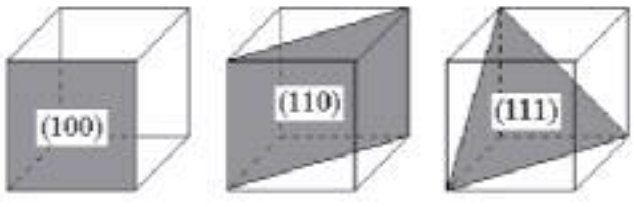

Fig. 1.5: Main planes in the cubic lattice of silicon.

(110) wafers are more difficult to handle, and to obtain a U-groove the side should be tilted by an angle of 125.2° with respect to the <110> wafer flat. In addition, to obtain a four-sided pit, the two other sides should make a 55° angle with the flat direction, defining a non-rectangular pit that is seldom used for membranes. If the control of the lateral etching by using the (111) planes is usually excellent, controlling the etching depth is more complicated. The first possibility is to use the self limiting effect appearing when two sloping (111) planes finally contact each other, providing the typical V-grooves of Fig. 1.5. Controlling the etching time is another alternative. However producing the flat membranes of precise thickness needed for pressure sensors required a better approach that what can be achieved by this simple method. MEMS technologist have tackled this problem by developing different etch stop techniques that reduce by one or two order of magnitude the etch speed when the solution reach a particular depth.

The electrochemical etch stop works by first creating a diode junction for example by using epitaxial growth or doping of a n-layer over a p-substrate. Proper polarization of the substrate and the chemical bath allows for the etching to completely stop at the junction. This process yields an excellent control over the final membrane thickness that is only determined by the thickness of the epitaxial layer, and thus can be better than 1% over a whole wafer. Another popular method that does not require epitaxial growth is to heavily dope the surface of silicon with boron by diffusion or implantation, triggering a decrease of the etch rate by at least one order of magnitude. However, if diffusion from the surface is used to obtain the boron layer, the resulting high boron concentration (> $10^{19}cm^{-3}$) at the surface will decrease substantially the piezoresistive coefficient value making piezoresistors less sensitive. Ion implantation can overcome this problem by burying the doped layer a few μm under the surface, leaving a thin top layer untouched for the fabrication of the piezoresistors.

Actually, the seemingly simple membrane process requires two tools specially designed for MEMS fabrication. Firstly, to properly align the aperture of the backside mask with the piezoresistor or other features on the front side a double-side mask aligner is required.

Different approaches have been used (infrared camera, image storage, folded optical path...) by the various manufacturers (Suss Microtec, OAI, EVGroup...) to tackle this problem, resulting in a very satisfying registration accuracy that can reach 1 μm for the best systems. Secondly, etching the cavity below the membrane needs a special protection tool, that in the case of electrochemical etch stop is also used for insuring the substrate polarization. Actually the presence of this cavity inevitably weakens the wafer and to avoid wafer breakage, the membrane is usually etched in the last step of the process.

At that time, the front side will have already received metallization which generally cannot survive the prolonged etch and needs to be protected. This protection can be obtained by using a thick protective wax, but more often a cleaner process is preferred based on a mechanical chuck. The chuck is designed to allow quick loading and unloading operation, using O-ring to seal the front-side of the wafer and spring loaded contact to provide bias for electrochemical etch-stop.

The chemical used during anisotropic etching are strong bases and it needs to rely on hard mask and not polymer (photoresist) to protect the substrate. Some metals can be used here but generally silicon oxide is preferred with TMAH, while silicon nitride is used with KOH.

Table 1.3 summarizes the characteristics of some anisotropic etching solution.

Solution	Temp (°C)	Si (100) etch rate (μm/min)	Etching rate ratio	Mask etch rate (nm/min)	Boron etch stop (cm^{-3})	Remarks
KOH / H_2O 44g / 100ml (30 wt.%)	85	1.4	400 for (100)/(111) 600 for (110)/(111)	SiO_2 (3.5) Si_3N_4 (< 0.01)	> 10^{20} rate / 20	+largest etching rate ratio -K ions degrade CMOS -etch SiO_2 fast
TMAH / H_2O 25g / 100ml (22 wt.%)	90	1	30 for (100)/(111) 50 for (110)/(111)	SiO_2 (0.2) Si_3N_4 (< 0.01)	$4 \cdot 10^{20}$ rate / 40	+SiO_2 mask +CMOS compat. -large overtech
EDP (Ethylene diamine / pyrocatechol / H_2O) 750ml / 120g / 240ml	115	1.25	+35 for (100)/(111)	SiO_2 (0.5) Si_3N_4 (0.1) Au, Cr, Ag, Cu, Ta (≈ 0)	$7 \cdot 10^{19}$ rate / 50	+SiO_2 mask +no metal etch +CMOS compat. -large overtech -toxic

Table 1.3: Characteristics of some anisotropic etchants.

Of course anisotropic wet etching has its limitation. The most serious one lies with the need to align the sides of the pattern with the crystal axes to benefit from the (111) plane etch-stop, severely limiting the freedom of layout. A typical example is when we want to design a structure with convex corners that is instead of designing a pit, we now want an island. The island convex corners will inevitably expose planes which are not the (111) planes and will be etched away slowly, finally resulting in the complete disappearance of the island. Although techniques have been developed to slow down the etch rate of the corner by adding protruding ‘prongs’, these structures take space on the wafer and they finally cannot give the same patterning freedom as dry etching techniques.

1.8 DRY ETCHING

Dry etching is a series of methods where the solid substrate surface is etched by gaseous species. Plasma is usually involved in the process to increase etching rate and supply reacting ions and radicals. The etching can be conducted physically by ion bombardment (ion etching or sputtering and ion-beam milling), chemically through a chemical reaction occurring at the solid surface (plasma etching or radical etching), or by

mechanisms combining both physical and chemical effects (reactive ion etching or RIE). These methods have various etching selectivity and achieve different etching profiles and usually the etching is more anisotropic and vertical when the etching is more physical, while it is more selective and isotropic when it is more chemical. Most of these methods are discussed in standard microelectronics process books, but they take a different twist when they are applied to MEMS fabrication as in general MEMS necessitates deep (> 5 μm) etching.

Fig. 1.6 illustrates an important parameter commonly used to describe dry etching: the aspect ratio.

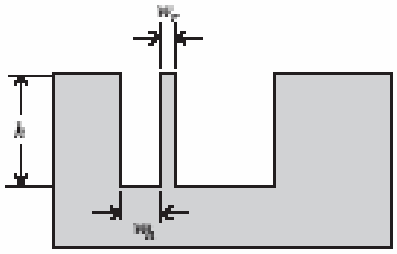

Fig. 1.6: Main parameter in dry etching.

Actually we can define an aspect ratio for features (h/w_r) and for holes (h/w_h) with most technologies giving better results with features than with holes but generally with only a small difference. Typical values for this parameter would range between 1 (isotropic etch) and 50, for very anisotropic etching like the DRIE process. To improve the aspect ratio of the etching, several techniques based on RIE have been developed, usually trying to increase the anisotropy by protecting the sidewalls during etching. For example, the SCREAM process developed in Cornell University alternate steps of etching and growth of oxide that remains longer on the sidewall, while for the RIE cryogenic process, very low temperature in a SF_6/O_2 plasma is used to obtain continuous deposition of a fluoropolymer on the sidewall during the etch. Finally the innovative Bosh process uses

alternating cycle of etching and protection in the plasma chamber to achieve the same function. This important process is the corner stone of DRIE micromaching and will be described in more details in a following section.

1.9 WAFER BONDING

A review of MEMS fabrication technique cannot be complete without mentioning wafer bonding. Wafer bonding is an assembly technique where two or more precisely aligned wafers are bonded together. This method is at the frontier between a fabrication method and a packaging method and belong both to front-end and back-end process, another specificities of MEMS, but at this stage it is not surprising anymore! Wafer bonding has the potential to simplify fabrication method because structures can be patterned on both wafers and after bonding they will be part of the same device, without the need for complex multi-layer fabrication process. Of course epoxy bonding can be used to bond wafers together but much better MEMS techniques do exist. Intermediate-layer eutectic bonding is based

Fig. 1.7 Silicon pressure sensor SP15 bonded with glass cover (courtesy by SensoNor AS An Infineon Technologies Company).

on forming a eutectic alloy that will diffuse into the target wafer and form the bond. For silicon-to-silicon bonding the intermediate layer is often gold which form a eutectic alloy with silicon at 363°C. Silicon-to-silicon fusion bonding allows bonding two silicon wafers directly effectively achieving seamless bond possessing an exceptional strength and hermeticity. However the technique requires excellent flatness and high temperature, two hurdles that limit its use. The most commonly used MEMS bonding methods is probably anodic bonding which is mainly used to bond silicon wafers with glass wafers. The technique work by applying a high voltage to the stacked wafers that induce migration of ion from glass to silicon, allowing a strong field assisted bond to form. This technique is commonly used to fabricate sensors allowing for example to obtain cavities with controlled pressure for pressure sensor as shown in Fig. 1.7. At the same time, the glass wafer provides wafer level packaging, protecting sensitive parts before back-end process. Another important use of wafer bonding is to fabricate MEMS substrates such as SOI and SOG (silicon on glass) wafers.

1.10 SURFACE MICROMACHINING

Unlike bulk micromachining in which microstructures are formed by etching into the bulk substrate, surface micromachining builds up structures by adding materials, layer by layer, on the surface of the substrate. The thin film layers deposited are typically 15 μm thick, some acting as structural layer and others as sacrificial layer. Dry etching is usually used to define the shape of the structure layers, and a final wet etching step releases them from the substrate by removing the supporting sacrificial layer. A typical surface micromachining process sequence to build a micro bridge is shown in Fig. 1.8. Phosphosilicate glass (PSG) is first deposited by LPCVD to form the sacrificial layer. After the PSG layer has been patterned, a structural layer of low-stress polysilicon is added. Then the polysilicon layer is patterned with another mask in $CF_4 + O_2$ plasma.

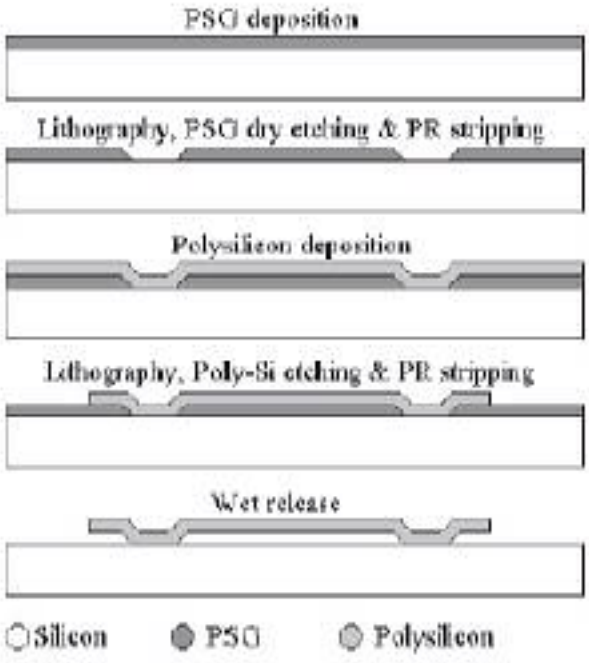

Fig. 1.8 Basic process sequence of surface micromachining.

Finally, the PSG sacrificial layer is etched away by an HF solution and the polysilicon bridge is released.

1.11 LAYER DEPOSITION

The choice of the deposited layers is dictated by many different considerations, as the deposition temperature (dictated by the temperature resistance of the material on the substrate and the allowable thermal stress), the magnitude of the residual stress in the layer (too much stress cause layer cracking), the conformality of the deposition (how the deposited layer follows the profile of the substrate as shown in Fig. 1.9), the roughness of the deposited layer, the existence of pinholes and the uniformity of the deposition, the speed of deposition (to obtain thicker layers).

These previous characteristics are rather general but surface micromachining requires considering an additional condition: the compatibility between sacrificial and structural layers.

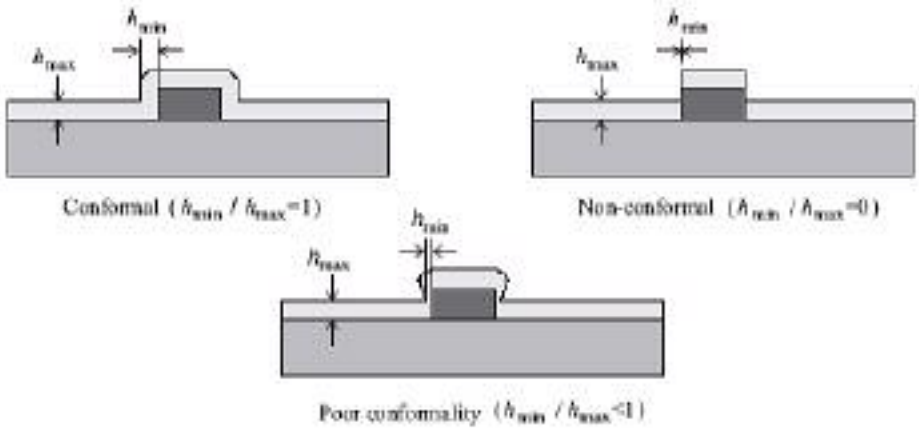

Fig. 1.9 Conformality of layer deposited over a ridge.

Actually, the selection of a suitable sacrificial material depends on the structural material and particularly on the availability of an etching method that can selectively etch the sacrificial material without significantly etching the structural materials or the substrate. A few common combinations of structural material and etching method are shown in Table 1.4, but the list is endless. As a large variety of materials such as polysilicon, oxide, nitride, PSG, metals, diamond, SiC and GaAs can be deposited as thin film and many layers can be stacked, surface micromachining can build very complicated microstructures.

Structural material	Sacrificial material	Etchant
Polysilicon	Oxide(PSG, LTO, etc)	Buffered HF
Si_3N_4	Poly-Si	KOH
SiO_2	Poly-Si	EDP/TMAH
Aluminum	Photoresist	Acetone/O_2 plasma
Polyimide	Cu	Ferric chloride
Ti	Au	Ammonium iodide
SiO_2, Si_3N_4, metal	Poly-Si	XeF_2

Table 1.4: Combination of material and etchants for surface micromachining.

For example Sandia National Laboratories is proposing a process with four polysilicon structural layers and four oxide sacrificial layers, which has been used for fabricating

complex locking mechanism for defense application. Fig.1.10 demonstrates surface micromachined micro-mirrors fabricated using two polysilicon structural layers and an additional final gold layer to increase reflectivity. They have been assembled in 3D like a pop-up structure, using a micromanipulator on a probe-station.

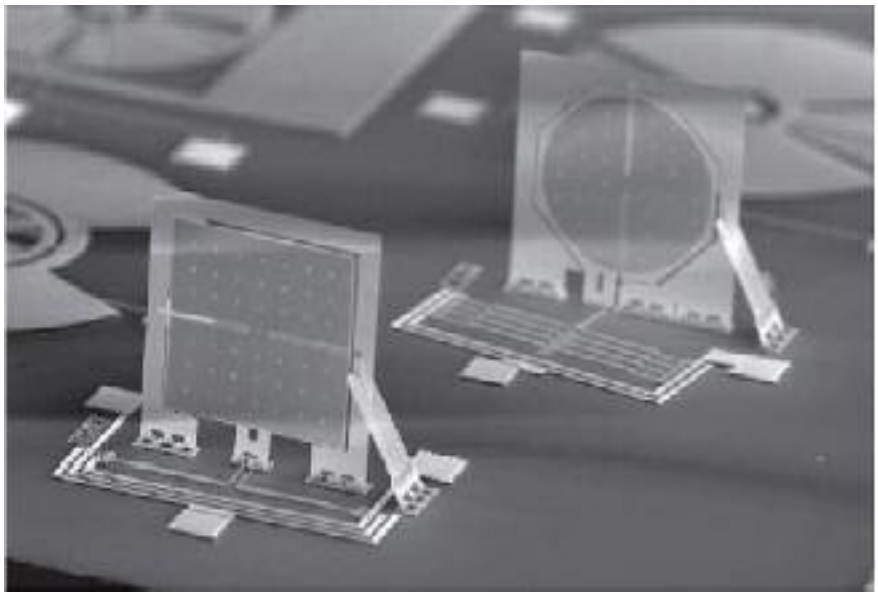

Fig. 1.10: A micro optical stage built by surface micromachining.

1.12 DESIGN LIMITATIONS

Yet surface micromachining has to face several unique problems that need addressing to obtain working devices. During layer deposition, a strict control of the stress in the structural layer has to be exerted. Compressive stress in a constrained member will cause it to buckle, while a gradient of stress across a cantilevered structure causes it to warp, resulting in both case in probable device failure. The possibility to stack several layers brings freedom but also adds complexity.

Actually there is large chance that the topography created by the pattern on underlying layer will create havoc with the upper layer, as illustrated in Fig. 1.11.

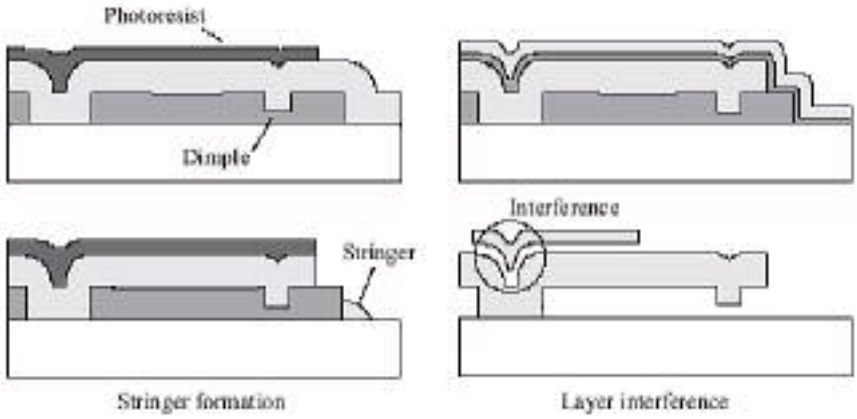

Fig. 1.11: Common surface micromachining issues.

A common problem is the formation of strings of structural material, called "stringers", during the patterning of the upper layer. Actually the high anisotropy of the etching by RIE leaves some material where the layer is thicker because of the conformal deposition of the structural material. To avoid the problem during fabrication, the RIE etching time needs to be substantially increased to fully etch the layer where it is thicker. For example the MUMPS surface micromachining process proposed by the foundry MEMSCAP is using an overteching of 100%, that is, the etching lasts twice the time needed to clear the material in the flat zone. Another common issue is the likelihood of structure interference between the stacked layers. In Fig. 1.11 we see that the topography creates an unintended protrusion below the top structural layer that will forbid it to move freely sideway probably dooming the whole device. This problem can be tackled during layout, particularly when the layout editor has a cross-section view, like L-Edit from Tanner Research. However even a clever layout won't be able to suppress this problem completely and it will need to be addressed during fabrication. Actually polishing using CMP the intermediate sacrificial layer to make it completely flat, will avoid all interference problems. For example, Sandia National Laboratory uses oxide CMP of the second sacrificial layer for their four layers SUMMiT V process. However, sometimes the interference may be a desired effect and for example the so called 'scissors' hinge

[15] design shown in Fig.1.12 benefits greatly from it. As we see here the protrusion below the upper layer helps to hold the hinge axis tightly. If we had to rely on lithography only, the gap between the axis and the fixed part in the first structural layer would be at best 2 μm, as limited by the design rules, and the axis will have too much play. However the protrusions below the staple reduce the gap to 0.75 μm, the thickness of the second sacrificial layer, and the quality of the hinge is greatly increased. The final step in surface micromachining process is the release and this critical step has also a fair amount of issues that need to be considered.

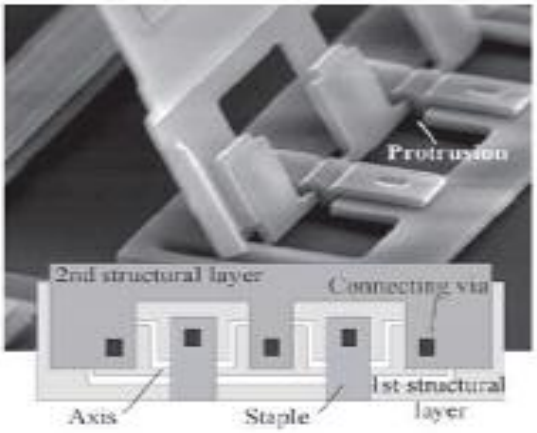

Fig. 1.12: Tight clearance obtained by layer interference in a hinge structure.

1.13 MICROSTRUCTURE RELEASE

The release step is the source of much technologist woes. Release is usually a wet process that is used to dissolve the sacrificial material under the structure to be freed. However the removal rate is usually relatively slow because the sacrificial layer is only a few μm thick and the reaction becomes quickly diffusion limited. Then the depth of sacrificial layer dissolved under the structure will increase slowly with the etching time as

$$d_{\text{release}} \propto \sqrt{t_{\text{etch}}}$$

Simply said, releasing a structure twice as wide will take 4 times more time. However if the etching lasts too long the chemical may start attacking the device structural material too. A first measure to avoid problems is to use compatible material and chemical, where the sacrificial layer is etched quickly but other material not at all. A typical example is given by the DLP (Digital Light Processing) from Texas Instrument, where the structural layer is aluminum and the sacrificial layer is a polymer. The polymer is removed with oxygen plasma, and prolonged release time will only slightly affect the metal. This ideal case is often difficult to reach and for example metals have often a finite etch rate in HF, which is used to remove PSG sacrificial layer. Thus to decrease the release time we have to facilitate etching of the sacrificial layer by providing access hole for the chemical through the structural layer.

In the case of Fig. 1.10 for example, the mirror metal starts to peel off after about 10 minutes in HF. However in about 5 minutes HF could only reach 40 μm under a plain plate, and the designer introduced 'release holes'. These holes in the structural layer are spaced by roughly 30 μm in the middle of the mirror plate (the white dots in the Fig.) allowing for the HF to etch all the oxide beneath in less than 5 minutes. The problems with wet release continue when you need to dry your sample. The meniscus created by the receding liquid/air interface tends to pull the structure against the substrate. This intimate contact give rise to other surface forces like Van der Walls force, which will irremediably pin your structure to the substrate when the drying is complete, effectively destroying your device. This phenomenom is referred as stiction (Fig. 1.13). Strategies that have been used to overcome this problem have tackled it at design and fabrication level. In surface micromachining the idea has been to reduce the contact surface by introducing dimples under the structure. From the fabrication side, super-critical drying, where the liquid changes to gas without creating a receding meniscus, has also been applied successfully. Coating the structure with non-sticking layer (fluorocarbon,

hydrophobic SAM...) has also proved successful and this method, albeit more complex, has the added advantage to provide long lasting protection

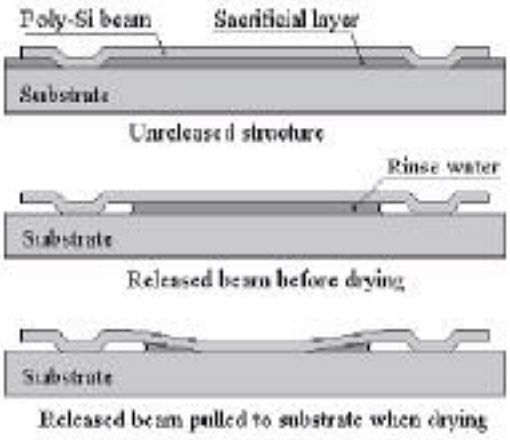

Fig. 1.13: Stiction phenomenon during release.

again sticking that could arise during use. Finally, a completely different approach is to avoid wet release altogether and instead perform a dry release with a gas suppressing completely the sticking concern. In Table 1.3 we describe two popular methods, dissolving polymer sacrificial layer with O_2 plasma, and using xenon difluoride (XeF_2) to etch sacrificial silicon. The xenon difluoride is a gas showing an excellent selectivity, having etching rate ratio close to 1000 with metal and up to 10000 with oxide. The gas has thus been used successfully to release very compliant or nanosized oxide structures where silicon was used as the sacrificial material. The process does not use plasma, making the chamber rather simple, and several manufacturers like XactiX (in cooperation with STS), in the USA or PentaVacuum in Singapore are proposing tools to exploit the technology.

1.14 DRIE MICROMACHINING

Deep reactive ion etching (DRIE) micromachining shares features both from surface and bulk micromachining. As in bulk micromachining the structure is etch in the bulk of

the substrate, but as in surface micromachining a release steps is used to free the microstructure. Fig. 1.14 shows a simplified process of bulk micromachining on silicon-on-oxide (SOI) wafer using deep reactive ion etching (DRIE), a special MEMS dry etch technique allowing large etching depth with very vertical side walls.

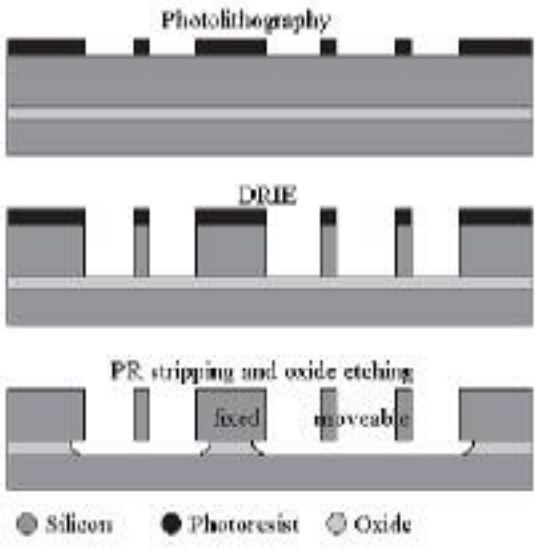

Fig. 1.14: Bulk micromachining of SOI wafer by DRIE.

The SOI wafers used in MEMS usually have a device layer thickness between 10 and 200μm used here as the bulk substrate. After photolithography, the wafer is etched with DRIE to form high aspect ratio silicon structures, and the buried silicon dioxide acts as an effective etching stop. Stripping off the protective photoresist by O2 plasma and then etching the sacrificial layer of the oxide using HF to release the microstructure finish the device. This simple, yet powerful, technique needs only one mask to obtain working devices, and it is understandably used in commercial products. The best known example is the optical switch produced by Sercalo, a company founded by C. Marxer the inventor of this fabrication technique. DRIE has reached a large popularity in recent years among MEMS community and the tools produced by Adixen (Alcatel), Surface Technology Systems (STS) and Oxford System produce high aspect ratio structures (>25) with vertical sidewalls (>89°) at a decent etching rate (6μm/min or more).

A standard DRIE setting uses high density inductively coupled plasma (ICP) as the plasma source, and usually adopts the patented ”Bosch process”. The Bosch process is a repetition of two alternating steps: passivation and etching. In the passivation step, C4F8 gas flows into the ICP chamber forming a polymer protective layer (n (-CF2-)) on all the surfaces. In the following etching step, the SF6 gas in the plasma chamber is dissociated to F-radicals and ions. The vertical ion bombardment sputters away the polymer at the trench bottom, while keeping the sidewalls untouched and still protected by the polymer. Then the radicals chemically etch the silicon on the bottom making the trench deeper. By carefully controlling the duration of the etching and passivation steps, trenches with aspect ratio as high as 25:1 have been routinely fabricated. Fig. 1.15 is a SEM picture of some structures fabricated by DRIE on a SOI wafer. The main issues with DRIE are the presence of ripple with an amplitude over 100nm on the vertical edge due to the repetition of etching and passivating steps, and the quick silicon undertech that happens when the etching reach the buried oxide layer of SOI. However, the most recent DRIE tools have managed to tackle these two problems satisfactorily, by tweaking the recipe and usually trading a bit of etching speed for improving another etching parameter. The SOI wafer used often in DRIE machining is still expensive and it is possible to obtain the thick silicon structural layer by growing it using epitaxy on an oxidized wafer.

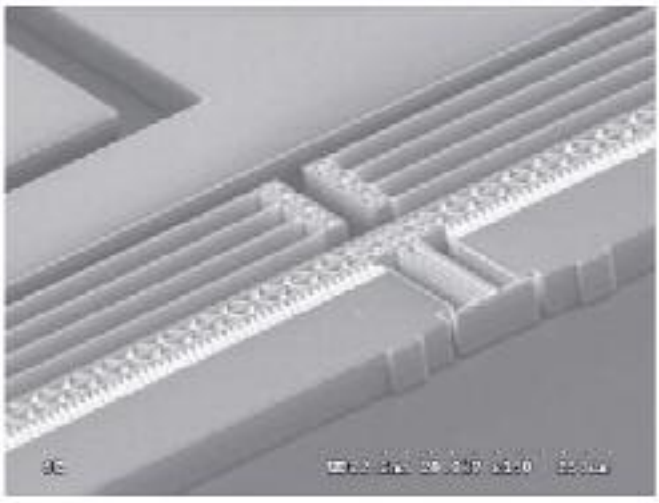

Fig.1.15 50 µm thick structures fabricated by DRIE on SOI.

Even more simply, DRIE has been used is a dry etching version of bulk micromachining (but allowing complete freedom over layout as there is no more crystallographic orientation concerns) without sacrificial layer at all, and using wafer bonding to provide movable part.

1.15 OTHER MICROFABRICATION TECHNIQUES

Other methods exist where no material is removed but this time molded to achieve the desired pattern. LIGA, a German acronym for lithography (LIthographie), electroforming (Galvanoformung), and molding (Abformung) is themother of these methods. LIGA makes very high aspect ratio 3-D microstructures with non-silicon materials such as metal, plastic or ceramics using replication or molding. LIGA process begins with X-ray lithography using a synchrotron source (e.g. energy of 2.4 GeV and wavelength of 2 °A) to expose a thick layer of X-ray photoresist (e.g. PMMA).

Because of the incredibly small wavelength, diffraction effects are minimized and thick layer of photoresist can be patterned with sub-micron accuracy. The resist mold is subsequently used for electroforming and metal (e.g. nickel using NiCl2 solution) is electroplated in the resist mold. After the resist is dissolved, the metal structure remains. This structure may be the final product but to lower down the costs, it usually serves as a mold insert for injection molding or hot embossing.

The possibility to replicate hundreds of part with the same insert opens the door to cheap mass production. When the sub-micrometer resolution is not much of a concern, pseudo-LIGA processes can be advantageously used.

These techniques avoid using the high cost X-ray source for the mold fabrication by replacing it by the thick photoresist SU8 and a standard UV exposure or even by fabricating a silicon mold using DRIE.

1.16 POLYMER MEMS

Bulk and surface micromachining can be classified as direct etch method, wherethe device pattern is obtained by removing material from the substrate or from deposited layers. However, etching necessitates the use of lithography, which already includes patterning the photoresist, then why would we want to etch the lower layer when the pattern is already here? Actually lithography for MEMS has seen the emergence of ultra-thick photoresist that can be spun up to several 100μm and exposed with a standard mask aligner, providing a quick way to the production of micro-parts. SU8, a high-density negative photoresist can be spun in excess of 200 μm and allows the fabrication of mechanical parts [14] of good quality. It is used in many applications ranging from bioMEMS with micro-parts for tissue scaffold or channels, for example to packaging, where it is used as buffer layer. Another application of thick photo-patternable polymer is the fabrication of microlenses using reflow at elevated temperature of thick positive photoresist pillars (e.g. AZ9260). Next to these major techniques, other microfabrication processes exist and keep emerging. They all have their purpose and advantages and are often used for a specific application. For example, quartz micromachining is based on anisotropic wet etching of quartz wafers to take benefit of its stable piezoelectric properties and build sensors like gyroscopes.

Bibliography

[1] I. Fujimasa, *Micromachines, a new era in mechanical engineering,* Oxford University Press (1996)

[2] I.J. Busch-Vishniac, *Electormechanical sensors and actuators,* Dekken Inc. (1998)

[3] K. Tsuruta, Y. Mikuriya, Y. Ishikawa, *Microsensor development in Japan,*Sensor Review 19 (1999) pp.37-42

[4] R. Miles, P. Krulevitch, *Handling Fluids in microsensors,* in S&TR, Nov.1999, pp 11-16, Lawrence Livermore Lab., Nov. 1999

[5] H. Fujita, *Microactuators and micromachines,* IEEE Proc. Vol. 86, n.8 (1998) pp.1721-1732

[6] D.S. Eddy, D. R. Sparks, *Applications of MEMS technology in automative sensors and actuators,* Proc. of the IEEE, Vol.86, n.8 (1998) pp. 1747-1754

[7] K.E. Petersen, *Silicon as a mechanical material,* IEEE Proc. Vol. 70, n.5 (1982) pp.420-457

[8] W. Trimmer, "Microrobot and micromechanical systems", Sensors and Actuators, vol. 19, no. 3, pp. 267-287 (1989)

[9] Fundamentals of microfabrication, M. Madou, 2nd ed., CRC Press, Boca Raton (2002)

[10] MEMS Performance & Reliability, P. McWhorter, S. Miller, W. Miller, T. Rost, Video, IEEE (2001)

[11] Micromachined transducers sourcebook, G. Kovacs, McGraw-Hill, Boston (1998)

[12] K.Petersen, "Silicon as a Mechanical Material", Proceedings of the IEEE, Vol 70, No. 5, pp. 420-457 (1982)

[13] L. Chen, J. Miao, L. Guo, R. Lin, "Control of stress in highly doped polysilicon multi-layer diaphragm structure", Surface and Coatings Technology, vol. 141, no. 1, pp. 96-102 (2001)

[14] "SU-8: Thick Photo-Resist for MEMS", Ed. F. Chollet, 14 Jan. 2006, http: //memscyclopedia.org/su8.html

[15] K. Pister, M. Judy, S. Burgett, R. Fearing, "Microfabricated hinges", Sensors & Actuators A, vol. 33, no. 3, pp. 249-256 (1992)

Chapter 2

DIAMOND PROPERTIES AND GROWTH

2.1 INTRODUCTION

As mentioned in the Introduction of the thesis, the use of silicon as base material for the realization of microsystems is not able to meet all possible applications. It is well known that silicon, in spite of his considerable mechanical and electrical properties presents problems in applications in harsh environments of various types and nature (high temperature, corrosive environments, intense nuclear radiation fields etc..) which limit its use and prevent the realization of microsystems just where they would be extremely useful.

Research and development of new materials with which to carry microsystems is thus an important part of ongoing work in this field. It is therefore necessary to study new materials that will combine the advantages of silicon (lattice excellent properties, good electrical and mechanical properties, ease in obtaining pure material and low-cost processing technologies well known and reliable, etc..) and that can also operate in hostile environments, having mechanical, thermal, optical and chemical properties greater than those of silicon. Among the various materials to consider for this pupose, diamond and in particular artificial diamond produced by CVD technique is undoubtedly the one of the most promising.

2.2 DIAMOND STRUCTURE

Diamond consists of carbon atoms arranged in a tetrahedral lattice classified in crystallography as face-centered cubic (Fig. 2.1), the same as silicon. The C atoms are arranged not only at the corners of the tetrahedron, but also at the center of the faces in positions (0,0,0,) and (1/4, 1/4, 1/4). C atoms are SP3 hybridized and each of them forms four covalent bonds with the four nearest neighbor atoms. The distance between the nearest neighbors atoms is 1.35 Å which is about half that between the atoms of silicon. The diamond then presents an outstanding lightweight but extremely compact structure

which gives it a range of mechanical, thermal and chemical properties very attractive for many applications.

The natural diamond is monocrystalline and depending on the nitrogen content and how it is introduced in the crystal (substitutional, aggregate etc.) is classified in the following format: type IA, IIA, IB and IIB. It should be noted that the type IA is the most abundant in nature and contains about 0.1% nitrogen in the form of small aggregates. The type IB contains nitrogen as an impurity interstitial and almost all artificial diamonds grown at high temperature and pressure are of this type. Types IIA and IIB are very rare in nature. Diamond IIA presents optical and thermal properties superior to other types, while type IIB has excellent properties as a semiconductor and is blue. It should be remembered that among the natural diamonds some properties, such as the resistivity can vary greatly from one type to another. This variation of the properties is normal for artificially grown diamonds because some parameters depend on the type of growth, indeed, as we shall see, the optimization of growth parameter in order to enhance some specific properties is currently used.

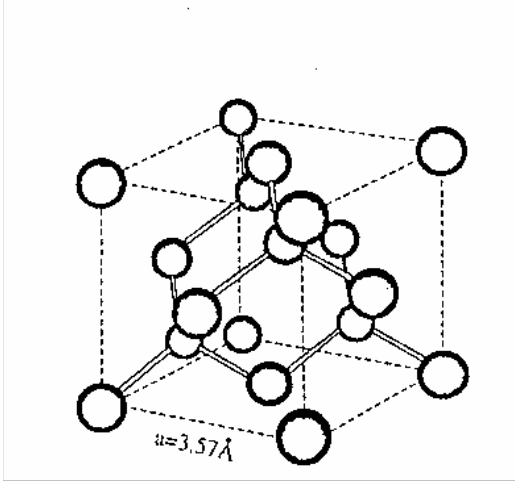

Fig.2.1 : Crystallographic unit cell of the diamond. It is shown the lattice constant a = 3.57 Å.

A direct consequence of the very compact network structure is represented by the large separation (gap) between the valence and conduction bands, which is 5.5 eV. This

band is much wider than that of silicon and makes in fact, pure diamond an insulator at room temperature[1]. Furthermore, diamond has the highest atomic density (1.77×10^{23} cm^{-3}) at atmospheric pressure and a bulk density of 3.52 g/cm^3. The main atomic, crystallographic, thermal and electrical properties of diamond are shown in Table 2.1 where they are also compared with those of silicon and germanium.

Property	Diamond	Silicon	Germanium
Atomic Number Z	6	14	32
Atomic Weight A	12.01	28.09	72.60
Density ($g\ cm^{-3}$)	3.52	2.33	5.33
Number of atoms ($x10^{22}\ cm^{-3}$)	17.7	4.96	4.41
Cristallografic structure	diamond	diamond	diamond
Reticular constant (Å)	3.57	5.43	5.66
Nearest neighbor distance (Å)	1.54	2.35	2.45
Coesione energy U (eV/atomo)	7.37	4.63	3.85
Compressibility ($x10^{11}\ m^2\ N^{-1}$)	0.226	1.012	1.29
Work function ϕ (eV)	4.81	4.58	4.52
Melting point T_m (°C)	3350*	1420	936
Thermal conduttivity σ_T ($w\ cm^{-1}\ °K^{-1}$)	20	1.27	0.653
e^- diffusion coefficient D_n ($cm^2\ s^{-1}$)	47	38	90
h diffusion coefficient D_p ($cm^2\ s^{-1}$)	31	13	45
Dielectric constant ε	5.70	11.9	16
Gap Energy E_{gap} (eV)	5.5	1.12	0.665
Electron-hole pair Energy E_{pair}(eV)	13	3.6	3.0
Intrinsic carrier density n_i (cm^{-3})	$< 10^3$	1.5×10^{10}	2.4×10^{13}
Resistivity ρ_e (Ω cm)	$> 10^{13}$	2.3×10^5	47
Electron mobility μ_n ($cm^2\ V^{-1}\ s^{-1}$)	1800	1350	3900
Hole mobility μ_p ($cm^2\ V^{-1}\ s^{-1}$)	1200	480	1900
Breakdown Voltage ($V\ cm^{-1}$)	10^7	3×10^3	$\sim 10^3$
Young modulus (Gpa)	1134		

Table 2.1 Fundamental properties for diamond, silicon and germanium at 300 °K
***Note:The graphitization of carbon occurs at about 700 ° C in presence of oxygen.**

2.3 SOME CURRENT APPLICATIONS FOR DIAMOND

Diamond is used as an abrasive in machining because of its legendary toughness. Indeed monocristalline diamond is the hardest material in nature and could withstand pressures up to 9000 Kg/mm^2.

Another peculiarity of diamond is to have the highest known Young's modulus (1134 GPa) which is also virtually independent from the direction along which is measured[2]. It is not the same for example, for silicon and SiC which also have cubic structure. Finally we mention the fact that the Young's modulus is virtually independent of temperature up to about 800 ° C [3].

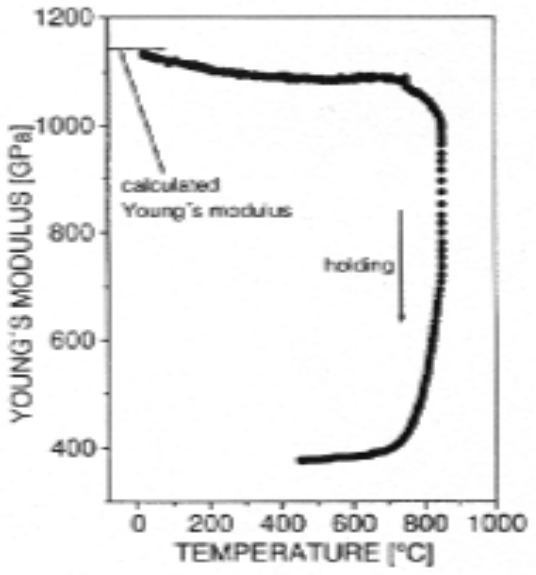

Fig.2.2 Evolution of Young's modulus for diamond crystals as a function of temperature.

Another fundamental aspect of diamond is its resistance to chemicals. It is indeed inert to any chemical attack up to temperatures of 900° C, while at higher temperatures and up to the melting point (3350 ° C) reacts almost exclusively with oxygen at atmospheric pressure[1]. The high melting point is another of the interesting aspects of the diamond making it suitable for the use in environments operating at high temperature.

The diamond also has a remarkable resistance to radiation of various types (*radiation hardness*)[4]. The dose limits are well above those of silicon and this makes it very attractive to operate in radiation fields with high fluence. For example, studies [5] are underway to produce particle detectors capable of supporting the fluences required for the experiment *Large Hadron Collider* (LHC) at CERN in Geneva, Switzerland.

2.3.1.Electronic applications

The already mentioned high-energy difference (gap) between the valence band and the conduction band (E_g = 5.5 eV) allows diamond-based microsystems to operate even at temperatures well above the ambient temperature and up to about 600° C without observing saturation. In the case of silicon for example, temperatures slightly above the ambient temperatures are sufficient to produce saturation. The great value of E_g makes diamond a high resistivity material ($\rho \sim 10^{15}$ Ω/cm in absence of light). The high value of ρ makes possible working with intrinsic diamond-based devices. In the case of silicon, as is known, it is necessary to use *p-n* junctions to achieve the same result.

The high voltage breakdown, about 10^7 V/cm depends on the value of E_g too. The combination of these properties with the thermal characteristics allows to create microsystems capable of absorbing large power compared to their sizes. This is a great advantage because in general the dissipation of power requires large additional volumes.
In the presence of a suitable dopant element, diamond shows evident piezoresistivity properties[6], very useful in the realization of microelectromechanical pressure sensors or accelerometers, also likely to operate at high temperatures[7].

2.3.2.Thermal and optical applications

The thermal conductivity of diamond is 20 W/cm °K and is about 5 times that of copper and comparable with that of materials such as lithium fluoride (LiF) and aluminum (Al_2O_3). This good thermal conductivity is very important when you need to quickly remove the heat generated by mechanical processing. The high thermal conductivity contrasts with the fact already mentioned that at room temperature, the diamond is practically an insulator. Indeed, the high thermal conductivity is related to electrical conductivity (the best electrical conductors are also good heat sinks), being the transport of heat, such as power, linked to electron transport. The diamond is an

exception because its particular structure, extremely compact, combined with the lightness of the carbon atoms that form it, makes it extremely suitable for phonons transport [8], from which depends the transport of heat.

Even from the standpoint of optical properties diamond shows very interesting features. It is virtually transparent to radiation, from ultraviolet to far infrared, corresponding to the gap at 225 nm (5.5 eV). Weak two and three phonons transitions are observed in the intervals 1332-2664 and 2665-3994 cm^{-1} respectively, which are the only intrinsic absorption regions. Other types of absorption is attributable to impurities [9]. The coefficient of transmission for the natural diamond type IIA is shown in Fig. 2.3.

These excellent transparency properties, with the others aforementioned of resistance, candidate the diamond as an "ideal" material to realize optical windows for high power lasers or to optically couple hostile environments [3].

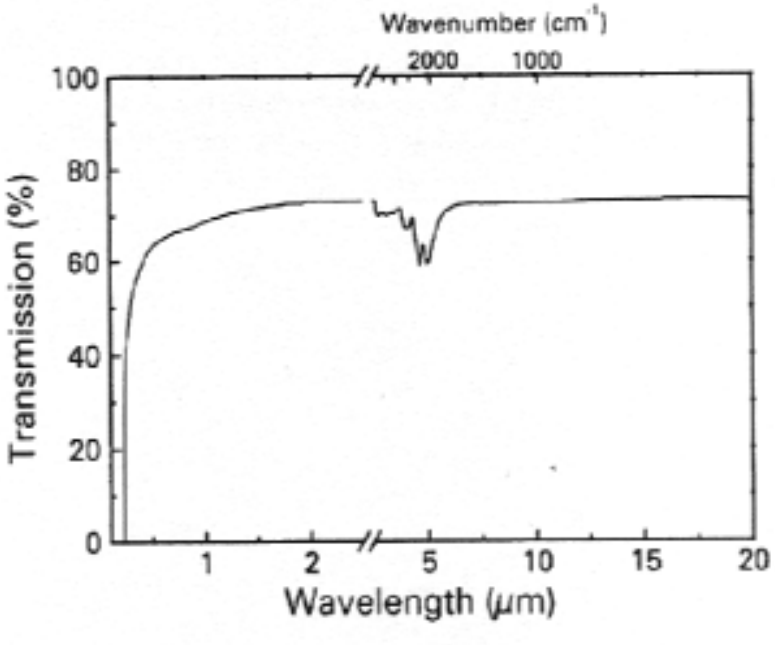

Fig. 2.3 Coefficient of transmission of light for natural diamond type IIA (single crystal) as a function of wavelength.

The reported properties of diamond are to understand how important it can be the application of this material in many fields. As is known, natural diamond as well as being

a little generous in nature can be very expensive (think of the type IIB), and still looks like a single crystal whose shape and dimensions are such as to be hardly used in practice. The same goes for artificial crystals. One reason for the success of silicon is due to the fact that it can be produced in very thin sheets (films), we think of applications in microelectronics and microsystems technology. The introduction of CVD technology for the growth of artificial diamonds has solved this problem. But before we talk about the diamond CVD and their applications in microsystems, a subject which will be the subject of the thesis from this chapter forward, it seems appropriate to recall briefly the chronology of events leading to the production of artificial diamonds [10]. Therefore we will show the most common technique for the production of both monocrystalline diamonds (based on the use of high pressures and high temperatures), both polycrystalline, using methods at low pressure. It is important to recall also that in the first method the growth occurs in the region of stable phase diagram of diamond while in the second pressure is too low and the growth of graphite is largely favoured being the diamond phase only metastable[11].

Historically, the first artificial synthesis of diamond was achieved in 1953 (although the work was never published) at Alemanna Elektris Svenska Aktiebolaget (ASEA). In 1955 the General Electric Company published an article where it reported the synthesis of artificial diamond crystal through technique based on the use of high pressures and temperatures. The first growth of diamond at low pressure was instead realized by W. Eversole in the early fifties of last century (first group ASEA) who synthesized diamond particles using arcs of graphite, thus showing that the diamond can be produced in the region of the metastable phase diagram of carbon. From these efforts, much progress has been made, especially in recent years. The development of methods for the synthesis of diamond CVD is the result of discovery and interaction among americans, russians and japanese research groups. Understanding the role played by hydrogen atoms and

molecules in the process of nucleation and growth over the years has led to significant improvements in outcomes such as the increase in the rate of growth, the suppression of nucleation of carbon graphite and the possibility of nuclear crystals of diamond on different substrates by the same diamond [10]. This last feature of the CVD process allows the growth of polycrystalline diamond on substrates of different material (e.g. Si) for growth surfaces extended to several square centimeters and thicknesses ranging from few microns to at least an inch. We will explain some methods of CVD diamond growth by focusing in particular on the method which uses microwaves since it is the one used in the laboratory where this thesis has been carried out and therefore this technique has been made diamonds used to applications discussed in Chapter 5.

2.4 HIGH PRESSURE HIGH TEMPERATURE METHOD (HPHT)

The method is close to that which naturally leads to the formation of single crystals of diamond, namely the use of an environment of high pressure (~ 60 GPa) and temperature (up to 1600 ° C) to grow crystals from coal. In the laboratory the knowledge of the phase diagram of carbon is used and graphite is employed as starting material. With the HPHT technique largest diamond single crystals are available (up to a few millimeters) but they are characterized by a significant level of impurities [12], not avoidable in those conditions of growth. This limits their use for applications in microsystems, because it was observed that these crystals are disomogeneous, divided into different areas with different levels of purity depending on the crystallographic face that determined the growth. The mechanical processes are the primary field of use for this type of artificial diamond, but its costs not insignificant make, certain times, more convenient to use natural diamond.

2.5 LOW PRESSURE GROWTH METHODS

The introduction of low-pressure methods has allowed enormous progress in the synthesis of artificial diamonds for which the study of these methods is currently very popular. Historically, the first attempts of diamond synthesis at low pressure are due to russian research groups since 1963 [13,14], but the first eteroepitaxial growth of diamond on (001) silicon substrate was produced in Japan in 1992 [15]. In the methods of growth at low pressure diamond is deposited with the technique called *Chemical Vapor Deposition* (CVD), using carbon in gaseous phase in the form of a suitable chemical precursor (eg CH_4). The carbon is selected by providing energy to the gas so as to separate the molecules in which it is kept bound. This can be obtained by heating with radio frequency. Nowadays, the use of a technique rather than another, as well as the choice of mixtures and gases as precursors, differentiates and distinguishes the different types of technologies in use for the growth of CVD diamond.

We remind that the industrial production of diamond was actually made possible by the CVD technique that allows to introduce a "hot zone" in the gas phase of the production process through some active elements such as the hot filament, the disk of graphite heat, RF etc.

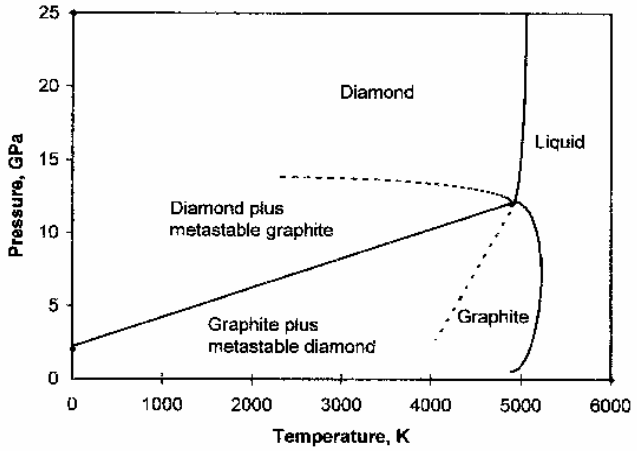

Fig. 2.4 Diamond phase diagram

This fact makes it possible to decouple the effects of temperature on the surface of the substrate than the temperature of the gas.

Fig. 2.4 (phase diagram) relates the rate of growth of CVD diamond [16] with the gas temperature for the various techniques used today.

Fig. 2.5 illustrates how the diamond growth species, as well as the presence of atomic hydrogen necessary to suppress the growth of non-diamond crystals, is much more efficient for temperatures higher than 1500 °C. Below this temperature it is observed that the diamond tends to the state of graphite. It is understandable then how the introduction of a "hot zone" has helped to overcome many of the difficulties inherent in the process of synthesis of diamond.

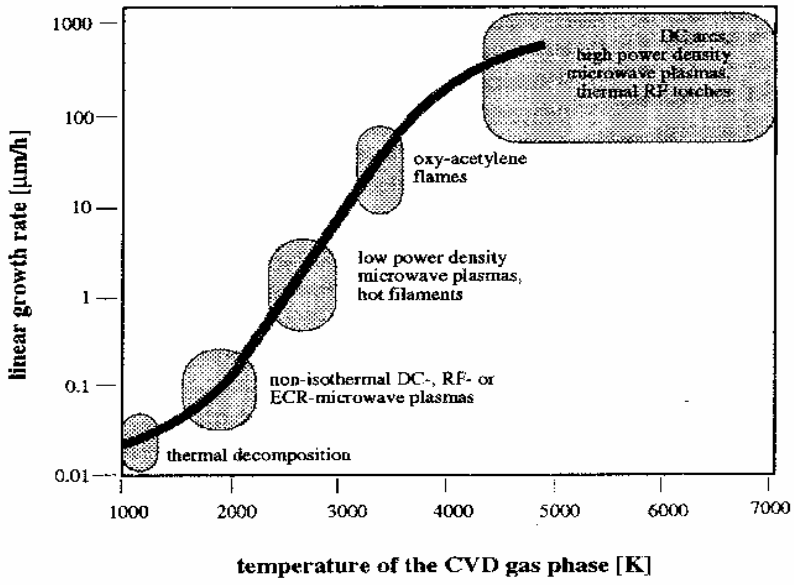

Fig. 2.5 Correlation between gas temperature and diamond growth rate in the CVD process.

2.5.1 Hot filament method

Historically, the Hot-Filament Chemical Vapour Deposition (HFCVD) method for the production of CVD diamond was firstly reported by Matsumoto et al. in 1982 [17] and precedes the method with microwaves [15]. The technique requires the presence of atomic hydrogen, as in the case of microwaves and a filament of hot metal placed in proximity of the silicon substrate (Fig.2.6).

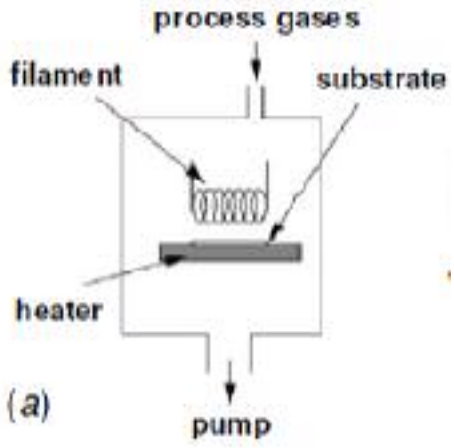

Fig. 2.6 Schematic diagram of deposition apparatus for hot filament

The filament, usually tungsten, is placed few millimeters from the silicon substrate where the deposition of diamond will take and is electrically heated up to 2000 °C. The growth chamber temperature is kept at around 700-1000 °C, while the gas flowing inside is composed of a mixture of methane (about 1% by volume), diluted in nitrogen with a flow rate of 10-100 cm^3/min.

The chamber pressure is maintained in the range 1-10 kPa. HPCVD method is in principle very simple and economic, and it is certainly also the most common. Moreover, the quality and properties of diamond can be changed by changing the parameters of growth. It is also possible to select the preferential orientation of grains and thus vary the morphological and structural properties of the deposited diamond. As is known varying the orientation of the grains implies varying the concentration and type of structural defects that affect the properties of the deposited film (eg, electronic properties).

Perhaps the most interesting aspect of this technique, is the flexibility in shape and size of the deposited films. Particularly if the substrate is not regular or not flat diamond surfaces of any shape can be obtained, e.g. diamond microtips. The deposition rate is of the order of 0.1 - 1 μm / h, consistent with that of other CVD techniques. The quality of the films obtained is good from the viewpoint of optics and electronics.

Among the problems associated with this technique we underline the high concentration of impurities and the low stability of the deposition process. These are closely linked to the use of the filament of W, which may deliver ions of this species that inevitably end up deposited in the substrate. Moreover, with prolonged growths, the filament tends to become carbon and a more marked inhomogeneity is observed in the deposition.

2.5.2 Combustion Flame and Plasma Jet Deposition

Without quote in full, we recall two other techniques for the growth of CVD diamond, they are *Combustion Flame Deposition* and *Plasma Jet Deposition* [18,19,20].

Combustion Flame Deposition takes its name from the fact that the excitation energy necessary for the growth of the diamond comes from a flame generated by combustion of a hydrocarbon (typically acetylene) combined with oxygen so that the stoichiometric relationship between C and O is about 1:1. Often, to improve the stability of the flame and the layer of diamond as grown, hydrogen is also added to the mix. The substrate growth, mounted on a special sample holder is exposed to direct flame and water cooled. This method is very simple and has the advantage of high growth rates (up to 50 μm/h), but the quality of the diamond (especially for the optical and electronic purity) is not comparable to that of the previous techniques especially that of CVD diamond. However, maintaining good mechanical and thermal properties this technique makes diamond suitable for coating of tools for machining.

Plasma Jet Deposition (PJD) is a technique that uses a plasma to form the energy required for the growth of diamond. The substrate is placed at the exit of a plasma source in a vacuum environment (approximately 100 mbar). The gases used are typically hydrocarbons by adding hydrogen. The use of oxygen can also improve the quality of the produced films. Like Combustion Flame Deposition, PJD has a high rate of growth (up to 100μm/h), but the quality of the films is higher than the previous technique, in

particular as regards the optical properties. Problems arise in obtaining homogeneous surface areas greater than 1 cm^2.

2.6 MICROWAVE PLASMA ENHANCED CVD

The use of a plasma to provide the energy required to activate the chemical deposition from the vapor phase is not an exclusive production of artificial diamonds, but with some variations, is also used for the formation of polymers, amorphous silicon, nitrate silicon, optical fiber on silicon and other materials and/or compounds.

In the case of diamond, it is possible to use either plasma discharges with 13.45 MHz radiofrequency than plasmas activated with microwaves at 915 MHz or 2.45 GHz. The use of a particular frequency is not justified by physical and/or technology reasons but rather by problems of legislation in different countries where different systems are ready.

The *Microwave Plasma Enhanced Chemical Vapor Deposition* o MPECVD [19,20]) is characterized by high purity of the films obtained (so it is particularly interesting for the production of microsystems), although, for problems related to the density power in plasma, is not suitable to the production of large surface areas (<100 cm^2) and can not be applied to produce non-planar surfaces. In literature several types of machines are reported, each running a different system of plasma originating from the various possible frequencies [19]. In the following the working principle of this technology is described.

A typical reactor for the growth of plasma assisted CVD diamond is shown in Fig. 2.7 and represents the apparatus used in our laboratory. It consists of a vacuum chamber with controlled entry of gas and a plate on which is placed on the substrate on which to grow the diamond. The microwaves, generated by a commercial magnetron are directed in the chamber (which then also acts as a resonant cavity) through a waveguide. The plasma is generated directly in contact with the substrate. It is very important to get a plasma as stable as possible, so the choice of plasma parameters is very important. Microwaves give

energy to the electrons of the plasma, which, in turn, give energy to the gas mixture through collisions heating it [22]. The reactions that follow this warming leads to the formation of carbon which is then deposited on the substrate suface. If the surface conditions are suitable (presence of nucleation centers) a new diamond layer is formed with a growth rate varying from 0.2 to 10 μm/h, depending on the growth parameters (gas composition, pressure, plasma temperature, power density of microwaves etc..) and on the geometry of the growth chamber.

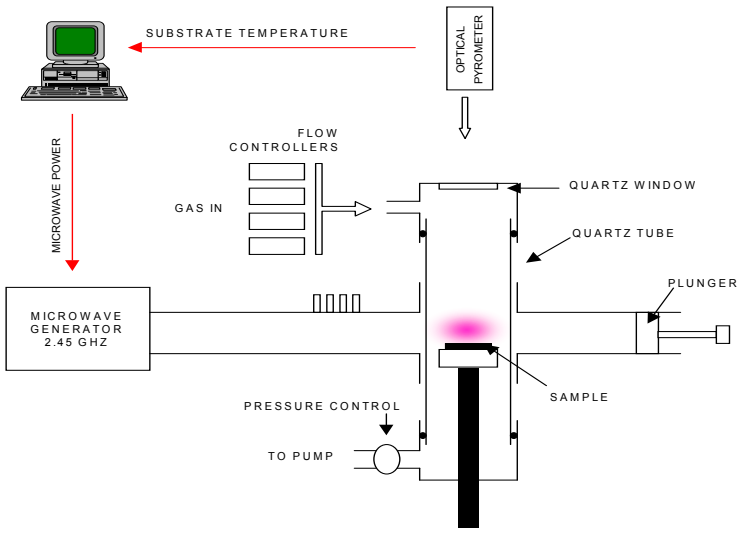

Fig.2.7 Scheme of the apparatus used in this work for the deposition of CVD diamond films.

2.6.1 Gas mixtures , C/H/O diagram and CVD diamond growth

The experience, but also the theory, show that the choice of gas mixture and its purity play a major role on the quality of the diamond product and its rate of growth. Chemical species to be used is essentially carbon and hydrogen. The presence of oxygen can lead to an increase in the rate of growth. The most used is a mixture of methane (CH_4) into hydrogen. The mechanism that leads to the growth of CVD diamond has not been fully elucidated. The most reliable theories [23] assume a simultaneous deposit of hybridized sp^3 carbon (diamond) and sp^2 (graphite), but the presence of hydrogen facilitates the

removal of graphite. The formation of diamond is facilitated by hydrogen because it reacts on the surface of the film with the hybridized sp^2 free carbon bindings [24], forming a uniform layer of saturated hydrocarbons which prevents a single species of atoms to go and settle on the surface. This theory is supported by the observation that if you remove the layer of hydrogen, there is a rearrangement of atoms on the surface.

The systematic study of the properties of CVD diamond, related to the type and composition of the mixture used for their growth has allowed Bachmann to develop its namesake diagram [25] (Fig. 2.) that explains and predicts the dependence of the deposited diamond by gas mixture used for growth. The diagram in question is a triangle and each side shows the concentrations of the three atomic species C, O, and H used in the blend. There are three regions: a) no growth, b) growth of graphite but not diamond, c) domain of the diamond. The latter is enclosed between the first two that are dominant. The diagram clearly shows how you can get diamond even in the absence of oxygen. In this case, the most widely used mixture consists of small percentages of methane into hydrogen. It is also possible to obtain diamond in the presence of oxygen, but in this case, there is growing diamonds only if the concentration of C is slightly larger than oxygen. This occurs because the formation of CO and the diamond is deposited only if C atoms remain sufficiently. Finally, the diagram shows the lines of the concentrations of C, H and O on the use of the most common gas mixtures used for growth (CO_2-CH_4, CO_2-C_2H_6, CO_2-C_2H_4, CO_2-C_2H_2).

A key aspect to obtain good quality diamond is the purity of gases used. The presence of impurities in the mixture leads to their deposition and therefore to the formation of defects of various types and nature in the crystal of diamond. In this regard, we remember that just because the CVD technique works at lower temperatures, diffusion and the concentration of pollutants inside the crystal is lower than other production techniques of diamond.

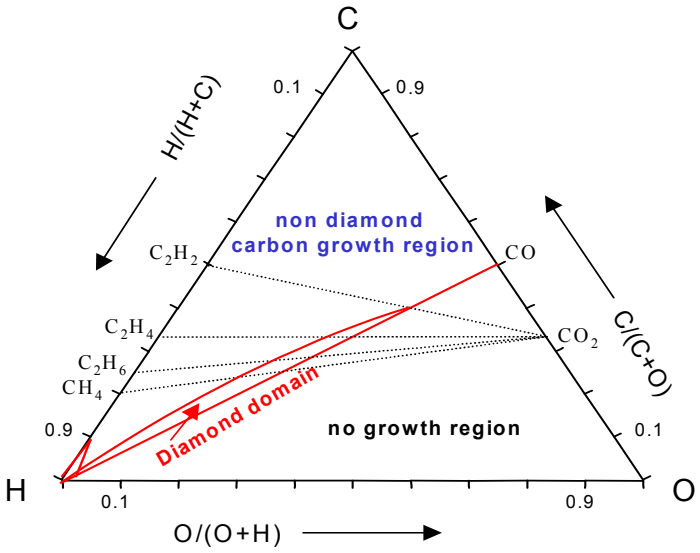

Fig.2.8 Bachmann chart or diagram for diamond for ternary gas concentration present in the growth chamber.

2.7 DIAMOND FILMS PRODUCTION

As previously mentioned the study of optimization of growth parameters for CVD has been deepened in detail in previous works [26], here we simply recall in this thesis the type of apparatus used and the type of the films obtained, while in the next chapters we deal with their characterization as radiotherapic devices.

The production process of radiation detectors object of this thesis work involves a first deposition of a single crystal "*p doped*" diamond film (SCD-p) on a commercial HPHT single crystal diamond substrate followed by a second deposition of an intrinsic film (SCD-i) on the "*p doped*" layer. For this purpose, two different reactors, built and installed at the laboratories of the Dept. of Mechanical Engineering, University of Rome "Tor Vergata" were used; the first, for the synthesis of SCD-p films doped with boron, the second, used exclusively for the growth of SCD-i. The complete separation of the two plants is motivated by the need to deposit the SCD-i layer in a controlled environment as free as possible from contamination: this second film represents in fact, the sensitive volume of the future detector, and the presence of impurities will strongly degrade its performances (increased dark current, signal instability, memory

effects, slow response time, worsening of the spectroscopic properties, etc..). The boron used for the synthesis of the p-doped layer (typically in gaseous phase in the form of diborane diluted in H_2) heavily contaminates the growth chamber so that, even in the absence of the substance that provides the dopant, is strongly unadvisable using the same CVD reactor for depositing ultrapure intrinsic diamond films.

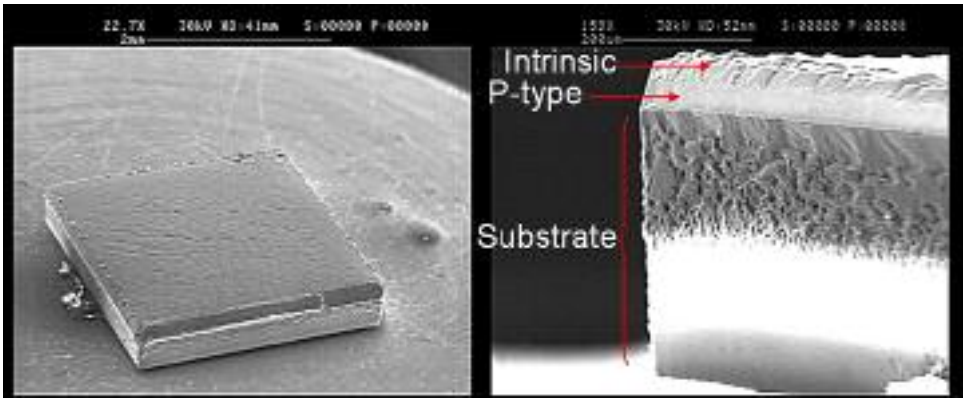

Fig. 2.9a) SEM image of the whole diamond sample after the two-step growth process. b) side view in which are roghly indicated the HPHT substrate, the p-doped layer and the intrinsic active layer on the top.

2.8 CVD DIAMONDS FOR MICROSYSTEMS

Referring to the literature to deepen of the details regarding the technical aspects of the CVD diamond growth [19], details that have been also extensively studied and optimized over the years in the Laboratory of Microsystems Engineering of the "Tor Vergata" University [20,21], we note that the CVD technique can be regarded as a deposition of atomic carbon on an existing diamond-like lattice structure. This carbon atoms are obtained breaking the C-H bonds of hydrocarbons precursors, by mean of atomic hydrogen present in the growth chamber. Obviously the one exposed is a very short and simple synthesis of a very detailed and complex problem that depends primarily on the gas used, the type of reactor and the substrate on which deposition occurs. Regarding the latter aspect, most of the films of artificial diamond produced to date and reported in literature are growth on substrates of monocrystalline silicon. This is due to

the large availability of excellent quality material at relatively low cost and to its physical properties, well suited for the use as substrate in CVD diamond synthesis: melting point sufficiently high (1683 K), formation of a very thin carbide layer (often only a few nanometers), coefficient of thermal expansion and reticular mismatch relatively low. Molybdenum and tungsten also have properties similar to that of silicon and are widely used as substrates. However, although it is economically advantageous, the growth of diamond on different substrates imply a pre-treat procedure to create a sufficiently high density of sites, known as "nucleation centers" from which to originate and evolve the sp^3 tetrahedral lattice. Anyway, the produced films are inevitably polycrystalline, characterized by a large number of grain edges and defects, with a typical columnar structure. Using instead monocrystalline diamond as substrate (natural or, more conveniently, HPHT artificial diamond of low electronic-quality) the growth surface presents inherently, on atomic-scale, the tetrahedral-type diamond structure and the deposition process of the carbon atoms is omoepitaxial, representing no more than the simple extension, atom by atom, of an existing network structure. The resulting films thus maintain the crystallographic perfection of the monocrystalline substrate of departure [27] and are completely free of structural defects and discontinuities that degrade the mechanical, electronic and spectroscopic properties. To this respect it is known that the films of synthetic diamond grown on (100) oriented substrates contain much less structural imperfections than those grown on surfaces (110) and (111). In the specific case of monocrystalline diamond films made during the period of the PhD, the substrates are commercial HPHT monocrystalline diamond type Ib (100) oriented produced by Element Six™ (De Beers Industrial Diamond Division).

In the field of micro-machining, diamond, either monocrystalline or polycrystalline can be machined based on different principles from microlithography. The diamond can be attacked with plasma in the presence of oxygen, moreover, considering that diamond

doesn't growth on oxidized silicon substrates it is possible to lead a selective growth for example through an appropriate mask. It is obvious that, in any case, good quality diamonds is needed to be able to fully exploit all the possibilities of application. Applications of diamonds to temperature sensors were reported in the literature [24]. In particular, diamond-based thermistors capable of operating over a wide range of temperatures and in high temperature environments were produced [28]. Since CVD diamond also has piezoresistivity properties, diamond-based pressure sensors [29,30] were produced.

In literature are also reported several applications of CVD diamond in electronics [24]. Both diodes and transistors were made [31,32]. But all these, and others applications are still not suitable for real applications in microsystems. Just taking into account this fact and the very definition of micro, in the next chapters we will expose our work to achieve micro-or parts of it (e.g. detector) using CVD diamond films obtained in our laboratory. Thus, a particular effort has been made in the feasibility of the device industry, starting from the basic material to the final realization.

Bibliography

[1] A.M. Stoneham, *Recent development in the theory of diamond,* The Properties of diamond, ed. J.E: Field, Academic Press (1990), pp.185

[2] C.A. Klein, G.F. Cardinale, Diamond and related Material 2 (1993) 918

[3] M. Werner, R. Locher, *Growth and application of undoped and doped diamond films,* Rep. Prog. Phys. 61(1998) 1665

[4] C. Bauer et al., *Radiation hardness studies of CVD diamond detectors,* Nucl. Instr. Meth. in Phys. Res. A 367 (1995) 207

[5] M.M. Zoeller et al., *Performance of CVD diamond microstrip detectors under particle irradiation***,** IEEE Trans. Nucl. Sci. 44 n.3 (1997) 815

[6] W.L. Wang, X. Jiang, K. Taube, C.P. Klages, J. Appl. Phys. 82 (2) (1997) 729

[7] I. Taher, M. Aslam, M.A. Tamor, T.J. Potter, R.C. Elder, Sensors and Actuators A, 45 (1994) 45

[8] J.R. Olson, R.O. Pohl, J.W. Vandersande, A. Zoltan, T.R. Antony, W.F. Banholzer, Phys. Rev. B47 (1993) 14850

[9] J.I. Pankove, C.H. Qiu, "*Optical properties and optoelectronic application of diamond",* Syntetic Diamond, Ed. K.E. Spear and J. P. Dismukes, Wiley and Son Publ. (1994)

[10] J.C. Angus, "*A short story of diamond synthesis",* in The Physics of Diamond, Proc. of the Int. School of Physics. "Enrico Fermi", Course CXXXV, Varenna (Italy) 23 July – 2 August 1996, ed. C. Paoletti, A. Tucciarone, IOS Press 1997, pp.1-8

[11] J.C. Angus, "*Structure and thermochemistry of diamond",* Ibid, pp.9 – 30

[12] R. J. Weldake, *"Technology of Diamond Growth",* The properties of Diamond, ed. J.E. Field, Academic Press (1990) pp.501

[13] B.V. Derianguin, D.V. Fedoseev, V.M. Lukyanovich, B.V. Spitzin, V.A. Ryabov, A. Lavrentyev, J. Crist. Growth 2 (1968) 380

[14] B.V. Derianguin, D.V. Fedoseev, Carbon, 11 (1973) 299

[15] X. Jiang, C.P: Klages, Diam. Relat. Mater. 2 (1993) 1112

[16] P.K. Bachmann, H. Lydtin, in *"Characterization of Plasma Process",* edited by G. Lukovsky, D.E. Ibbotson and D.W. Hess, Mater. Res. Sym. Proc. 165 (1990) pp.181

[17] S. Matsumoto, Y. Sato, M. Kamo, N. Seneka, *Japan J. Appl. Phys.* 21L (1982) 183

[18] M.A. Cappelli, T.G. Owano, *"Plasma-Jet Deposition of Diamond",* Ibid, pp. 59

[19] P.K. Bachmann, *"Plasma Chemical Vapor Deposition of Diamond Films",* in The Physics of Diamond, Proc. of the Int. School of Physics. "Enrico Fermi", Course CXXXV, Varenna (Italy) 23 July – 2 August 1996, ed. C. Paoletti, A. Tucciarone, IOS Press 1997, pp.45 – 71

[20] G. Balestrino, M. Marinelli, E. Milani, A. Paoletti, I. Pinter, A. Tebano, *Appl. Phys. Let.* 62 (8) (1993)879

[21] M. Marinelli, E. Milani, A. Paoletti, A. Tucciarone, G. Verona Rinati, M. Angelone, M. Pillon, *Appl. Phys. Lett.* 75 (1999) 3216

[22] E. Hyman, K. Tsang, A. Drobot, B. Lane, J. Casey, R. Post, *J. Vac. Sci. Techn*. A 12 (1994) 1474

[23] B.V. Deryagin, D.V. Fedoseev, *Growth of diamond and graphite from the gas phase,* Surf. Coat. Technol. 38 (1989) 131

[24] D.G. Goodwin, J.E. Butler, *Theory of diamond chemical vapor deposition,* Handbook of Industrial Diamonds and Diamond Films, ed. M. Prelas, G. Popovici, L. Bigelov, (New York : Marcel Dekker, 1997)

[25] P.K. Bachmann, D. Leers, H. Lydtin, D.U. Wiechert, *Diamond Relat. Mater.* 1 (1991) 1

[26] G. Verona-Rinati, *Applicazioni del diamante sintetico nella tecnologia dei microsistemi,* PHD Thesis XII° Cycle, Univ. "Tor Vergata" Roma, October 1999.

[27] G. Prestopino, *Microrivelatoridi neutroni in diamante monocristallino CVD* PHD Thesis XXI° Cycle, Univ. "Tor Vergata" Roma, June 2009.

[28] M. Werner, O. Dorsch, E. Obermeier, *Electron Technol*. 27 (1994) 83

[29] M. Werner, *Low Pressure Synthetic Diamond: Manifacturing and Applications,* ed. B. Dischler and C. Wild (Berlin : Springer) p. 243

[30] M. Werner, O. Dorsch, E. Obermeier, *Diam. Relat. Mater.* 4 (1995) 873

[31] A.J. Tessmer, L.S. Plano, D.L. Dreifus, *IEEE Electron. Devices Lett.* 14 (1993) 66

[32] P. Gluche, A. Aleksov, A. Vescan, W. Ebert, E. Kohn, *IEEE Trans. Electron. Devices Lett.* 18 (1997) 547

Chapter 3

DOSIMETRIC PRINCIPLES QUANTITIES AND UNITS

3.1. INTRODUCTION

Radiation measurements and investigations of radiation effects require various specifications of the radiation field at the point of interest. Radiation dosimetry deals with methods for a quantitative determination of energy deposited in a given medium by directly or indirectly ionizing radiations. A number of quantities and units have been defined for describing the radiation beam, and the most commonly used dosimetric quantities and their units are defined below. A simplified discussion of cavity theory, the theory that deals with calculating the response of a dosimeter in a medium, is also given.

3.2. PHOTON FLUENCE AND ENERGY FLUENCE

The following quantities are used to describe a monoenergetic ionizing radiation beam: particle fluence, energy fluence, particle fluence rate and energy fluence rate. These quantities are usually used to describe photon beams and may also be used in describing charged particle beams.

- The particle fluence Φ is the quotient dN by dA, where dN is the number of particles incident on a sphere of cross-sectional area dA:

$$\Phi = \frac{dN}{dA} \tag{3.1}$$

The unit of particle fluence is m^{-2}. The use of a sphere of cross-sectional area dA expresses in the simplest manner the fact that one considers an area dA perpendicular to the direction of each particle and hence that particle fluence is independent of the incident angle of the radiation [1,2].

- Planar particle fluence is the number of particles crossing a plane per unit area and hence depends on the angle of incidence of the particle beam.

- The energy fluence Ψ is the quotient of dE by dA, where dE is the radiant energy incident on a sphere of cross-sectional area dA:

$$\Psi = \frac{dE}{dA} \tag{3.2}$$

The unit of energy fluence is J/m^2. Energy fluence can be calculated from particle fluence by using the following relation:

$$\Psi = \frac{dE}{dA} E = \Phi E \tag{3.3}$$

where E is the energy of the particle and dN represents the number of particles with energy E. Almost all realistic photon or particle beams are polyenergetic, and the above defined concepts need to be applied to such beams. The concepts of particle fluence spectrum and energy fluence spectrum replace the particle fluence and energy fluence, respectively. They are defined respectively as:

$$\Phi_E(E) = \frac{d\Phi}{dE}(E) \tag{3.4}$$

and

$$\Psi_E(E) = \frac{d\Psi}{dE}(E) = \frac{d\Phi}{dE}(E)E \tag{3.5}$$

where $\Phi_E(E)$ and $\Psi_E(E)$ are shorthand notations for the particle fluence spectrum and the energy fluence spectrum differential in energy E, respectively [2].

Fig.3.1 shows a photon fluence and an energy fluence spectrum generated by an orthovoltage X ray unit with a kVp value of 250 kV and an added filtration of 1 mm Al and 1.8 mm Cu (target material: W; inherent filtration: 2 mm Be). Orthovoltage X-rays are produced by X-ray generators operating at voltages in the 200–500 kV range, and therefore an energy in the 200–500 keV range. When used to treat patients, radiation oncologists find that they penetrate to a useful depth of about 4–6 cm. That makes them good for treating skin, superficial tissues, and ribs, but not for deeper structures such as lungs or pelvic organs.

The two spikes superimposed on the continuous bremsstrahlung spectrum represent the K_α and the K_β characteristic X ray lines produced in the tungsten target.

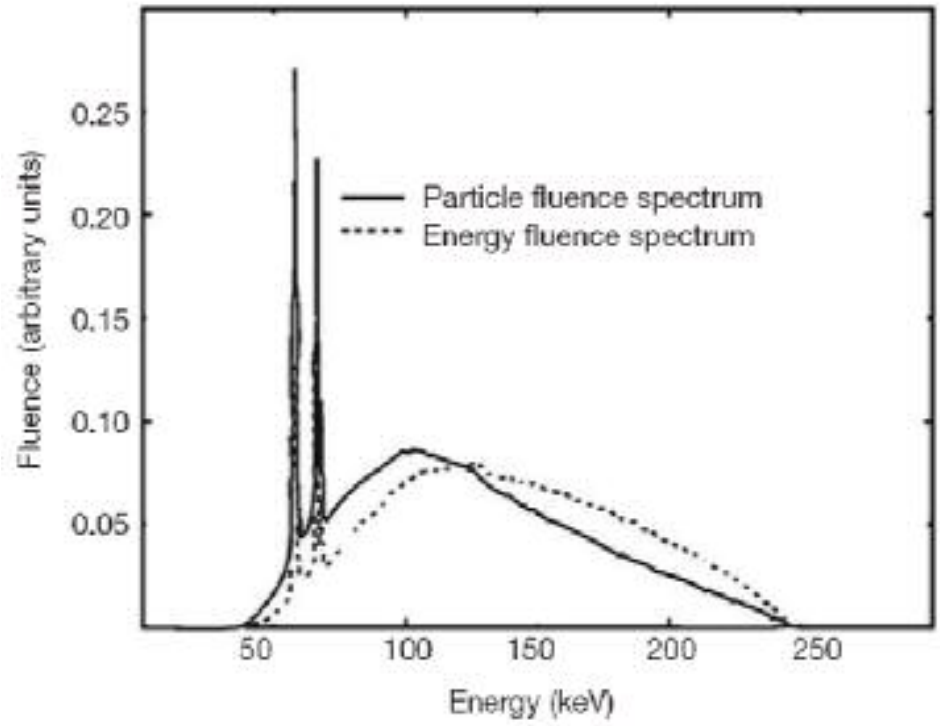

FIG. 3.1 Photon fluence and energy fluence spectra at 1 m from the target of an X ray machine with a tube potential of 250 kV and added filtration of 1 mm Al and 1.8 mm Cu (target material: W; inherent filtration: 2 mm Be).

The particle fluence rate is $d\Phi/dt$ (units of $m^{-2} \cdot s^{-1}$), while the energy fluence rate $d\Psi/dt$ (also referred as intensity) is the increment of the energy fluence in the time interval dt (units of W/m^2 or $J/m^2 \cdot s^{-1}$).

3.3. KERMA

Kerma is an acronym for Kinetic Energy Released per unit MAss. It is a non-stochastic quantity applicable to indirectly ionizing radiations such as photons and neutrons [3]. It quantifies the average amount of energy transferred from indirectly ionizing radiation to directly ionizing radiation without concern as to what happens after this transfer. In the discussion that follows we will limit ourselves to photons.

The energy of photons is imparted to matter in a two stage process. In the first stage, the photon radiation transfers energy to the secondary charged particles (electrons) through various photon interactions (the photoelectric effect, the Compton effect, pair production, etc.). In the second stage, the charged particle transfers energy to the medium through atomic excitations and ionizations.

In this context, the kerma is defined as the mean energy transferred from the indirectly ionizing radiation to charged particles (electrons) in the medium $d\overline{E}_{tr}$ per unit mass dm:

$$K = \frac{d\overline{E}_{tr}}{dm} \tag{3.6}$$

The unit of kerma is joule per kilogram (J/kg). The name for the unit of kerma is the gray (Gy), where 1 Gy = 1 J/kg.

3.4. CEMA

Cema is the acronym for Converted Energy per unit MAss. It is a nonstochastic quantity applicable to directly ionizing radiations such as electrons and protons [3]. The cema C is the quotient of dE_c by dm, where dE_c is the energy lost by charged particles, except secondary electrons, in collisions in a mass dm of a material:

$$C = \frac{dE_c}{dm} \tag{3.7}$$

As for kerma, cema is measured in joule per kilogram (J/kg).

3.5. ABSORBED DOSE

Absorbed dose is a non-stochastic quantity applicable to both indirectly and directly ionizing radiations. For indirectly ionizing radiations, energy is imparted to matter in a two step process. In the first step (resulting in kerma), the indirectly ionizing radiation

transfers energy as kinetic energy to secondary charged particles. In the second step, these charged particles transfer some of their kinetic energy to the medium (resulting in absorbed dose) and lose some of their energy in the form of radiative losses (bremsstrahlung, annihilation in flight). The absorbed dose is related to the stochastic quantity energy imparted. The absorbed dose is defined as the mean energy $\bar{\varepsilon}$ imparted by ionizing radiation to matter of mass m in a finite volume V by:

$$D = \frac{d\bar{\varepsilon}}{dm} \tag{3.8}$$

The energy imparted $\bar{\varepsilon}$ is the sum of all the energy entering the volume of interest minus all the energy leaving the volume, taking into account any mass/ energy conversion within the volume. Pair production, for example, decreases the energy by 1.022 MeV, while electron–positron annihilation increases the energy by the same amount [1,2,3,4].

Note that because electrons travel in the medium and deposit energy along their tracks, this absorption of energy does not take place at the same location as the transfer of energy described by kerma. The unit of absorbed dose is joule per kilogram (J/kg). The name for the unit of absorbed dose is the gray (Gy).

3.6. STOPPING POWER

Stopping powers are widely used in radiation dosimetry, but they are rarely measured and must be calculated from theory. For electrons and positrons the Bethe theory is used to calculate stopping powers.

The linear stopping power is defined as the expectation value of the rate of energy loss per unit path length (dE/dx) of the charged particle. The mass stopping power is defined as the linear stopping power divided by the density of the absorbing medium. Division by the density of the absorbing medium almost eliminates the dependence of the mass

stopping power on mass density, except for the density effect discussed further below. Typical units for the linear and mass stopping powers are MeV/cm and MeV·cm^2/g, respectively.

Two types of stopping power are known: collision (ionization), resulting from interactions of charged particles with atomic orbital electrons; and radiative, resulting from interactions of charged particles with atomic nuclei. The unrestricted mass collision stopping power expresses the average rate of energy loss by a charged particle in all hard and soft collisions.

- A soft collision occurs when a charged particle passes an atom at a considerable distance (i.e. $b >> a$, where b is the impact parameter and a the atomic radius). The net effect of the collision is that a very small amount of energy is transferred to an atom of the absorbing medium in a single collision.
- In a hard collision where $b \approx a$, a secondary electron (often referred to as a delta electron or historically as a delta ray) with considerable energy is ejected and forms a separate track.
- In the unrestricted mass collision stopping power the maximum energy transfer to an orbital electron allowed due to a hard collision is half of the kinetic energy of the electron (collision of indistinguishable particles) or the full kinetic energy of a positron (collision of distinguishable particles).

The theory of the mass collision stopping power for heavy charged particles, electrons and positrons as a result of soft and hard collisions combines the Bethe theory for soft collisions with the stopping power as a result of energy transfers due to hard collisions. The result of this, for a heavy charged particle with mass M and velocity v, where the energy transfer due to hard collisions is limited to $2m_e c^2\beta^2/(1-\beta^2)$, $(\beta = v/c)$, is:

$$\frac{S_{col}}{\rho} = \frac{4\pi N_A Z}{A}\frac{r_e^2 m_e c^2}{\beta^2} z^2 \left[\ln\left(\frac{2m_e v^2}{I}\right) - \ln(1-\beta^2) - \beta^2 - \frac{C}{Z} \right] \qquad (3.9)$$

where:

r_e is the classical electron radius (2.82 fm);

z is the projectile charge in units of electron charge;

I is the mean excitation potential of the medium;

C/Z is the shell correction.

The mean excitation potential I is a geometric mean value of all ionization and excitation potentials of an atom of the absorbing material. Since binding effects influence the exact value of I, calculation models are often inadequate to estimate its value accurately. Hence, I values are usually derived from measurements of stopping powers in heavy charged particle beams, for which the effects of scattering in these measurements is minimal.

For elemental materials I varies approximately linearly with Z, with, on average, $I = 11.5Z$. For compounds, I is calculated assuming additivity of the collision stopping power, taking into account the fraction by weight of each atom constituent in the compound.

The shell correction C/Z accounts for the decrease in mass stopping power when the passing particle's velocity has ceased to be much greater than that of the atomic electrons in the stopping medium, an effect that leads to a violation of the Born approximation, which underlies the derivation of the mass collision stopping power. The electrons in the K shell are the first affected by this, followed by the L shell electrons, etc. C/Z is a function of the medium and of the velocity of the fast charged particle.

The following observations can be made about Eq. (3.9):

- The mass stopping power does not depend on the projectile mass and is proportional to the inverse square of the projectile velocity. Note that the

term $2mev^2$ under the logarithm has no relation to the kinetic energy of any of the particles involved in the collision process [1,2].

● The mass stopping power gradually flattens to a broad minimum for kinetic energies $E_K \approx 3m_ec^2$.

● The leading factor Z/A is responsible for a decrease of about 20% in stopping power from carbon to lead. The term –ln I causes a further decrease in stopping power with Z.

● In a given medium, the square dependence on the projectile charge (z^2) causes heavy charged particles with double the charge to experience four times the stopping power

For electrons and positrons, energy transfers due to soft collisions are combined with those due to hard collisions using the Møller (for electrons) and Bhabba (for positrons) cross-sections for free electrons. The complete mass collisional stopping power for electrons and positrons, according to ICRU Report No. 37 [5], is:

$$\frac{S_{col}}{\rho} = \frac{N_A Z}{A}\frac{\pi r_0^2 2m_e c^2}{\beta^2}\left[\ln\left(E_K / I\right)^2 + \ln(1+\tau/2) + F\pm(\tau) - \delta\right] \qquad (3.10)$$

with F^- given for electrons as:

$$F^-(\tau) = (1-\beta^2)\left[1+\tau^2/8-(2\tau+1)\ln 2\right]$$

and F+ given for positrons as:

$$F^+(\tau) = 2\ln 2 - (\beta^2/12)\left[23+14/(\tau+2)+10/(\tau+2)^2+4/(\tau+2)^3\right]$$

In this equation, t = E_K/mec_2 and β = v/c.

The density effect correction d accounts for the fact that the effective Coulomb force exerted on a fast charged particle by atoms that are distant from the particle track is reduced as a result of the polarization of the medium caused by the char- ged particle. The density effect affects the soft collision component of the stopping power. It plays a

significant role in the values of ratios of the stopping power of a dense material to that of a non-dense material (such as, for example, water to air), and various models for it have been developed.

The mass radiative stopping power is the rate of energy loss by electrons or positrons that results in the production of bremsstrahlung. The Bethe–Heitler theory leads to the following formula for the mass radiative stopping power:

$$\frac{S_{rad}}{\rho} = \sigma_0 \frac{N_A Z^2}{A}(E_k + m_e c^2)\overline{B}_r \qquad (3.11)$$

where $\sigma = \alpha(e^2/(4\pi\varepsilon_0 mec^2))^2 = 5.80 \times 10^{-28}$ cm^2/atom, where α is the fine structure constant and $\overline{B_r}$ is a function of Z and E_K, varying between 5.33 and 15 for energies in the range from less than 0.5 MeV to 100 MeV.

This factor, together with the increase of the radiative stopping power proportional with E_K, is responsible for the increase in total stopping power at energies above 2 MeV as depicted in Fig. 3.2. Note that the Z^2 dependence of the mass radiative stopping power in contrast to the Z dependence of the mass collision stopping power makes this mode of energy loss more prominent in high Z materials.

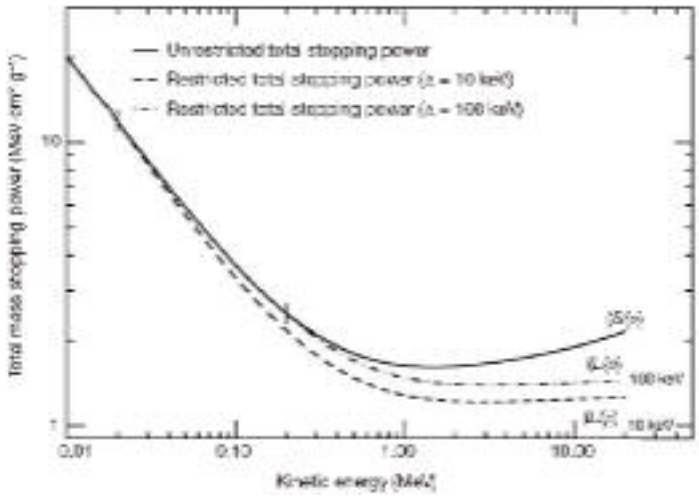

FIG. 3.2. Unrestricted S/ρ and restricted ((L/ρ)$_\Delta$ with Δ = 10 and 100 keV) total mass stopping powers for carbon (ρ = 1.70 g/cm^3), based on data published in ICRU Report No. 37. Vertical lines indicate the points at which restricted and unrestricted mass stopping powers begin to diverge as the kinetic energy increases.

The concept of restricted mass collision stopping power is introduced to calculate the energy transferred to a localized region of interest. By limiting the energy transfer to secondary charged (delta) particles to a threshold (often denoted as D), highly energetic secondary particles are allowed to escape the region of interest.

The restricted stopping power is lower than the unrestricted stopping power. The choice of the energy threshold depends on the problem at hand [5]. For problems involving ionization chambers a frequently used threshold value is 10 keV (the range of a 10 keV electron in air is of the order of 2 mm). For microdosimetric quantities one usually takes 100 eV as a reasonable threshold value.

The restricted linear collision stopping power (also referred to as linear energy transfer (LET)) L_Δ of a material, for charged particles, is the quotient of dE_Δ by dl, where $dE\Delta$ is the energy lost by a charged particle due to soft and hard collisions in traversing a distance dl minus the total kinetic energy of the charged particles released with kinetic energies in excess of Δ:

$$L_\Delta = dE_\Delta / dl \qquad (3.12)$$

The restricted mass collision stopping power is the restricted linear collision stopping power divided by the density of the material. As the threshold for maximum energy transfer in the restricted stopping power increases, the restricted mass stopping power tends to the unrestricted mass stopping power for $\Delta \rightarrow E_K/2$. Note also that since energy transfers to secondary electrons are limited to $E_K/2$, unrestricted and restricted electron mass stopping powers are identical for kinetic energies lower than or equal to 2Δ. This is indicated in Fig. 3.2 by vertical lines at 20 keV and 200 keV.

The total mass stopping power is the sum of the collision mass stopping power and the radiative mass stopping power. Fig. 3.2 shows the total unrestricted and restricted (Δ = 10

keV, 100 keV) electron mass stopping powers for carbon, based on data in ICRU Report No. 37 [5].

3.7. RELATIONSHIPS BETWEEN DOSIMETRIC QUANTITIES

3.7.1. Energy fluence and kerma (photons)

The energy transferred to electrons by photons can be expended in two distinct ways:

- Through collision interactions (soft collisions and hard collisions);
- Through radiative interactions (bremsstrahlung and electron–positron annihilation).

The total kerma is therefore usually divided into two components: the collision kerma K_{col} and the radiative kerma K_{rad}.

- The collision kerma K_{col} is that part of kerma that leads to the production of electrons that dissipate their energy as ionization in or near the electron tracks in the medium, and is the result of Coulomb force interactions with atomic electrons. Thus the collision kerma is the expectation value of the net energy transferred to charged particles per unit mass at the point of interest, excluding both the radiative energy loss and energy passed from one charged particle to another.
- The radiative kerma *K*rad is that part of kerma that leads to the production of radiative photons as the secondary charged particles slow down and interact in the medium. These interactions most prominently are bremsstrahlung as a result of Coulomb field interactions between the charged particle and the atomic nuclei, but can also result from annihilation in flight.

The total kerma K is thus given by the following:

$$K = K_{col} + K_{rad} \tag{3.13}$$

The average fraction of the energy transferred to electrons that is lost through radiative processes is represented by a factor referred to as the radiative fraction $\bar{g}$. Hence the fraction lost through collisions is $(1 - \bar{g})$.

A frequently used relation between collision kerma K_{col} and total kerma K may be written as follows:

$$K_{col} = K(1 - \bar{g}) \tag{3.14}$$

For monoenergetic photons the collision kerma K_{col} at a point in a medium is related to the energy fluence Ψ at that point in the medium by the following:

$$K_{col} = \Psi\left(\frac{\mu_{en}}{\rho}\right) \tag{3.15}$$

where (μ_{en}/ρ) is the mass–energy absorption coefficient for the monoenergetic photons in the medium. For polyenergetic beams a formally similar relation exists, but use is made of spectrum averaged quantities. If a photon energy fluence spectrum $\Psi_E(E)$ is present at the point of interest, the collision kerma at that point is obtained as follows:

$$K_{col} = \int_0^{E_{\max}} \Psi_E(E)\left(\frac{\mu_{en}}{\rho}\right) dE = \Psi\left(\frac{\bar{\mu}_{en}}{\rho}\right) \tag{3.16}$$

where the expression:

$\Psi = \int_0^{E_{\max}} \Psi_E(E) dE$ stands for the total (integrated) energy fluence, and:

$\left(\frac{\bar{\mu}_{en}}{\rho}\right) = \frac{1}{\Psi} \int_0^{E_{\max}} \Psi_E(E) \frac{\mu_{en}}{\rho}(E) dE$ is a shorthand notation for the mass–energy absorption coefficient for the medium averaged over the energy fluence spectrum.

For monoenergetic photons the total kerma K at a point in a medium is related to the energy fluence Y in the medium by the following:

$$K = \Psi\left(\frac{\mu_{tr}}{\rho}\right) \tag{3.17}$$

where (μ_{tr}/ρ) is the mass–energy transfer coefficient of the medium for the given monoenergetic photon beam. For polyenergetic beams, similarly as above, spectrum averaged mass–energy transfer coefficients can be used in conjunction with total energy fluence to obtain the total kerma.

Using Eq. (3.15), one can obtain the frequently used relation between collision kerma in two different materials, material 1 and material 2, as follows:

$$\frac{K_{col,2}}{K_{col,1}} = \frac{\Psi_2 \left(\frac{\bar{\mu}_{en}}{\rho} \right)_2}{\Psi_1 \left(\frac{\bar{\mu}_{en}}{\rho} \right)_1} \equiv (\Psi)_{2,1} \left(\frac{\bar{\mu}_{en}}{\rho} \right)_{2,1} \tag{3.18}$$

This equation is often used in circumstances in which the fluence ratio $(\Psi)_{2,1}$ can be assumed to be unity through a proper scaling of dimensions (the scaling theorem), for very similar materials or for situations in which the mass of material 2 is sufficient to provide buildup but at the same time small enough so as not to disturb the photon fluence in material 1 (e.g. dose to a small mass of tissue in air).

3.7.2. Fluence and dose (electrons)

Under the conditions that (a) radiative photons escape the volume of interest and (b) secondary electrons are absorbed on the spot (or there is a charged particle equilibrium (CPE) of secondary electrons), the absorbed dose to medium D_{med} is related to the electron fluence Φ_{med} in the medium as follows:

$$D_{med} = \Phi_{med} \left(\frac{S_{col}}{\rho} \right)_{med} \tag{3.19}$$

where $(S\text{col}/\rho)_{\text{med}}$ is the unrestricted mass collision stopping power of the medium at the energy of the electron.

Owing to electron slowdown in a medium, even for a monoenergetic starting electron kinetic energy E_K, there is always present a primary fluence spectrum that ranges in energy from E_K down to zero and is commonly denoted by $\Phi_{\mathrm{med},E}$.

In this case, the absorbed dose to the medium can be obtained by an integration of Eq. (3.18):

$$D_{med} = \int_0^{E_{\max}} \Phi_{med,E}(E)\left(\frac{S_{col}}{\rho}\right)_{med}(E)dE = \Phi_{med}\left(\frac{\overline{S}_{col}}{\rho}\right)_{med} \tag{3.20}$$

The right hand side of Eq. (3.19) shows that absorbed dose can be calculated using a formally similar equation as Eq. (3.18) by making use of spectrum averaged collision stopping power and total fluence.

Based on Eq. (3.20) and under the same assumptions, for two media, med_1 and med_2, the ratio of absorbed doses can be calculated as:

$$\frac{D_{med_2}}{D_{med_1}} = \left(\Phi\right)_{med_2,med_1}\left(\frac{\overline{S}_{col}}{\rho}\right)_{med_2,med_1} \tag{3.21}$$

where the shorthand notations:

$\left(\Phi\right)_{med_2,med_1}$ and $\left(\frac{\overline{S}_{col}}{\rho}\right)_{med_2,med_1}$ are being used for the ratio of the electron fluences (often referred to as the electron fluence ratio) and the collision stopping powers in the media med_2 and med_1, respectively.

The full, realistic electron fluence spectrum consists of primary charged particles that, for example, are the result of a polyenergetic photon beam interacting in the medium. These primary charged particles are slowed down and result in secondary particle fluence. This fluence thus contains charged particles that result from slowing down through soft collisions as well as hard, knock-on collisions. Electrons created as a result of the latter process are designated delta electrons [3,4].

3.7.3. Kerma and dose (charged particle equilibrium)

Generally, the transfer of energy (kerma) from the photon beam to charged particles at a particular location does not lead to the absorption of energy by the medium (absorbed dose) at the same location. This is due to the non-zero (finite) range of the secondary electrons released through photon interactions.

Since radiative photons mostly escape from the volume of interest, one relates absorbed dose usually to collision kerma. In general, however, the ratio of dose and collision kerma is often denoted as:

$$\beta = D / K_{col} \tag{3.22}$$

If radiative photons escape the volume of interest, an assumption is made that $\beta \approx 1$ [2,4].

Fig. 3.3 illustrates the relation between collision kerma and absorbed dose under buildup conditions; under conditions of CPE in part (a) and under conditions of transient charged particle equilibrium (TCPE) in part (b).

As a high energy photon beam penetrates the medium, collision kerma is maximal at the surface of the irradiated material because photon fluence is greatest at the surface. Initially, the charged particle fluence, and hence the absorbed dose, increases as a function of depth until the depth of dose maximum $z_{\max}$ is attained.

If there were no photon attenuation or scattering in the medium, but yet production of electrons, a hypothetical situation, as illustrated in Fig. 3.3(a), would occur: the buildup region (with $\beta < 1$) is followed by a region of complete CPE where $D = K_{\text{col}}$ (i.e. $\beta = 1$).

In the more realistic situation, however, due to photon attenuation and scattering in the medium, a region of TCPE occurs (Fig. 3.3(b)) where there exists an essentially constant relation between collision kerma and absorbed dose. This relation is practically constant since, in high energy photon beams, the average energy of the generated electrons and hence their range does not change appreciably with depth in the medium.

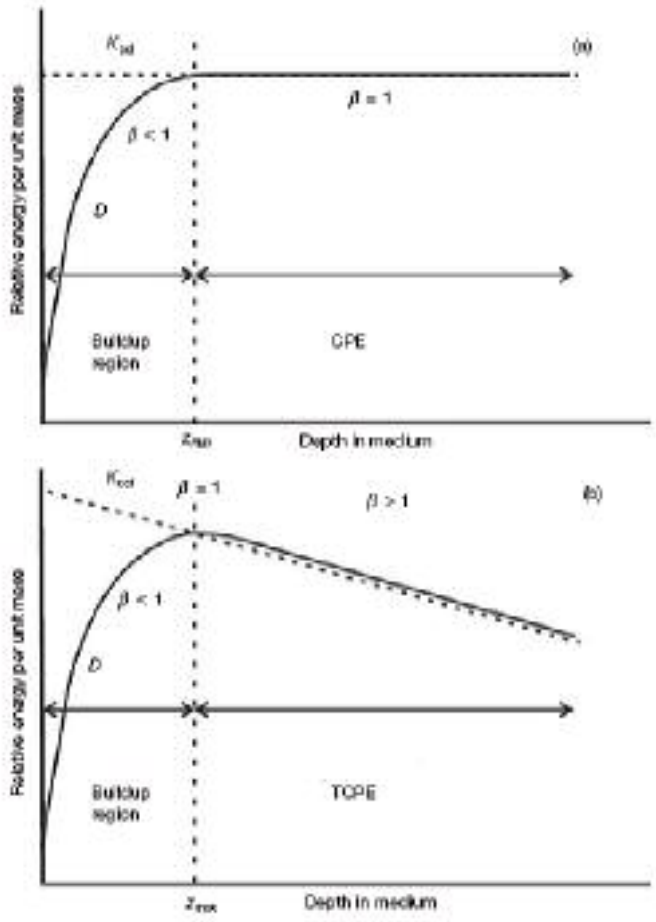

Fig. 3.3. Collision kerma and absorbed dose as a function of depth in a medium irradiated by a high energy photon beam for (a) the hypothetical case of no photon attenuation or scattering and for (b) the realistic case.

In the special case in which true CPE exists (at the depth of maximum dose in the medium), the relation between absorbed dose D and total kerma K is given by:

$$D = K_{col} = K(1 - \bar{g}) \tag{3.23}$$

where $\bar{g}$ is the radiative fraction, depending on the electron kinetic energy; the higher the energy, the larger is $\bar{g}$. The radiative fraction also depends on the material considered, with higher values of g— for higher Z materials. For electrons produced by ^{60}Co rays in air the radiative fraction equals 0.0032. The buildup of absorbed dose is responsible for the skin sparing effect in the case of high energy photon beams. However, in practice the surface dose is small but does not equal zero because of the electron contamination in the beam due to photon interactions in the media upstream from the

phantom or due to charged particles generated in the accelerator head and beam modifying devices.

3.7.4. Collision kerma and exposure

Exposure X is the quotient of dQ by dm, where dQ is the absolute value of the total charge of the ions of one sign produced in air when all the electrons and positrons liberated or created by photons in mass dm of air are completely stopped in air:

$$X = \frac{dQ}{dm} \tag{3.24}$$

The unit of exposure is coulomb per kilogram (C/kg). The unit used for exposure is the roentgen R, where 1 R = 2.58 × 10–4 C/kg. In the SI system of units, roentgen is no longer used and the unit of exposure is simply 2.58×10^{-4} C/kg of air.

The average energy expended in air per ion pair formed W_{air} is the quotient of E_K by N, where N is the mean number of ion pairs formed when the initial kinetic energy E_K of a charged particle is completely dissipated in air:

$$W_{air} = \frac{E}{N} \tag{3.25}$$

The current best estimate for the average value of W_{air} is 33.97 eV/ion pair or 33.97 × 1.602 × 1019 J/ion pair:

$$\frac{W_{air}}{e} = \frac{33.97(eV/ionpair)\times 1.602\times 10^{-19}(j/eV)}{1.602\times 10^{-19}} = 33.97 J/C \tag{3.26}$$

Multiplying the collision kerma by (e/Wair), the number of coulombs of charge created per joule of energy deposited, gives the charge created per unit mass of air or exposure:

$$X = (K_{col})_{air}\left(\frac{e}{W_{air}}\right) \tag{3.27}$$

The relation between total kerma and exposure is obtained by combining Eqs (3.23) and (3.26).

3.8. CAVITY THEORY

In order to measure the absorbed dose in a medium, it is necessary to introduce a radiation sensitive device (dosimeter) into the medium. Generally, the sensitive medium of the dosimeter will not be of the same material as the medium in which it is embedded.

Cavity theory [1] relates the absorbed dose in the dosimeter's sensitive medium (cavity) to the absorbed dose in the surrounding medium containing the cavity. Cavity sizes are referred to as small, intermediate or large in comparison with the ranges of secondary charged particles produced by photons in the cavity medium. If, for example, the range of charged particles (electrons) is much larger than the cavity dimensions, the cavity is regarded as small. Various cavity theories for photon beams have been developed, which depend on the size of the cavity; for example, the Bragg–Gray and Spencer–Attix theories for small cavities and the Burlin theory for cavities of intermediate sizes.

3.8.1. Bragg–Gray cavity theory

The Bragg–Gray cavity theory was the first cavity theory developed to provide a relation between the absorbed dose in a dosimeter and the absorbed dose in the medium containing the dosimeter [1].

The conditions for application of the Bragg–Gray cavity theory are:

(a) The cavity must be small when compared with the range of charged particles incident on it, so that its presence does not perturb the fluence of charged particles in the medium;

(b) The absorbed dose in the cavity is deposited solely by charged particles crossing it (i.e. photon interactions in the cavity are assumed negligible and thus ignored).

The result of condition (a) is that the electron fluences in Eq. (2.22) are the same and equal to the equilibrium fluence established in the surrounding medium. This condition can only be valid in regions of CPE or TCPE. In addition, the presence of a cavity always causes some degree of fluence perturbation that requires the introduction of a fluence perturbation correction factor. Condition (b) implies that all electrons depositing the dose inside the cavity are produced outside the cavity and completely cross the cavity. No secondary electrons are therefore produced inside the cavity and no electrons stop within the cavity.

Under these two conditions, according to the Bragg–Gray cavity theory, the dose to the medium D_{med} is related to the dose in the cavity D_{cav} as follows:

$$D_{med} = D_{cav}\left(\frac{\overline{S}}{\rho}\right)_{med,cav} \tag{3.28}$$

where $(\overline{S}/\rho)_{med,cav}$ is the ratio of the average unrestricted mass collision stopping powers of the medium and the cavity. The use of unrestricted stopping powers rules out the production of secondary charged particles (or delta electrons) in the cavity and the medium. Although the cavity size is not explicitly taken into account in the Bragg– Gray cavity theory, the fulfilment of the two Bragg–Gray conditions will depend on the cavity size, which is based on the range of the electrons in the cavity medium, the cavity medium and the electron energy. A cavity that qualifies as a Bragg–Gray cavity for high energy photon beams, for example, may not behave as a Bragg–Gray cavity in a medium energy or low energy X ray beam.

3.8.2. Spencer–Attix cavity theory

The Bragg–Gray cavity theory does not take into account the creation of secondary (delta) electrons generated as a result of hard collisions in the slowing down of the primary electrons in the sensitive volume of the dosimeter.

The Spencer–Attix cavity theory [1] is a more general formulation that accounts for the creation of these electrons that have sufficient energy to produce further ionization on their own account. Some of these electrons released in the gas cavity would have sufficient energy to escape from the cavity, carrying some of their energy with them. This reduces the energy absorbed in the cavity and requires modification of the stopping power of the gas. The Spencer–Attix theory operates under the two Bragg–Gray conditions; however, these conditions now even apply to the secondary particle fluence in addition to the primary particle fluence.

The secondary electron fluence in the Spencer–Attix theory is divided into two components based on a user defined energy threshold Δ. Secondary electrons with kinetic energies E_K less than Δ are considered slow electrons that deposit their energy locally; secondary electrons with energies larger than or equal to Δ are considered fast (slowing down) electrons and are part of the electron spectrum. Consequently, this spectrum has a low energy threshold of Δ and a high energy threshold of E_{K0}, where E_{K0} represents the initial electron kinetic energy. Since the lowest energy in the spectrum is Δ, the maximum energy loss of a fast electron with kinetic energy E_K larger than or equal to 2Δ cannot be larger than Δ, and the maximum energy loss of a fast electron with kinetic energy less than 2Δ cannot be larger than $E_K/2$ (where $\Delta \leq E\mathrm{K} < 2\Delta$).

The energy deposition must be calculated as the product of $L_\Delta(E_K)/\rho$, the restricted collision stopping power with threshold Δ, and , the fast electron fluence ranging in energy from Δ to E_{K0} (e-e stands for the contribution of delta electrons in the slowing down spectrum).

Owing to the Bragg–Gray condition, which stipulates that there must not be electron production in the cavity, the electrons with energy Δ must be capable of crossing the

cavity. The threshold value Δ is hence related to the cavity size and is defined as the energy of the electron with a range equal to the mean chord length across the cavity.

The Spencer–Attix relation between the dose to the medium and the dose in the cavity is thus written as:

$$D_{med} / D_{cav} = s_{med,cav} \tag{3.29}$$

where $s_{med,cav}$ is the ratio of the mean restricted mass collision stopping powers of the medium to that of the cavity.

Using the medium electron fluence spectrum $\Phi^{e-e}_{med,E_k}(E_k)$, the full expression is:

$$s_{med,cav} = \frac{\int_{\Delta}^{E_{k0}} \Phi^{e-e}_{med,E_k}(E_K)(L_{\Delta,med}/\rho)d(E_K) + TE_{med}}{\int_{\Delta}^{E_{k0}} \Phi^{e-e}_{med,E_k}(E_K)(L_{\Delta,cav}/\rho)d(E_K) + TE_{cav}} \tag{3.30}$$

The terms TE_{med} and TE_{cav} are called the track end terms and account for a part of the energy deposited by electrons with initial kinetic energies between Δ and 2Δ. These electrons can have an energy loss that brings their kinetic energy to lower than Δ. Their residual energy after such events should be deposited on the spot, and these electrons are removed from the spectrum. The track end terms are approximated by Nahum as:

$$TE_{med} = \Phi^{e-e}_{med,E_K}(\Delta)\frac{S_{med}(\Delta)}{\rho}\Delta \tag{3.31}$$

and

$$TE_{cav} = \Phi^{e-e}_{med,E_K}(\Delta)\frac{S_{cav}(\Delta)}{\rho}\Delta \tag{3.32}$$

The unrestricted collision stopping powers can be used here because the maximum energy transfer for an electron with energy less than 2D is less than Δ.

Monte Carlo calculations have shown that the difference between the Spencer–Attix and Bragg–Gray cavity theories is non-negligible yet generally not very significant. Since

collision stopping powers for different media show similar trends as a function of particle energy, their ratio for the two media is a very slowly varying function with energy.

The value of the stopping power water to air ratio for ionization chambers is only weakly dependent on the choice of the cut-off energy. For Farmer type chambers and for parallel-plate chambers used in radiotherapy physics a nominal value of 10 keV is often used.

For a typical ionization chamber used in water, the energy dependence of the stopping power water to air ratio arises mainly from the difference in the density effect correction between the two materials.

3.8.3. Considerations in the application of cavity theory to ionization chamber calibration and dosimetry protocols

A dosimeter can be defined generally as any device that is capable of providing a reading that is a measure of the average absorbed dose deposited in its (the dosimeter's) sensitive volume by ionizing radiation. A dosimeter can generally be considered as consisting of a sensitive volume filled with a given medium, surrounded by a wall of another medium. In the context of cavity theories, the sensitive volume of the dosimeter can be identified as the 'cavity', which may contain a gaseous, liquid or solid medium.

Gas is often used as the sensitive medium, since it allows a relatively simple electrical means for collection of charges released in the sensitive medium by radiation.

The medium surrounding the cavity of an ionization chamber depends on the situation in which the device is used. In an older approach, the wall (often supplemented with a buildup cap) serves as the buildup medium and the Bragg–Gray theory provides a relation between the dose in the gas and the dose in the wall. This is referred to as a thick walled ionization chamber and forms the basis of cavity chamber based air kerma in-air standards and of the C_λ based dosimetry protocols of the 1970s. If, however, the chamber is used in a phantom without a buildup material, since typical wall thicknesses are much

thinner than the range of the secondary electrons, the proportion of the cavity dose due to electrons generated in the phantom greatly exceeds the dose contribution from the wall, and hence the phantom medium serves as the medium and the wall is treated as a perturbation to this concept.

In the case of a thick walled ionization chamber in a high energy photon beam, the wall thickness must be greater than the range of secondary electrons in the wall material to ensure that the electrons that cross the cavity arise in the wall and not in the medium. The Bragg–Gray cavity equation then relates the dose in the cavity to the dose in the wall of the chamber. The dose in the medium is related to the dose in the wall by means of a ratio of the mass– energy absorption coefficients of the medium and the wall $(\overline{\mu}_{en}/\rho)_{med,wall}$ by assuming that:

(a) The absorbed dose is the same as the collision kerma;

(b) The photon fluence is not perturbed by the presence of the chamber;

the dose to the cavity gas is related to the ionization produced in the cavity as follows:

$$D_{gas} = \frac{Q}{m}\left(\overline{\frac{W_{gas}}{e}}\right) \tag{3.33}$$

where Q is the charge (of either sign) produced in the cavity and m is the mass of the gas in the cavity.

Spencer–Attix cavity theory can be used to calculate the dose in the medium as:

$$D_{med} = D_{wall}\left(\overline{\frac{\mu_{en}}{\rho}}\right)_{med,wall} = D_{gas}s_{wall,gas}\left(\frac{\overline{\mu}_{en}}{\rho}\right)_{med,wall} = \frac{Q}{m}\left(\frac{\overline{W}_{gas}}{e}\right)s_{wall,gas}\left(\frac{\overline{\mu}_{en}}{\rho}\right)_{med,wall} \tag{3.34}$$

where $s_{wall,gas}$ is the ratio of restricted mass collision stopping powers for a cavity wall and gas with threshold Δ. In practice, there are additional correction factors associated with Eq. (4.34) to satisfy assumptions (a) and (b) made above.

A similar equation to Eq. (4.34) is used for air kerma in-air calibrations; however, here the quantity of interest is not the dose to the medium, but the air kerma in air. In this case,

a substantial wall correction is introduced to ensure the presence of complete CPE in the wall to satisfy assumption (a) above.

In the case of a thin walled ionization chamber in a high energy photon or electron beam, the wall, cavity and central electrode are treated as a perturbation to the medium fluence, and the equation now involves the ratio of restricted collision stopping powers of the medium to that of the gas $s_{med,gas}$ as:

$$D_{med} = \frac{Q}{m}\left(\frac{\overline{W}_{gas}}{e}\right) s_{med,gas}\, p_{fl}\, p_{dis}\, p_{wall}\, p_{cel} \qquad (3.35)$$

Where:

p_{fl} is the electron fluence perturbation correction factor;

p_{dis} is the correction factor for displacement of the effective measurement point;

p_{wall} is the wall correction factor;

p_{cel} is the correction factor for the central electrode.

Values for these multiplicative correction factors are summarized for photon and electron beams in typical dosimetry protocols.

3.8.4. Large cavities in photon beams

A large cavity is a cavity with dimensions such that the dose contribution made by electrons inside the cavity originating from photon interactions outside the cavity can be ignored when compared with the contribution of electrons created by photon interactions within the cavity.

For a large cavity the ratio of dose cavity to medium is calculated as the ratio of the collision kerma in the cavity to the medium and is therefore equal to the ratio of the average mass–energy absorption coefficients of the cavity gas to that of the medium $(\overline{\mu}/\rho)_{gas,med}$:

$$\frac{D_{gas}}{D_{med}} = \left(\frac{\overline{\mu_{en}}}{\rho} \right)_{gas,med} \tag{3.36}$$

where the mass–energy absorption coefficients have been averaged over the photon fluence spectra in the cavity gas (numerator) and in the medium (denominator).

3.8.5. Burlin cavity theory for photon beams

Burlin extended the Bragg–Gray and Spencer–Attix cavity theories to cavities of intermediate dimensions by introducing, on a purely phenomenological basis, a large cavity limit to the Spencer–Attix equation using a weighting technique. He provided a formalism to calculate the value of the weighting parameter.

The Burlin cavity theory can be written in its simplest form as follows:

$$\frac{D_{gas}}{D_{med}} = ds_{gas,med} + (1-d)\left(\frac{\overline{\mu_{en}}}{\rho} \right)_{gas,med} \tag{3.37}$$

where

d is a parameter related to cavity size, approaching unity for small cavities and zero for large cavities;

$s_{gas,med}$ is the mean ratio of the restricted mass stopping powers of the cavity and the medium;

D_{gas} is the absorbed dose in the cavity;

$(\overline{\mu}_{en}/\rho)_{gas,med}$ is the mean ratio of the mass–energy absorption coefficients for the cavity and the medium.

The Burlin theory effectively requires that:

- The surrounding medium and the cavity medium be homogeneous;
- A homogeneous photon field exist everywhere throughout the medium and the cavity;

● CPE exist at all points in the medium and the cavity that are further than the maximum electron range from the cavity boundary;

● The equilibrium spectra of secondary electrons generated in the medium and the cavity be the same.

Burlin provided a method for estimating the weighting parameter d in his theory. It is expressed as the average value of the electron fluence reduction in the medium. Consistent with experiments with b sources he proposed that the electron fluence in the medium Φ_{med}^{e-e} decays, on average, exponentially. The value of the weighting parameter d in conjunction with the stopping power ratio can be calculated as:

$$d = \frac{\int_0^L \Phi_{med}^{e-e} e^{-\beta} dl}{\int_0^L \Phi_{med}^{e-e} dl} = \frac{1 - e^{-\beta L}}{\beta L} \tag{3.38}$$

where β is an effective electron fluence attenuation coefficient that quantifies the reduction in particle fluence from its initial medium fluence value through a cavity of average length L. For convex cavities and isotropic electron fluence distributions, L can be calculated as $4V/S$, where V is the cavity volume and S its surface area. Burlin described the buildup of the electron fluence Φ_{gas}^{e-e} inside the cavity using a similar, complementary equation:

$$1 - d = \frac{\int_0^L \Phi_{gas}^{e-e} (1 - e^{-\beta l}) dl}{\int_0^L \Phi_{gas}^{e-e} dl} = \frac{\beta L - 1 + e^{-\beta L}}{\beta L} \tag{3.39}$$

Burlin's theory is consistent with the fundamental constraint of cavity theory: that the weighting factors of both terms add up to unity (i.e. d and $1 - d$). It had relative success in calculating ratios of absorbed dose for some types of intermediate cavities. More generally, however, Monte Carlo calculations show that, when studying ratios of directly

calculated absorbed doses in the cavity to absorbed dose in the medium as a function of cavity size, the weighting method is too simplistic and additional terms are necessary to calculate dose ratios for intermediate cavity sizes. For these and other reasons, the Burlin cavity theory is no longer used in practice.

3.8.6. Stopping power ratios

Although cavity theory was designed to calculate ratios of absorbed doses, the practical application of the Spencer–Attix cavity theory has always required additional correction factors. Since the central component of the Spencer–Attix cavity theory results in averaging stopping powers, Spencer–Attix dose ratios are often referred to as 'stopping power ratios'.

In photon beams, except at or near the surface, average restricted stopping power ratios of water to air do not vary significantly as a function of depth. Stopping power ratios (with Δ = 10 keV) under full buildup conditions are shown in Table 3.1. Stopping power ratios not only play a role in the absolute measurement of absorbed dose, they are also relevant in performing accurate relative measurements of absorbed dose in regimes in which the energy of the secondary electrons changes significantly from one point in a phantom to another. An important example of this is apparent from Fig. 3.4, which shows restricted stopping power ratios (Δ = 10 keV) of water to air for electron beams as a function of depth in water.

Photon spectrum	$s_{water,air}$
^{60}Co	1.134
4 MV	1.131
6 MV	1.127
8 MV	1.121
10 MV	1.117
15 MV	1.106
20 MV	1.096
25 MV	1.093
35 MV	1.084

Table 3.1. Average restricted stopping power ratio of water to air, $s_{water,air}$, for different photon spectra in the range from ^{60}Co γ rays to 35 MV X rays

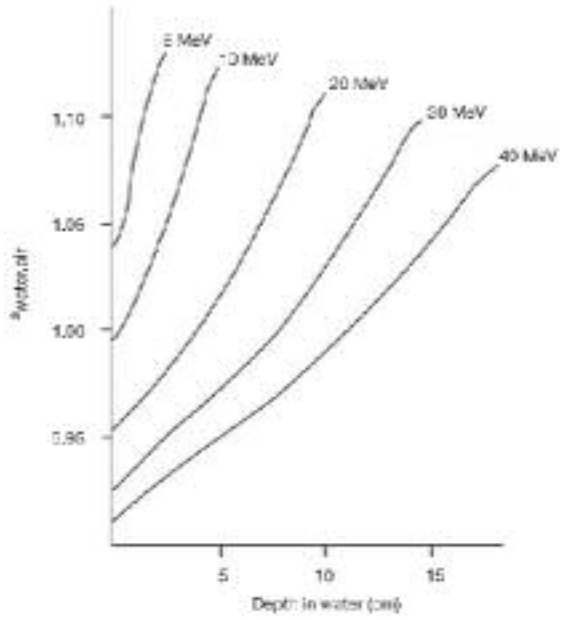

FIG. 3.4. Restricted collision stopping power water to air ratio (D = 10 keV) as a function of depth for different monoenergetic electron energies.

Note that these curves are for monoenergetic electrons; protocols or codes of practice for electron dosimetry provide fits of stopping power ratios for realistic accelerator beams. However, Fig. 3.4 shows clearly that the accurate measurement of electron beam depth dose curves requires depth dependent correction factors.

Bibliography

[1] Attix, F.H., *Introduction to Radiological Physics and Radiation Dosimetry*, Wiley, New York (1986).

[2] Greening. J.R*., Fundamentals of Radiation Dosimetry*, Adam Hilger, Bristol (1981).

[3] INTERNATIONAL COMMISSION ON RADIATION UNITS AND MEASUREMENTS, *Stopping Powers for Electrons and Positrons*, Rep. 37, ICRU, Bethesda, MD (1984).

[4] *Fundamental Quantities and Units for Ionizing Radiation*, Rep. 60, ICRU, Bethesda, MD (1998).

[5] Johns, H.E., Cunningham, J.R., *The Physics of Radiology*, Thomas, Springfield, IL (1985).

[6] Khan, F.M., *The Physics of Radiation Therapy*, Lippincott, Williams and Wilkins, Baltimore, MD (2003).

Chapter 4

RADIATION DOSIMETERS

4.1. INTRODUCTION

A radiation dosimeter is a device, instrument or system that measures or evaluates, either directly or indirectly, the quantities exposure, kerma, absorbed dose or equivalent dose, or their time derivatives (rates), or related quantities of ionizing radiation. A dosimeter along with its reader is referred to as a dosimetry system.

Measurement of a dosimetric quantity is the process of finding the value of the quantity experimentally using dosimetry systems. The result of a measurement is the value of a dosimetric quantity expressed as the product of a numerical value and an appropriate unit.

To function as a radiation dosimeter, the dosimeter must possess at least one physical property that is a function of the measured dosimetric quantity and that can be used for radiation dosimetry with proper calibration. In order to be useful, radiation dosimeters must exhibit several desirable characteristics. For example, in radiotherapy exact knowledge of both the absorbed dose to water at a specified point and its spatial distribution are of importance, as well as the possibility of deriving the dose to an organ of interest in the patient. In this context, the desirable dosimeter properties will be characterized by accuracy and precision, linearity, dose or dose rate dependence, energy response, directional dependence and spatial resolution.

Obviously, not all dosimeters can satisfy all characteristics. The choice of a radiation dosimeter and its reader must therefore be made judiciously, taking into account the requirements of the measurement situation; for example, in radiotherapy ionization chambers are recommended for beam calibrations and other dosimeters, such as those discussed below, are suitable for the evaluation of the dose distribution (relative dosimetry) or dose verification.

4.2. PROPERTIES OF DOSIMETERS

4.2.1. Linearity

Ideally, the dosimeter reading should *M* be linearly proportional to the dosimetric quantity to be read *Q*. However, beyond a certain dose range a non-linearity sets in. The linearity range and the non-linearity behaviour depend on the type of dosimeter and its physical characteristics [1,2].

Two typical examples of response characteristics of dosimetry systems are shown in Fig. 4.1. Curve A first exhibits linearity with dose, then a supralinear behaviour, and finally saturation. Curve B first exhibits linearity and then saturation at high doses.

In general, a non-linear behaviour should be corrected for. A dosimeter and its reader may both exhibit non-linear characteristics, but their combined effect could produce linearity over a wider range.

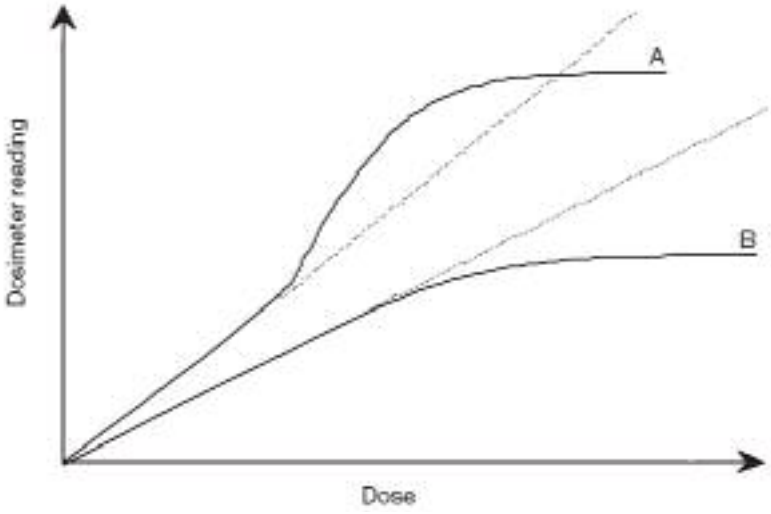

FIG. 4.1. ***Response characteristics of two dosimetry systems. Curve A first exhibits linearity with dose, then supralinear behaviour and finally saturation. Curve B first exhibits linearity and then saturation at high doses.***

4.2.2. Dose rate dependence

Integrating systems measure the integrated response of a dosimetry system. For such systems the measured dosimetric quantity should be independent of the rate of that quantity.

Ideally, the response of a dosimetry system M/Q at two different dose rates $((dQ/dt)_1$ and $(dQ/dt)_2)$ should remain constant. In reality, the dose rate may influence the dosimeter readings and appropriate corrections are necessary, for example recombination corrections for ionization chambers in pulsed beams.

4.2.3. Energy dependence

The response of a dosimetry system M/Q is generally a function of radiation beam quality (energy). Since the dosimetry systems are calibrated at a specified radiation beam quality (or qualities) and used over a much wider energy range, the variation of the response of a dosimetry system with radiation quality (called energy dependence) requires correction.

Ideally, the energy response should be flat (i.e. the system calibration should be independent of energy over a certain range of radiation qualities). In reality, the energy correction has to be included in the determination of the quantity Q for most measurement situations. In radiotherapy, the quantity of interest is the dose to water (or to tissue). As no dosimeter is water or tissue equivalent for all radiation beam qualities, the energy dependence is an important characteristic of a dosimetry system.

4.2.4. Directional dependence

The variation in response of a dosimeter with the angle of incidence of radiation is known as the directional, or angular, dependence of the dosimeter.

Dosimeters usually exhibit directional dependence, due to their constructional details, physical size and the energy of the incident radiation. Directional dependence is important in certain applications, for example in *in vivo* dosimetry while using semiconductor dosimeters. Therapy dosimeters are generally used in the same geometry as that in which they are calibrated.

4.2.5. Spatial resolution and physical size

Since the dose is a point quantity, the dosimeter should allow the determination of the dose from a very small volume (i.e. one needs a "point dosimeter" to characterize the dose at a point). The position of the point where the dose is determined (i.e. its spatial location) should be well defined in a reference coordinate system.

Thermoluminescent dosimeters (TLDs) come in very small dimensions and their use, to a great extent, approximates a point measurement. Film dosimeters have excellent 2-D and gels 3-D resolution, where the point measurement is limited only by the resolution of the evaluation system [2].

Ionization chamber type dosimeters, however, are of finite size to give the required sensitivity, although the new type of pinpoint microchambers partially overcomes the problem.

4.2.6. Readout convenience

Direct reading dosimeters (e.g. ionization chambers) are generally more convenient than passive dosimeters (i.e. those that are read after due processing following the exposure, for example TLDs and films). While some dosimeters are inherently of the integrating type (e.g. TLDs and gels), others can measure in both integral and differential modes (ionization chambers).

4.2.7. Convenience of use

Ionization chambers are reusable, with no or little change in sensitivity within their lifespan. Semiconductor dosimeters are reusable, but with a gradual loss of sensitivity within their lifespan; however, some dosimeters are not reusable (e.g. films, gels and alanine).

Some dosimeters measure dose distribution in a single exposure (e.g. films and gels) and some dosimeters are quite rugged (i.e. handling will not influence sensitivity, for example ionization chambers), while others are sensitive to handling (e.g. TLDs).

4.3. IONIZATION CHAMBERS DOSIMETRY SYSTEMS

4.3.1. Chambers and electrometers

Ionization chambers are used in radiotherapy and in diagnostic radiology for the determination of radiation dose. The dose determination in reference irradiation conditions is also called beam calibration. Ionization chambers come in various shapes and sizes, depending upon the specific requirements, but generally they all have the following properties:

- An ionization chamber is basically a gas filled cavity surrounded by a conductive outer wall and having a central collecting electrode (Fig.4.3). The wall and the collecting electrode are separated with a high quality insulator to reduce the leakage current when a polarizing voltage is applied to the chamber.
- A guard electrode is usually provided in the chamber to further reduce chamber leakage. The guard electrode intercepts the leakage current and allows it to flow to ground, bypassing the collecting electrode. It also ensures improved field uniformity in the active or sensitive volume of the chamber, with resulting advantages in charge collection.
- Measurements with open air ionization chambers require temperature and pressure correction to account for the change in the mass of air in the chamber volume, which changes with the ambient temperature and pressure.

Electrometers are devices for measuring small currents, of the order of 10^{-9} A or less. An electrometer used in conjunction with an ionization chamber is a high gain, negative feedback, operational amplifier with a standard resistor or a standard capacitor in the feedback path to measure the chamber current or charge collected over a fixed time interval, as shown schematically in Fig.4.2.

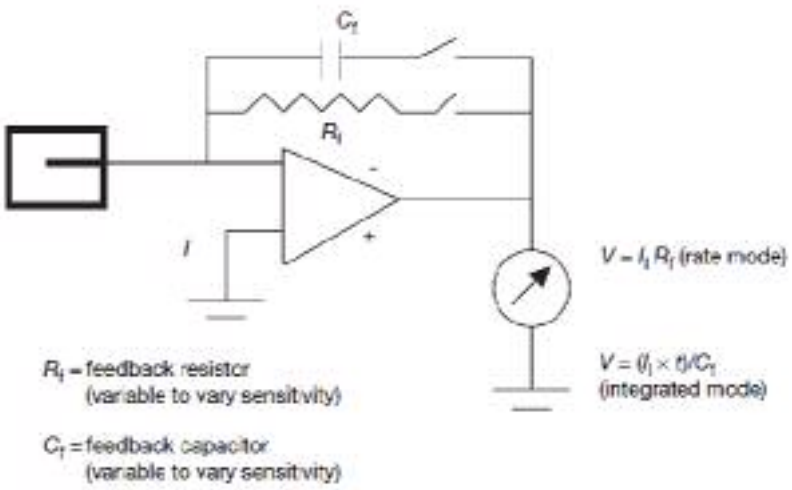

FIG. 4.2. ***Electrometer in feedback mode of operation.***

4.3.2. Cylindrical (thimble type) ionization chambers

The most popular cylindrical ionization chamber is the 0.6 cm^3 chamber designed by Farmer and originally manufactured by Baldwin, but now available from several vendors, for beam calibration in radiotherapy dosimetry. Its chamber sensitive volume resembles a thimble, and hence the Farmer type chamber is also known as a thimble chamber. A schematic diagram of a Farmer type thimble ionization chamber is shown in Fig. 4.3.

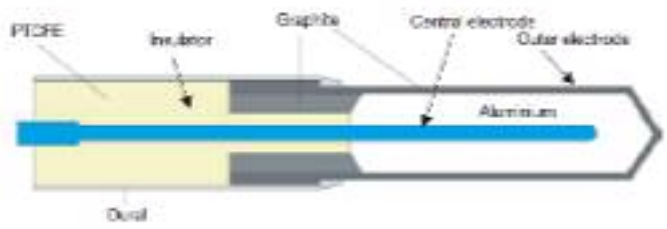

FIG. 4.3. ***Basic design of a cylindrical Farmer type ionization chamber.***

Cylindrical chambers are produced by various manufacturers, with active volumes between 0.1 and 1 cm^3. They typically have an internal length no greater than 25 mm and an internal diameter no greater than 7 mm. The wall material is of low atomic number Z (i.e. tissue or air equivalent), with the thickness less than 0.1 g/cm^2. A chamber is equipped with a buildup cap with a thickness of about 0.5 g/cm^2 for calibration free in air using ^{60}Co radiation. The chamber construction should be as homogeneous as possible, although an aluminium central electrode of about 1 mm in diameter is typically used to ensure flat energy dependence. Construction details of various commercially available cylindrical chambers are given in the IAEA Technical Reports Series (TRS) 277 and TRS 398 codes of practice [4-7].

4.3.3. Parallel-plate (Roos) ionization chambers

A parallel-plate ionization chamber consists of two plane walls, one serving as an entry window and polarizing electrode and the other as the back wall and collecting electrode, as well as a guard ring system. The back wall is usually a block of conducting plastic or a non-conducting material (usually Perspex or polystyrene) with a thin conducting layer of graphite forming the collecting electrode and the guard ring system on top. A schematic diagram of a parallel-plate ionization chamber is shown in Fig. 4.4.

The parallel-plate chamber is recommended for dosimetry of electron beams with energies below 10 MeV. It is also used for surface dose and depth dose measurements in the buildup region of megavoltage photon beams. The characteristics of commercially available parallel-plate chambers and the use of these chambers in electron beam dosimetry are explained in detail in the TRS 381 [6] and TRS 398 [7] codes of practice. Some parallel-plate chambers require significant fluence perturbation correction because they are provided with an inadequate guard width.

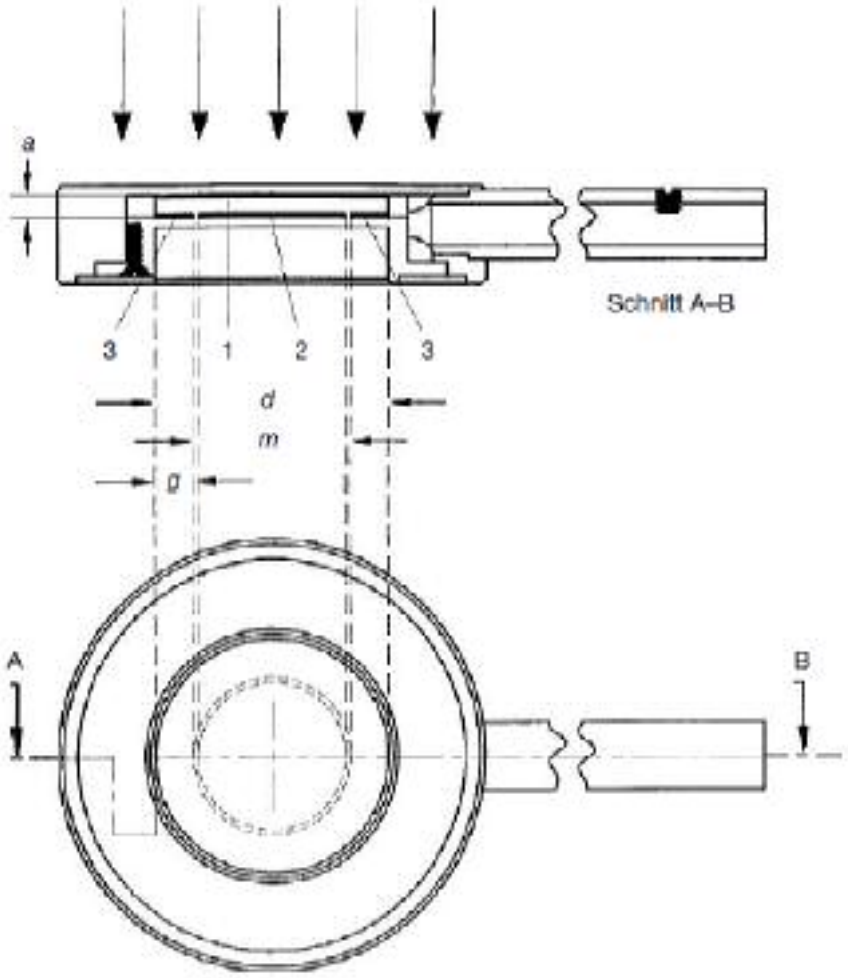

FIG. 4.4. ***Parallel-plate ionization chamber. 1: the polarizing electrode. 2: the measuring electrode. 3: the guard ring. a: the height (electrode separation) of the air cavity. d: the diameter of the polarizing electrode. m: the diameter of the collecting electrode. g: the width of the guard ring.***

4.3.4. Brachytherapy chambers

Sources used in brachytherapy are low air kerma rate sources that require chambers of sufficient volume (about 250 cm^3 or more) for adequate sensitivity. Well type chambers or re-entrant chambers are ideally suited for calibration and standardization of brachytherapy sources [8]. Fig. 4.5 shows a schematic diagram of a well type chamber. Well type chambers should be designed to accommodate sources of the typical sizes and shapes that are in clinical use in brachytherapy and are usually calibrated in terms of the reference air kerma rate.

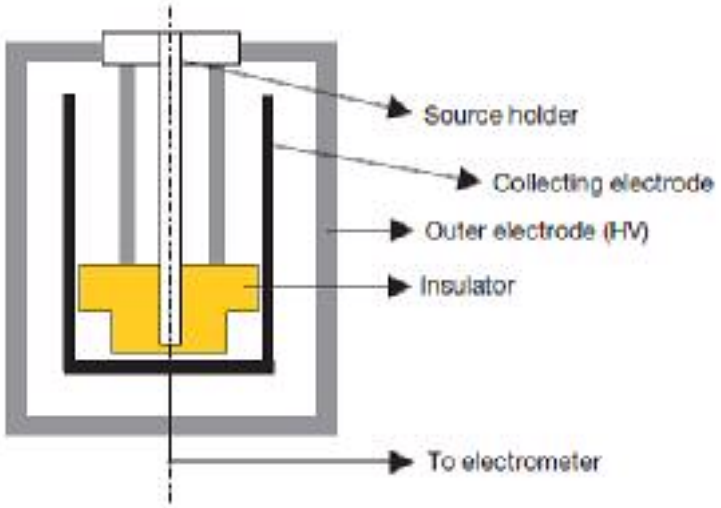

FIG. 4.5. ***Basic design of a brachytherapy well type chamber.***

4.3.5. Extrapolation chambers

Extrapolation chambers are parallel-plate chambers with a variable sensitive volume. They are used in the measurement of surface doses in orthovoltage and megavoltage X ray beams and in the dosimetry of β rays, and low energy X rays. They can also be used in absolute radiation dosimetry when directly embedded into a tissue equivalent phantom. The cavity perturbation for electrons can be eliminated by making measurements as a function of the cavity thickness and then extrapolating to zero thickness. Using this chamber, the cavity perturbation for parallel-plate chambers of finite thickness can be estimated.

4.4. FILM DOSIMETRY

4.4.1. Radiographic film

Radiographic X ray film performs several important functions in diagnostic radiology, radiotherapy and radiation protection. It can serve as a radiation detector, a relative dosimeter, a display device and an archival medium.

Unexposed X ray film consists of a base of thin plastic with a radiation sensitive emulsion (silver bromide (AgBr) grains suspended in gelatin) coated uniformly on one or both sides of the base [2].

- Ionization of AgBr grains, as a result of radiation interaction, forms a latent image in the film. This image only becomes visible (film blackening) and permanent subsequently to processing.
- Light transmission is a function of the film opacity and can be measured in terms of optical density (OD) with devices called densitometers.
- The OD is defined as $OD = \log_{10} (I_0/I)$ and is a function of dose. I_0 is the initial light intensity and I is the intensity transmitted through the film.
- Film gives excellent 2-D spatial resolution and, in a single exposure, provides information about the spatial distribution of radiation in the area of interest or the attenuation of radiation by intervening objects.
- The useful dose range of film is limited and the energy dependence is pronounced for lower energy photons. The response of the film depends on several parameters, which are difficult to control. Consistent processing of the film is a particular challenge in this regard.
- Typically, film is used for qualitative dosimetry, but with proper calibration, careful use and analysis film can also be used for dose evaluation.
- Various types of film are available for radiotherapy work (e.g. direct exposure non-screen films for field size verification, phosphor screen films used with simulators and metallic screen films used in portal imaging).

● Unexposed film would exhibit a background OD called the fog density (OD_f). The density due to radiation exposure, called the net OD, can be obtained from the measured density by subtracting the fog density.

● OD readers include film densitometers, laser densitometers and automatic film scanners. The principle of operation of a simple film densitometer is shown in Fig. 4.6.

Ideally, the relationship between the dose and OD should be linear, but this is not always the case. Some emulsions are linear, some are linear over a limited dose range and others are non-linear. The dose versus OD curve, known as the sensitometric curve (also known as the characteristic or H&D curve, in honour of Hurter and Driffield, who first investigated the relationship) must therefore be established for each film before using it for dosimetry work.

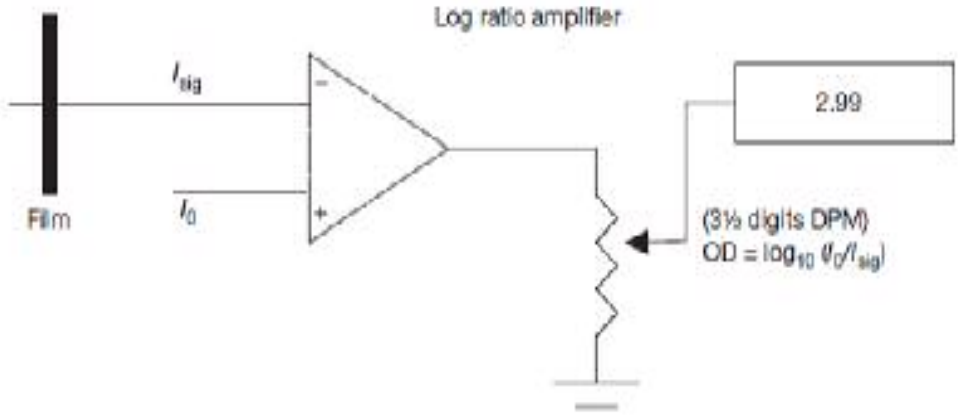

FIG. 4.6. ***Basic film densitometer***

A typical H&D curve for a radiographic film is shown in Fig. 4.7. It has four regions: (1) fog, at low or zero exposures; (2) toe; (3) a linear portion at intermediate exposures; and (4) shoulder and saturation at high exposures.

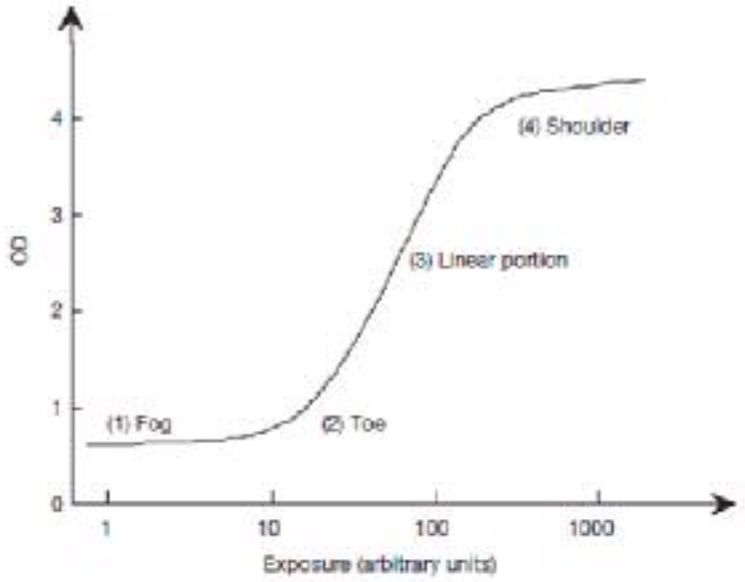

FIG. 4.7. ***Typical sensitometric (characteristic H&D) curve for a radiographic film.***

The linear portion is referred to as optimum measurement conditions, the toe is the region of underexposure and the shoulder is the region of overexposure.

Important parameters of film response to radiation are gamma, latitude and speed:

- The slope of the straight line portion of the H&D curve is called the gamma of the film.
- The exposure should be chosen to make all parts of the radiograph lie on the linear portion of the H&D curve, to ensure the same contrast for all ODs.
- The latitude is defined as the range of exposures over which the ODs will lie in the linear region.
- The speed of a film is determined by giving the exposure required to produce an OD of 1.0 greater than the OD of fog.

Typical applications of a radiographic film in radiotherapy are qualitative and quantitative measurements, including electron beam dosimetry, quality control of radiotherapy machines (e.g. congruence of light and radiation fields and the

determination of the position of a collimator axis, the so called star test), verification of treatment techniques in various phantoms and portal imaging.

4.4.2. Radiochromic film

Radiochromic film is a new type of film in radiotherapy dosimetry. The most commonly used is a GafChromic film. It is a colourless film with a nearly tissue equivalent composition (9.0% hydrogen, 60.6% carbon, 11.2% nitrogen and 19.2% oxygen) that develops a blue colour upon radiation exposure.

Radiochromic film contains a special dye that is polymerized upon exposure to radiation. The polymer absorbs light, and the transmission of light through the film can be measured with a suitable densitometer. Radiochromic film is self-developing, requiring neither developer nor fixer. Since radiochromic film is grainless, it has a very high resolution and can be used in high dose gradient regions for dosimetry (e.g. measurements of dose distributions in stereotactic fields and in the vicinity of brachytherapy sources). Dosimetry with radiochromic films has a few advantages over radiographic films, such as ease of use; elimination of the need for darkroom facilities, film cassettes or film processing; dose rate independence; better energy characteristics (except for low energy X rays of 25 kV or less); and insensitivity to ambient conditions (although excessive humidity should be avoided). Radiochromic films are generally less sensitive than radiographic films and are useful at higher doses, although the dose response non-linearity should be corrected for in the upper dose region.

- Radiochromic film is a relative dosimeter. If proper care is taken with calibration and the environmental conditions, a precision better than 3% is achievable.

- Data on the various characteristics of radiochromic films (e.g. sensitivity, linearity, uniformity, reproducibility and post-irradiation stability) are available in the literature.

4.5. SEMICONDUCTOR DOSIMETRY

4.5.1. Silicon diode dosimetry systems

A silicon diode dosimeter is a p–n junction diode. The diodes are produced by taking n type or p type silicon and counter-doping the surface to produce the opposite type material. These diodes are referred to as n–Si or p–Si dosimeters, depending upon the base material. Both types of diode are commercially available, but only the p–Si type is suitable for radiotherapy dosimetry, since it is less affected by radiation damage and has a much smaller dark current.

Radiation produces electron–hole (e–h) pairs in the body of the dosimeter, including the depletion layer. The charges (minority charge carriers) produced in the body of the dosimeter, within the diffusion length, diffuse into the depleted region. They are swept across the depletion region under the action of the electric field due to the intrinsic potential. In this way a current is generated in the reverse direction in the diode.

- Diodes are used in the short circuit mode, since this mode exhibits a linear relationship between the measured charge and dose. They are usually operated without an external bias to reduce leakage current.
- Diodes are more sensitive and smaller in size than typical ionization chambers. They are relative dosimeters and should not be used for beam calibration, since their sensitivity changes with repeated use due to radiation damage.
- Diodes are particularly useful for measurement in phantoms, for example of small fields used in stereotactic radiosurgery or high dose

gradient areas such as the penumbra region. They are also often used for measurements of depth doses in electron beams. For use with beam scanning devices in water phantoms, they are packaged in a waterproof encapsulation. When used in electron beam depth dose measurements, diodes measure directly the dose distribution (in contrast to the ionization measured by ionization chambers).

● Diodes are widely used in routine in vivo dosimetry on patients or for bladder or rectum dose measurements. Diodes for in vivo dosimetry are provided with buildup encapsulation and hence must be appropriately chosen, depending on the type and quality of the clinical beams. The encapsulation also protects the fragile diode from physical damage.

● Diodes need to be calibrated when they are used for in vivo dosimetry, and several correction factors have to be applied for dose calculation. The sensitivity of diodes depends on their radiation history, and hence the calibration has to be repeated periodically.

● Diodes show a variation in dose response with temperature (this is particularly important for long radiotherapy treatments), dependence of signal on the dose rate (care should be taken for different source to skin distances), angular (directional) dependence and energy dependence even for small variations in the spectral composition of radiation beams.

4.5.2. MOSFET dosimetry systems

A metal-oxide semiconductor field effect transistor (MOSFET), a miniature silicon transistor, possesses excellent spatial resolution and offers very little attenuation of the

beam due to its small size, which is particularly useful for *in vivo* dosimetry [8-10]. MOSFET dosimeters are based on the measurement of the threshold voltage, which is a linear function of absorbed dose. Ionizing radiation penetrating the oxide generates charge that is permanently trapped, thus causing a change in threshold voltage. The integrated dose may be measured during or after irradiation. MOSFETs require a connection to a bias voltage during irradiation. They have a limited lifespan.

- A single MOSFET dosimeter can cover the full energy range of photons and electrons, although the energy response should be examined, since it varies with radiation quality. For megavoltage beams, however, MOSFETs do not require energy correction, and a single calibration factor can be used.
- MOSFETs exhibit small axial anisotropy (±2% for 360º) and do not require dose rate corrections.
- Similarly to diodes, single MOSFETs exhibit a temperature dependence, but this effect has been overcome by specially designed double detector MOSFET systems. In general, they show non-linearity of response with the total absorbed dose; however, during their specified lifespan, MOSFETs retain adequate linearity. MOSFETs are also sensitive to changes in the bias voltage during irradiation (it must be stable), and their response drifts slightly after the irradiation (the reading must be taken in a specified time after exposure).
- MOSFETs have been in use for the past few years in a variety of radiotherapy applications for *in vivo* and phantom dose measurements, including routine patient dose verification, brachytherapy, TBI, intensity modulated radiotherapy (IMRT), intraoperative radiotherapy

and radiosurgery. They are used with or without additional buildup, depending on the application.

4.6. OTHER DOSIMETRY SYSTEMS

4.6.1. Alanine/electron paramagnetic resonance dosimetry system

Alanine, one of the aminoacids, pressed in the form of rods or pellets with an inert binding material, is typically used for high dose dosimetry [11]. The dosimeter can be used at a level of about 10 Gy or more with sufficient precision for radiotherapy dosimetry. The radiation interaction results in the formation of alanine radicals, the concentration of which can be measured using an electron paramagnetic resonance (known also as electron spin resonance) spectrometer. The intensity is measured as the peak to peak height of the central line in the spectrum. The readout is non-destructive.

- Alanine is tissue equivalent and requires no energy correction within the quality range of typical therapeutic beams. It exhibits very little fading for many months after irradiation. The response depends on environmental conditions during irradiation (temperature) and storage (humidity).
- At present, alanine's potential application for radiotherapy is in dosimetry comparisons among hospitals.

Bibliography

[1] Attix, F.H., *Introduction to Radiological Physics and Radiation Dosimetry*, Wiley, New York (1986).

[2] Cameron, J.R., Suntharalingham, N., Kenney, G.K., *Thermoluminescent Dosimetry,* University of Wisconsin Press, Madison, WI (1968).

[3] Horton, J., *Handbook of Radiation Therapy Physics*, Prentice Hall, New York (1987).

[4] INTERNATIONAL ATOMIC ENERGY AGENCY, Absorbed Dose Determination in Photon and Electron Beams, Technical Reports Series No. 277, IAEA, Vienna (1987).

[5] Calibration of Dosimeters Used in Radiotherapy, Technical Reports Series No. 374, IAEA, Vienna (1994).

[6] The Use of Plane Parallel Ionization Chambers in High Energy Electron and Photon Beams, Technical Reports Series No. 381, IAEA, Vienna (1997).

[7] Absorbed Dose Determination in External Beam Radiotherapy, Technical Reports Series No. 398, IAEA, Vienna (2000).

[8] INTERNATIONAL ORGANIZATION FOR STANDARDIZATION, Guide to Expression of Uncertainty in Measurement, ISO, Geneva (1992).

[9] Khan, F.M., *The Physics of Radiation Therapy*, Lippincott, Williams and Wilkins, Baltimore, MD (2003).

[10] Klevenhagen, S.C., *Physics and Dosimetry of Therapy Electron Beams*, Medical Physics Publishing, Madison, WI (1993).

[11] Van Dyk, J. (Ed.), *Modern Technology of Radiation Oncology: A Compendium for Medical Physicists and Radiation Oncologists*, Medical Physics Publishing, Madison, WI (1999).

Chapter 5

SYNTHETIC SINGLE CRYSTAL DIAMOND

FOR RADIOTHERAPIC DOSIMETRY

5.1 INTRODUCTION

The commonly used detectors for photon and electron beam measurements in the energy range of MeV, the ionization chamber and the silicon diode, have a limited range of applicability which is dictated by their design and the intrinsic properties of their respective detector elements.

The ionization chamber is able to very accurately measure dose distributions for regions where the dose is not varying rapidly. The relatively large sensitive volume of most chambers means, however, that a significant spatial averaging, or smoothing of the true dose distribution occurs. Ionization chambers are therefore not suitable when high spatial resolution is required, such as in the accurate measurement of penumbra widths [1] except in the case of very small sensitive volumes devices. In this case, the use of very small ionization chambers is often precluded by the low density, and hence low sensitivity, of their air volume.

Silicon diode detectors have the advantage of a small, high-density, sensitive volume and thus have a high spatial resolution. A significant disadvantage however is the non-water-equivalence of the silicon. As Fig. 1 shows, the silicon-to-water collision mass stopping power ratio is not constant with electron energy, especially at energies below 5 MeV. In addition, separate diode detectors are required for electron and photon dosimetry.

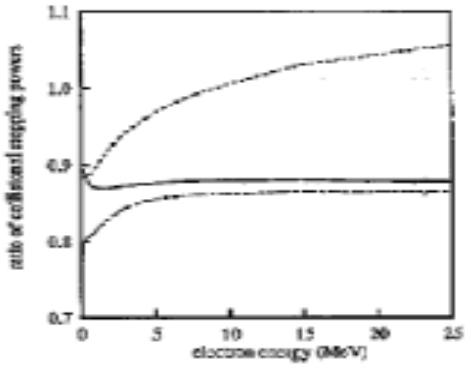

Fig 5.1. Collision stopping power ratios of carbon-to-water (solid line), air-to-water (dotted line) and silicon-to-water as (dash-dotted line) as function of photon energy.

Diamond detectors are attractive because of their near water-equivalence and their radiation hardness [2]. As Fig.1 shows, the carbon-to-water stopping power ratio remains approximately constant over the energy range 1-20 MeV, which implies an advantage of diamond detectors over silicon diodes for electron dosimetry. Fig. 1 also shows the increase in the air-to-water stopping power ratio with energy caused by the density effect. As a matter of fact, type IIa natural diamonds are well assessed in the market since a relatively long time for such application in dosimetry [3]. However, they were found to suffer from some relevant limitations. An undesired dose rate dependence of the response of such devices makes it necessary to correct the acquired data by sample-dependent correction factors [3]. In addition, natural diamond exhibiting detector grade quality are extremely rare, so that they are very expensive and deliverable after very long times. On the other hand, polycrystalline diamonds usually deposited by chemical vapour deposition (CVD) as well as high-pressure high temperature (HPHT) single crystal diamonds (SCDs) are far from being of the same quality of the best type IIa natural ones to this respect [4]. Their electronic properties are often dominated by the presence of structural and crystallographic defects, which strongly affect the stability and reproducibility of the obtained dosimeters.

This is why a great effort is now being devoted to the achievement of high-quality single crystal synthetic diamonds, trying to overcome the main factors limiting a widespread diffusion of diamond-based dosimeters [5,6].

In this context is inserted the following discussion in which we report on the realization and characterization of CVD a SCD dosimeter, fabricated at University of Rome ‘‘Tor Vergata’’ Laboratories of Mechanical Engineering Department, and tested at the S. Filippo Neri Hospital in Rome.

5.2 SCD DOSIMETER FABRICATION

The standard configuration in which "detector-grade" type II a diamond crystals are assembled in the dosimeter realization is the classical "sandwich configuration" in which the sensing element (diamond) is contacted on opposite sides by two metal electrodes (Au, Al or other metals) evaporated on the upper and lower surface (Fig.2).

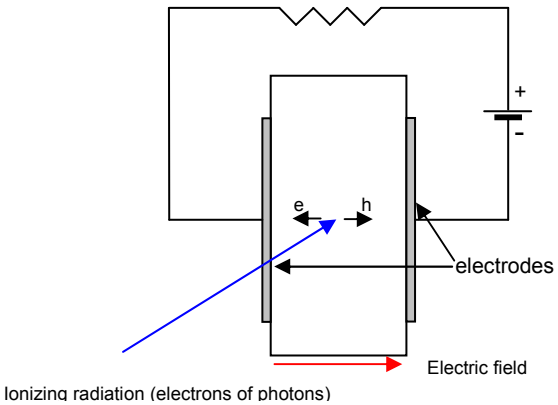

Fig. 5.2. sketch of a typical natural diamond dosimeter

Typically natural diamond crystals of some hundred microns thickness and some mm^2 surface are used in this configuration. The possibility of growing high electronic quality films of intrinsic and p-doped diamond offered by the CVD technique enabled us to use an alternative configuration in which the SCD dosimeter is fabricated in p-type/intrinsic/metal layered structure, whose schematic is shown in Fig. 5.3.

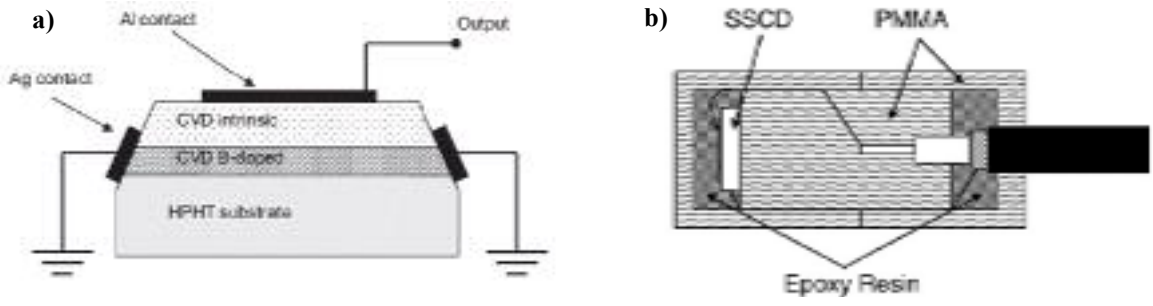

Fig. 5.3 a) Schematics of the CVD single crystal diamond diode. b) the waterproof PMMA and epoxy resin housing

First, a 4x4 mm^2 commercial HPHT single crystal substrate is covered by a highly conductive boron-doped CVD diamond film, which is used as a backing contact. An intrinsic diamond sensing layer is then grown on the doped surface, on top of which an aluminium contact is thermally evaporated. The resulting sensitive volume is approximately some tenth of mm^3, depending on the thickness of the intrinsic layer (tipically some micron) and the area of the metallic contact (typically some mm^2). The dosimeter fabrication process is then concluded by embedding the dosimeter in a waterproof housing made of PMMA (polymetylmetacrilate) and epoxy resin (Fig.5.3b). The choice of PMMA and epoxy resin as encapsulants and waterproofing materials is dictated primarily by their tissue-equivalence, namely the property of possessing a coefficient of mass attenuation and absorption [Chap.3.6] similar to that of water (which comprises 70% of human body).

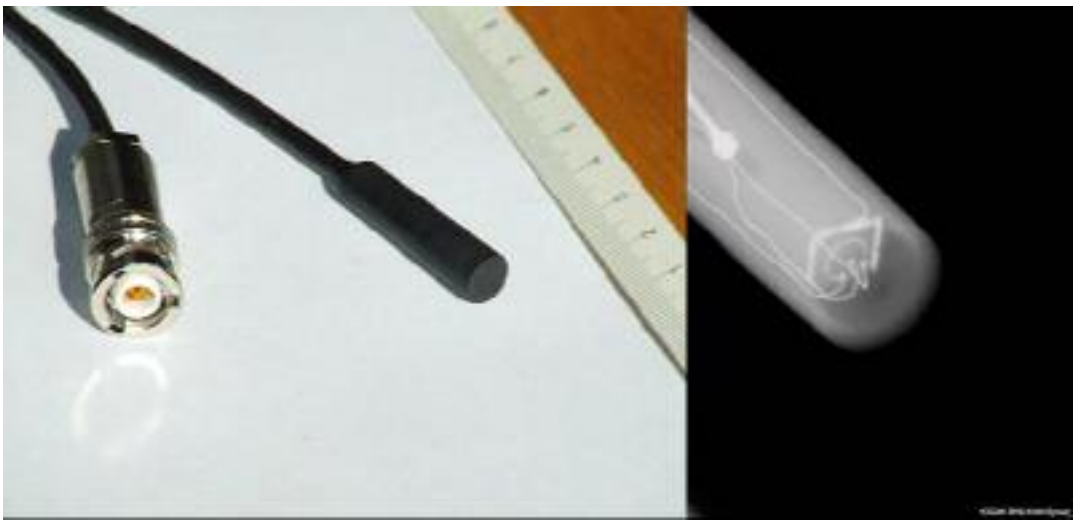

Fig. 5.4.a) Image of the CVD dosimeter with the connection cable and the PMMA housing painted with graphite-based lacquer. b) X-ray image of the CVD dosimeter. It is possible to identify the squared diamond element, the signal cables, and the circular aluminium dot on the top of the intrinsic diamond layer.

The PMMA housing is finally painted with graphite-based lacquer, in order to make conductive the external envelope using a tissue-equivalent coating (Fig.5.4a).

5.3 DOSIMETRIC CHARACTERIZATION

5.3.1 Preliminary test

A preliminary characterization of the device properties was done exposing it to the outgoing X-ray beam from a standard electron gun with copper target for *X Ray Diffraction.*

In this case the spectrum of the outgoing radiation consists of a *continuum* of X-rays, with additional sharp peaks at certain energies. The continuous spectrum is due to electron's *bremsstrahlung radiation*, while the sharp peaks are characteristic X-rays associated with the atoms in the target (in the case of copper the $k_{\alpha 1}$ and $k_{\alpha 2}$ emission at 8.048 and 8.028 keV and the $k_{\beta 1}$ and $k_{\beta 2}$ emission at 8.905 and 8.977 keV respectively).

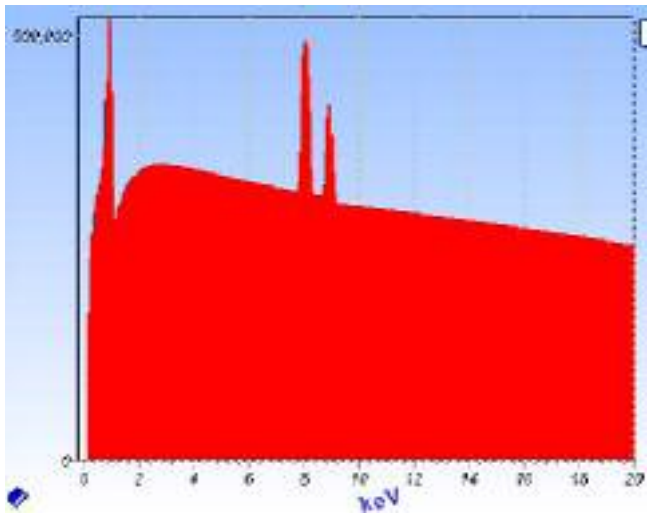

Fig.5.5 Typical emission spectrum of a XRD electron gun with copper target. On x-axis the energy, on y-axis an arbitrary units proportional to the emission intensity (logarithmic scale). Superimposed to the bremsstrahlung radiation it is possible to observe some emission peaks caracteristic of the target material ($k_{\alpha 1}$ and $k_{\alpha 2}$ emission at about 8 keV and $k_{\beta 1}$ and $k_{\beta 2}$ emission at about 9 keV).

This preliminary test was performed using a particular scheme of irradiation thought to put out the properties of signal stability, response speed and dose linearity. Initially, the dosimeter is exposed for 600 seconds at a constant dose to highlight the signal stability properties. A variation of the initial signal (that tends to become constant whithin times of 300-500 seconds) is normally observed. This trend is also found in commercial

dosimeters (a pre-irradiation procedure to stabilize the response is normally recommended) and in the case of diamond is believed to be due to levels saturation in the energy gap [6]. Subsequently, the X-ray beam is interrupted for successive intervals of 15, 30 and 60 seconds, in order to highlight the response speed to sudden changes in the dose rate.

Finally, the electron gun filament current is changed in order to vary the X-ray beam intensity and, consequently, the X-ray dose rate incident on the dosimeter. This check is intended to verify the linearity of response as a function of dose rate.

In the next graph the whole irradiation procedure, in terms of current signal vs time is shown:

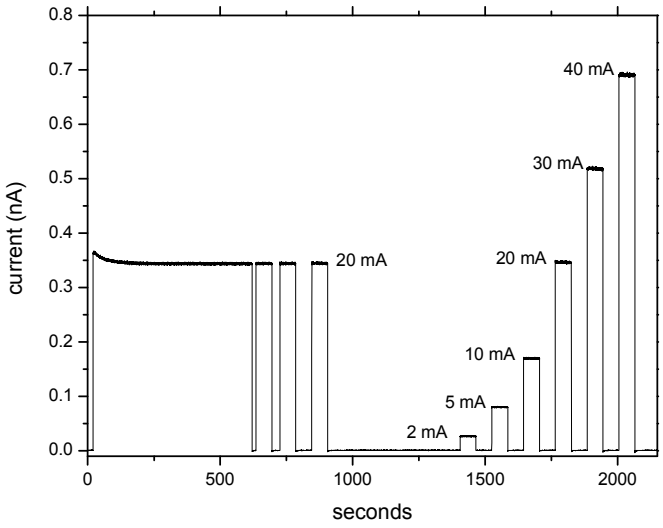

Fig.5.6 Irradiation procedure adopted for preliminary test: the SCD dosimeter is firstly exposed to a costant X-ray dose (corresponding to a filament currento of 20mA) for 600 s, after which the flux is suddenly switched off for three different intervals (15s, 30s and 60s respectively) in order to test the respone speed. Finally, the filament current is varied from 2 mA up to 40 mA in successive steps of 30s duration, each with intervals of 30s without irradiation, in order to test the dosimeter linearity with dose rate.

5.3.2 Test at San Filippo Neri Hospital

Irradiation experiments with radiotherapic radiation were performed at San Filippo Neri Hospital, by using Bremsstrahlung X-ray beams with maximum energy of 6 and 10 MeV, produced by a CLINAC DHX Varian accelerator as well as electron beams with

different energies, ranging from 6 to 18 MeV. All measurements were done in a motorized water phantom (PTW MP3), according to the International Atomic Energy Agency (IAEA) dosimetry protocol [7]. The distance between the beam source and the water surface was fixed at 90 cm (Source-to-Surface Distance SSD).

Fig. 5.7. The CLINAX DHX Accelerator with the PTW motorized water phantom MP3 (red arrow)

A PTW Semiflex commercial Roos ionization chamber [8] (IC in the following) was used together with the diamond detector for calibration and comparison. This kind of ionization chamber is used as a reference electron chamber as recommended by the IAEA dosimetric protocol [7] for high precision electron dosimetry in radiation therapy. The chamber has a 4 mm wide guard ring to exclude any perturbation effect even at low electron energies. The energy response is only influenced by the stopping power ratios water/air. The chamber is waterproof for absolute dose and depth dose measurements in a water phantom and its nominal useful energy range is from 2 MeV to 45 MeV.

During the test the SCD dosimeter was connected both to a Keithley 6517A electrometer through a 15-m long triaxial cable and to a commercial PTW TANDEM acquisition system. Both dosimeters operated in current mode, like in the case of the preliminary tests, and in integrated charge, measuring the total current obtained under irradiation. The first measurement configuration is more indicative of the *istantaneous released dose* while the second is used when a direct indication of the *total released dose* is needed.

No external bias voltage was applied to the CVD dosimeter during the test. Its response was thus only driven by the built-in potential arising from the adopted p-type/intrinsic/metal layered structure. Such a built-in potential is created across the whole device and it is believed to be due to the combination of both the p-type/intrinsic diamond and the intrinsic diamond/aluminium junctions [9].

In order to highlight this point in Fig. 5.8 the I–V curve of the diamond-based device is reported as measured in dark (full dots) and under irradiation with 10-MV photons at 3Gy/min dose rate (open dots). A signal is observed at 0-V bias, demonstrating the existence of a built-in potential and the possibility of operation with no external voltage applied.

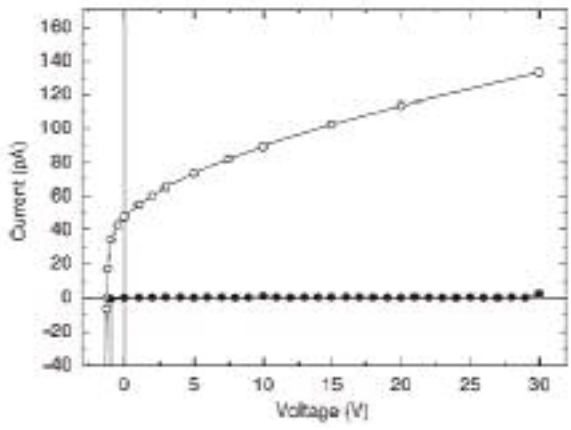

Fig. 5.8. I–V curve of the device in dark (full dots) and under 3Gy/min 10 MV photons irradiation (open circles).

As mentioned during the preliminary test, a pre-irradiation procedure was found to be necessary before daily use in order to stabilize the device response. During this

preirradiation, the response is observed to typically decrease to a regime value 20% lower than the starting one. Approximately 10–15 Gy irradiation is needed in order to reach a device output stability of 0.5% FWHM. This procedure was also applied to the IC [7].

An evaluation of the signal obtained from the investigated devices was performed by measuring the photocurrent during irradiation at a depth of 2.4 cm in water, where the maximum absorbed dose is expected for a 10 MV beam (§ 3.7.3).

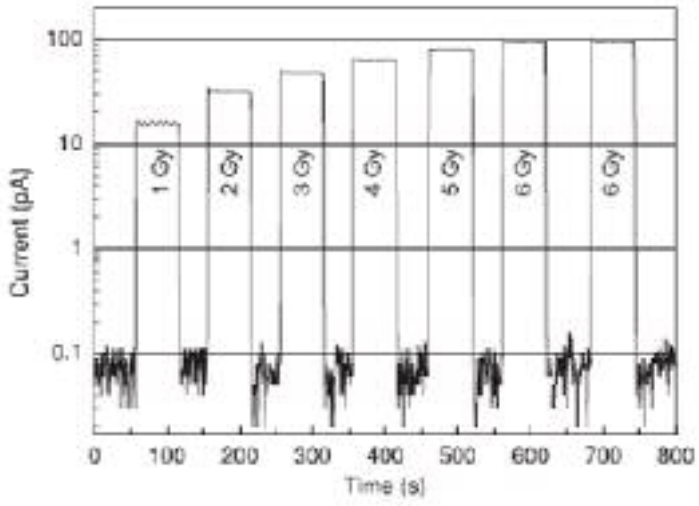

Fig. 5.9. Device current vs time during a multi-step irradiation.

In Fig. 3, the detector current is reported in a semi-log plot, as measured during a multi-step irradiation process. Different doses, from 1 to 6 Gy, were delivered with accordingly increasing dose rates in order to have the same duration time of each step. A fast device response time can be noticed as well as the complete absence of persistent photocurrents.

The linearity of the device response as a function of the delivered dose was measured with 10-MV photons with the detector kept at the same depth in water as before. The results, reported in Fig.5.10, were obtained irradiating the samples at a fixed dose rate of 3 Gy/min to deliver doses ranging from 0.04 to 50 Gy, thus changing the exposure time between 0.8 and 1000 s. An excellent linear behaviour is observed, with a linearity index $\Delta = 1.0008$ as derived by the best fit to the experimental data with the function $y = a*x^{\Delta}$.

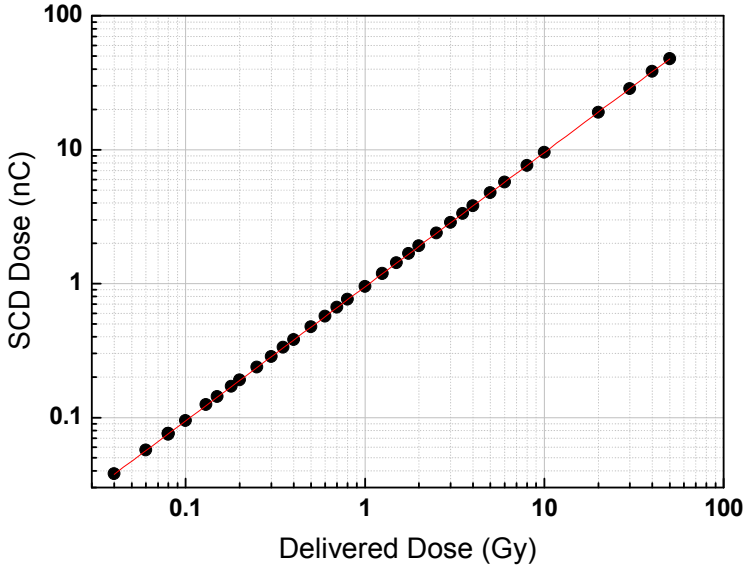

Fig. 5.10 Measured integrated charge as a function of the nominal delivered dose, which was changed by varying the exposure time and keeping constant the dose rate.

The analysis of residuals from the linear best fit is reported in Fig.5.11, demonstrating a deviation from linearity of less than 0.5% with the exception of few very low dose data affected by scattering due to noise and/or accelerator instabilities.

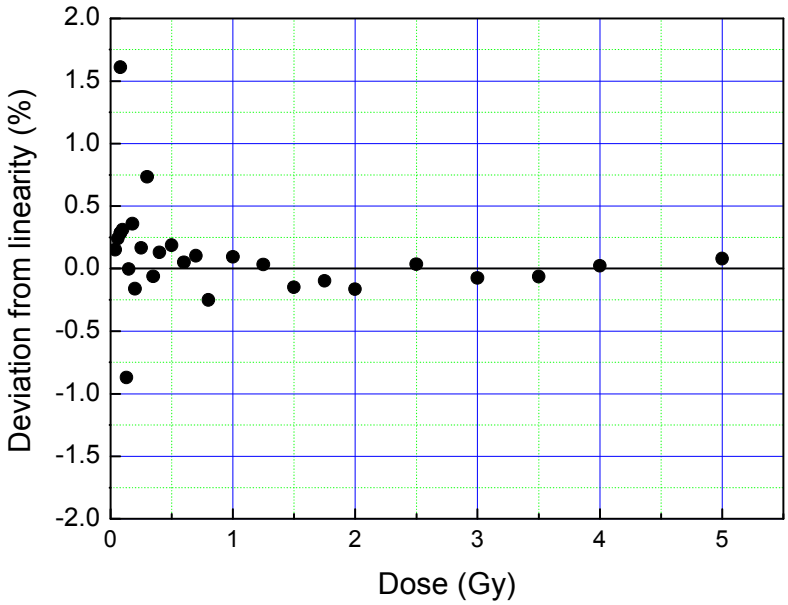

Fig. 5.11 Percentage deviation from the linear best fit of experimental data reported in Fig. 4.

The detector photocurrent as a function of the dose rate was studied adopting two different procedures: (i) varying the pulse repetition frequency of the accelerator and keeping constant the exposure time and (ii) varying the distance between the source and the water surface. For these linearity measurements neither the photon energy (10 MV) nor the depth in water (2.4 cm) were changed.

The results for procedure (i) are reported in Fig. 5.12(a) for all the pulse repetition rates available from the accelerator. A very good linear behaviour is observed with a linearity index $\Delta = 0.9997$.

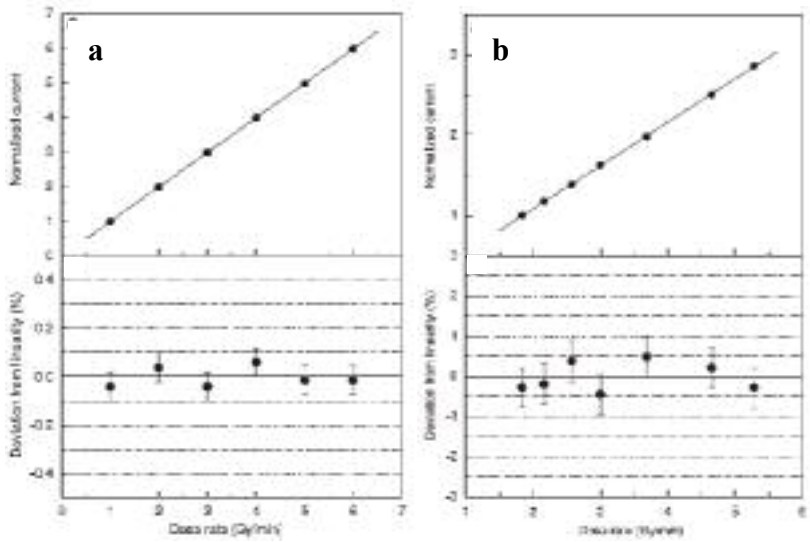

Fig. 5.12 Normalized device current as a function of the dose rate, which was changed by varying the pulse repetition frequency of the accelerator (a) and the source-to-water distance (b). Deviation from linearity are represented in the lower graphs.

Fig. 5.12(b) summarizes the results obatined adopting the procedure (ii). A very good linearity is observed again, with a linearity index $\Delta = 0.996$ and a deviation from linearity below ± 0.5%.

The dependence of the detector response on the radiation quality was then studied for each radiation type provided by the accelerator (i.e. 6 and 10 MV photons and 6, 9, 12, 15 and 18 MeV electrons) measuring its sensitivity in term of the current signal per Gy released. For each kind of irradiation the detector was placed in the corresponding

maximum dose position. The results are summarized in Fig.5.13, where the obtained sensitivities are reported. It is possible to observe that a constant sensitivity value is observed for each radiation quality with the exception of 6-MV photons in which case a slightly lower response, of the order of 1% below, is observed.

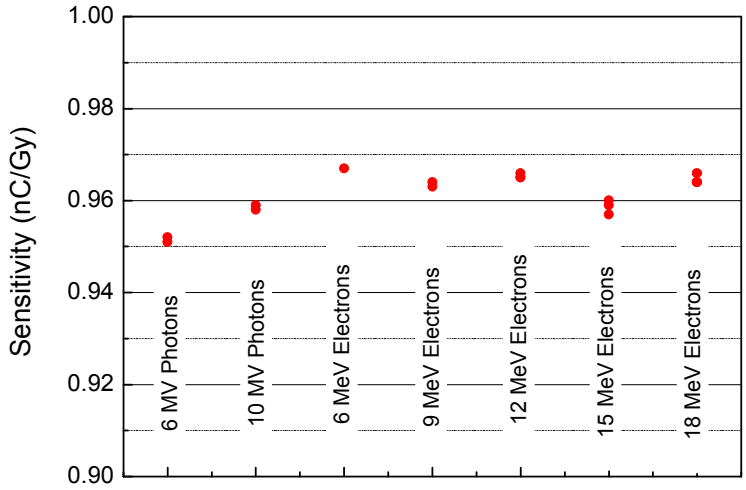

Fig. 5.13 SCD sensitivity for all the available radiation qualities from the Varian Clinac DHX accelerator (two repetitons).

The Percentage Depth Dose (PDD) curves are very important to have an indication of the dose given at different depths in the body and are obtained by measuring the current signal as a function of depth in the water phantom. This test is therefore comparable to mark the build-up curve discussed in § 3.7.3.

In our case the PDD measurements were performed connecting the dosimeter to the PTW TANDEM acquisition system. The reference IC was placed in air at the same distance from the source within the irradiation field, in order to properly take in account the accelerator fluctuations and reduce the scattering of experimental data. In this configuration it should be pointed out that the IC current signal *cannot be directly compared* with the one of the diamond detector because *it must be converted by the*

stopping power ratios water/air, according with Fig.5.1 and considering that *the IC sensitive material is air*.

An automated acquisition cycle was adopted, with 1 s measuring time in each position, which was sequentially repeated in both directions, i.e. from top to bottom position of the water phantom and vice-versa. In Fig. 5.14(a) and (b) the 10 and 6 MV photons results are reported. A good agreement with the reference IC is observed in both cases. Small deviation can be noticed at high depths where the diamond signal was observed to be higher than the one from the IC. In particular, at 30 cm deep in water, the diamond signal is 2.4% and 4.9% higher than the IC one for 10 MV and 6 MV photons, respectively. It can be also noticed that the two sets of data acquired by the diamond dosimeter (from bottom to top and vice versa) are perfectly superimposed, being almost indistinguishable .

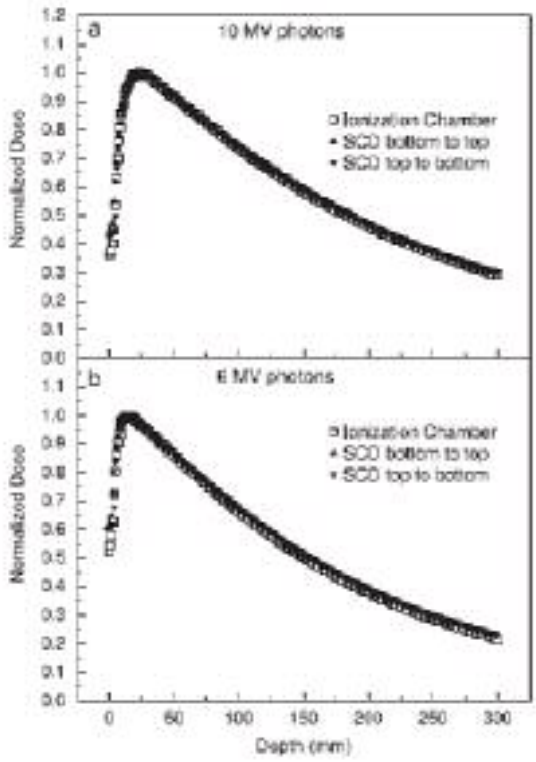

Fig. 5.14 Percentage depth dose profiles in water as measured by the SCD dosimeters (triangles) and by the ionization chamber (open squares) under irradiation with (a) 10-MV photons and (b) 6-MV photons.

The PDD curves in water were also measured for electrons in the energy range from 6 to 18 MeV. The results are summarized in Fig.5.15 and compared with the reference curves from the IC. An excellent agreement between the two sets of data is observed.

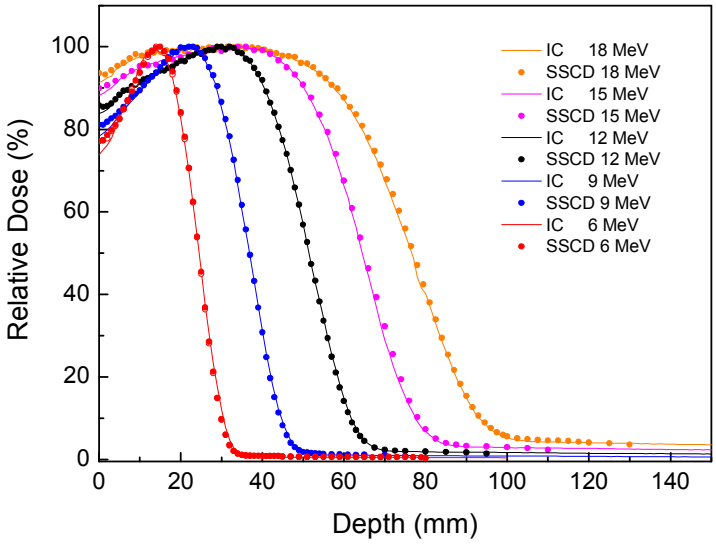

Fig.5.15 Percentage depth dose profiles in water under irradiation with 6, 9, 12, 15 and 18 MeV electrons as measured by the diamond dosimeter (symbols) and by the ionization chamber (lines).

To put in evidence the ability to spatially resolve the field of radiation, the transversal dose profile for a squared 10x10 cm^2 field was measured, putting the dosimeter at a depth of 2.4 cm of water under irradiation with 10 MV photons. The detector was moved across the whole irradiation field axes through an automated multi-step movement cycle. The comparison between the diamond detector and IC results is reported in Fig.5.16.

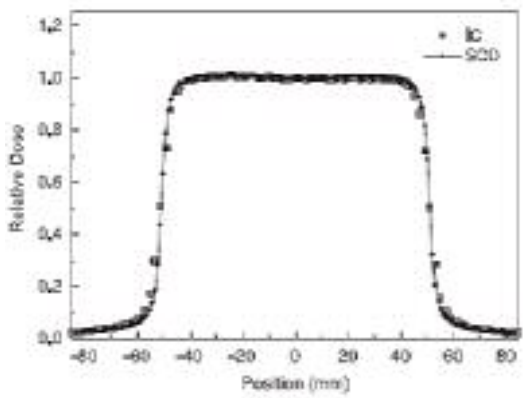

Fig. 5.16. Transversal dose profile acquired at depth of 2.5cm in water of a square 10x10 cm2 10 MV photon irradiation field as measured by the diamond diode (line+dots) and by the IC (squares).

Very similar trends are observed in both cases but a sharper edge of the irradiation field is measured by the diamond device, demonstrating a better spatial resolution of the CVD dosimeter. This result is quite expected, considering the different dimensions of the sensitive volume of the two dosimeters (0.35 cm^3 for the PTW Roos chamber, about 0.1 mm^3 for the diamond detetctor).

To this respect, it is should be pointed out that the PTW Roos chamber is *not* specifically designed for this type of measure, but this result is of great interest in the case of the CVD dosimeter, especially for application in highly conformed irradiation techniques such as Intensity Modulated Radiation Therapy [3] where a very high spatial resolution is requested.

5.4 APPLICATION IN A REAL INTENSITY MODULATED RADIATION TREATMENT (IMRT) PLAN

IMRT is a special technique which allows to change the irradiation intensity within the beam to create highly conformal dose distributions and reduce unwanted irradiation of surrounding normal tissue. These non-uniform beam intensities are generated by linear accelerators, equipped with multileaf collimators (MLCs), by superposing several sub-fields (segments) through a complex motion of the leaves either in sequential static delivery mode (SMLC-IMRT) or in continuously dynamic delivery mode (DMLC-IMRT) [3]. The number, shape and intensity of such irradiation segments are determined by the treatment planning system (TPS), using a mathematical optimization process, according to dose profiles and constraints set by the user. An “optimal” fluence map is usually achieved dividing each IMRT field into multiple small beams, whose dimensions are often smaller than the lateral range of secondary electrons produced. As a consequence, a detector characterized by a relatively large sensitive volume may cause fluence perturbations and dose averaging effects in peaked dose distributions, resulting

in an incorrect dose determination. A decrease in size of the sensitive volume yields a reduction of dose averaging effects and therefore leads to more accurate measurements in high dose gradient regions. As specified before, the decrease in detection volume, however, is in a trade-off with sensitivity, so that high sensitivity per unit volume materials are needed in order to keep statistical noise, reproducibility and accuracy acceptable. Ideally, IMRT detectors should exhibit other remarkable characteristics, like stability, fast response time, linearity, independence of the measured dose on the radiation quality and dose rate, tissue equivalence, radiation hardness, high sensitivity and low bias voltage operating conditions.

Our SCD dosimeter has shown to meet most of such stringent requirements. It should be pointed out that natural diamond-based dosimeters have been extensively tested [4,5] and have shown to be suitable for IMRT applications [6,7] but this is not the case for synthetic polycrystalline diamonds [4] mainly due to their slow dynamic response that makes them unable to reveal the sharp transients of IMRT fields. In the following, our Synthetic Single Crystal Diamond (SSCD in the following) dosimeter was employed in a real IMRT treatment plan operating at 0 V bias voltage.

5.5 EXPERIMENTAL DETAILS

In this test, the SSCD dosimeter was compared with two commercial ionization chambers. The first one was a PinPoint chamber (PP-IC in the following) PTW type 31014 (PTW-Freiburg, Germany) [8], with an inner diameter of 2 mm and a length of 5 mm for a total sensitive volume of about 15 mm^3 and a nominal sensitivity of 400pC/Gy. This ionization chamber can be used for both depth dose and absolute dose measurements. Due to its small sensitive volume, the main application is dosimetry in high energy beams with high spatial resolution, such as IMRT. The second ionization chamber was a Semiflex Chamber (SF-IC in the following) PTW type 31010 [8], with a

sensitive volume of about 386 mm^3 and a nominal sensitivity of 3.3nC/Gy. This chamber is cylindrically shaped with an inner diameter of 5.5 mm and 16.25 mm length. Due to its large useful energy range (30 KV-50 MV photons and 10-45 MeV electrons) SF-IC is mainly designed for dosimetry in conventional radiotherapy beams. For both IC's the sensitive volume is air vented and the wall material is PMMA and graphite. Power supply is 400 V, housing is waterproof.

Fig. 5.17 The two commercial Ionization Chambers used for testing the performances of the Single Crystal Diamon Dosimeter; PTW type 31014 Pin Point Chamber (on the left) and PTW type 31010 Semiflex Chamber (on the right).

To monitor the whole highly conformed dose profile a bidimensional diode array MapCheck (MC) model 1175 (Sun Nuclear Corporation, Florida) was used. The MC device consists of a 2D matrix of 445 radiation hardened silicon diodes, mounted between acrylic plates [10].

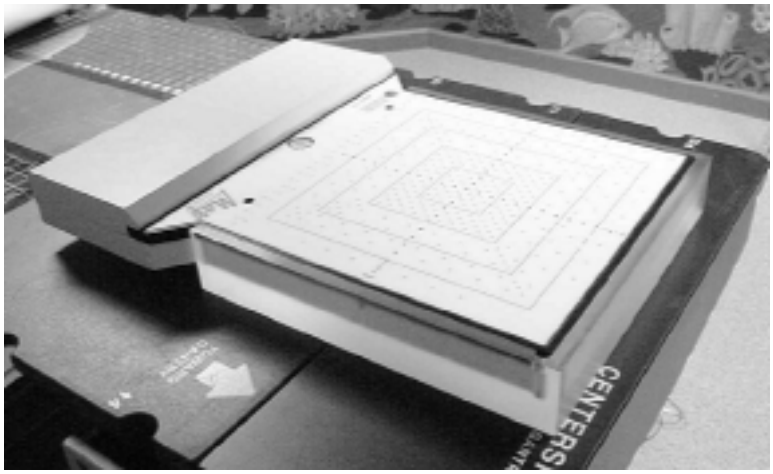

Fig. 5.18 The Sun Nuclear MapCheck. The whole squared surface represents the area to put under irradition during the treatment. In each of the visible dots is placed a silicon diode. The marked squares represents different irradiation fields.

Tests were performed delivering a prostate cancer IMRT treatment on a 20 cm^2 area, consisting of 10 complex shaped beams whose superposition results in an highly conformed dose profile [11] (one of the beams is reported in Fig.5.19a)). The whole dose map, as measured by the MC over the whole IMRT treatment, is reported in Fig.5.19b). Nine reference points, whose positions are indicated in Fig.5.19b), have been chosen in order to compare the dose measurements from all the devices adopted in the present work.

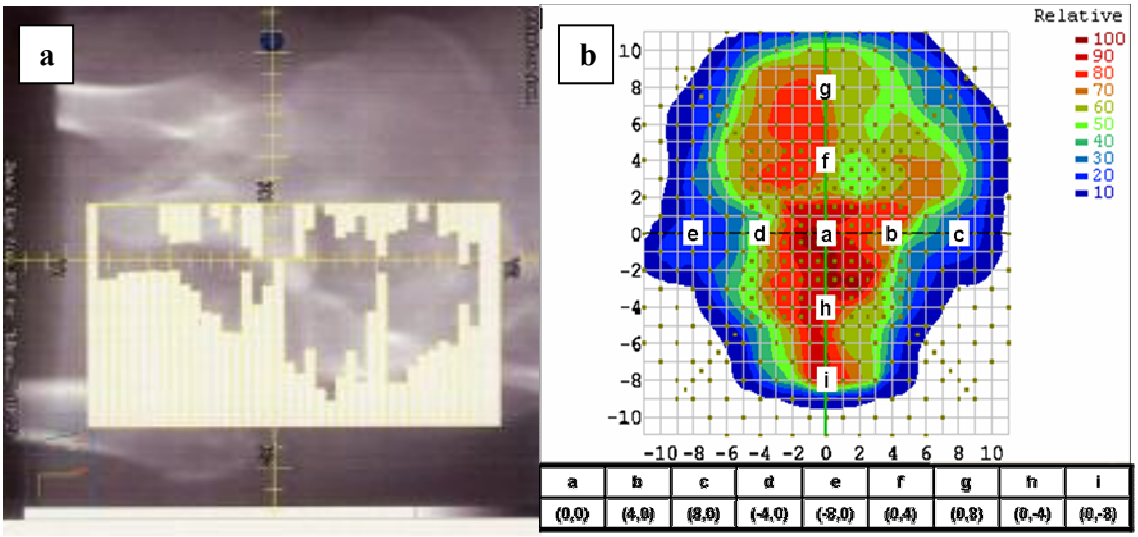

Fig.5.19a) Image of one of the complex shaped beam used; it can be saw the X-ray image of the abdomen area with the bones of the legs and pelvis. The yellow rectangle represents the entire area subjected to the treatment while the yellow segments indicate the sections screened in this particular beam. b) Dose map of the whole treatment as obtained by the MapCheck with the coordinates of the nine position examined with the three dosimeters.

All measurements were performed in the PTW motorized water phantom MP3 with SSD of 90 cm, while the dosimeters were positioned at a depth of 10 cm. Before the use, the usual pre-irradiation procedure was applied both to SSCD and IC.

5.6 RESULTS

Fig. 5.20 (up) shows the comparison between PP-IC, SF-IC and SSCD absolute current signal measured at the so-called *isocenter* (position ***a*** in Fig. 5.19b)) during the irradiation step of one of the 10 complex beams (B1), constituting the whole treatment.

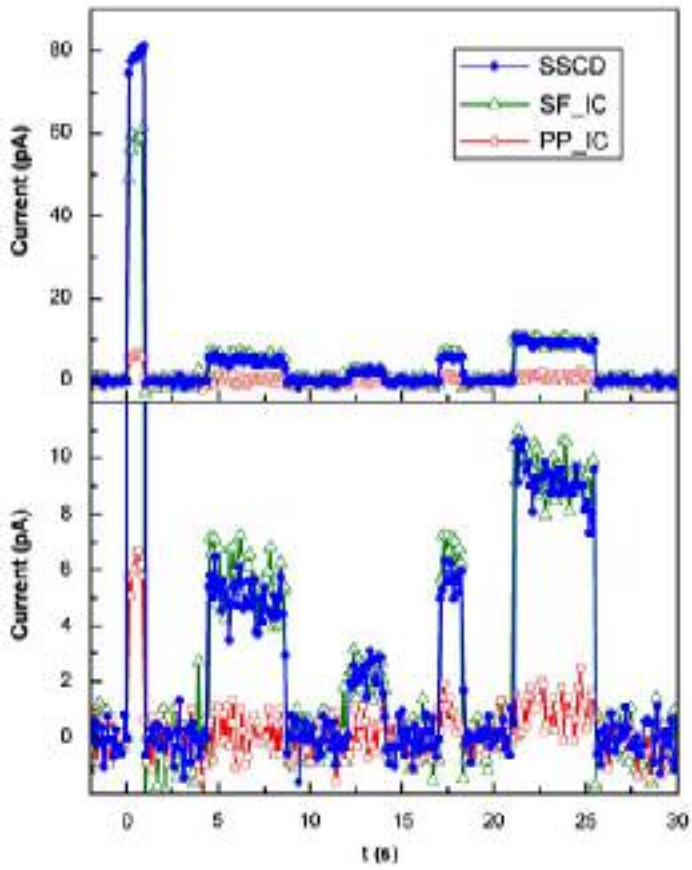

Fig. 5.20 (up) Total current signal obtained by three dosimeters during the complex beam B1 at position a (isocenter). (down) Magnification of the three signals.

No significant difference in the response times is observed among the three dosimeters, demonstrating the fast response time of the SSCD dosimeter and the complete absence of persistent currents and memory effects, often observed in poor quality diamond based detectors [4]. As for the SSCD device sensitivity, it is found that, despite its smaller sensitive volume and the 0 V bias voltage operating conditions, the obtained value is much higher than the PP-IC one (about 9 times higher) and comparable to the SF-IC one. In particular, the lower intensity irradiation segments of the complex beam B1 are hardly detected by the PP-IC. This is even more evident in the lower part of Fig.5.20(down), where a magnification of the three current signals is reported, showing a much lower signal-to-noise ratio from PP-IC with respect to the ones obtained from both the SSCD and the SF-IC dosimeters.

It should be pointed out that for IMRT applications *the reference dosimeter is the* PP-IC [12], being the SF-IC not suitable when high dose gradients are present, due to its relatively large sensitive volume. This is particularly evident in Fig.5.21, where the normalized current response of the three detectors is compared during the entire duration of the complex beam "B2" at the isocenter. These data show that the PP-IC and SSCD signals are essentially superimposed, while the SF-IC one is slightly apart from the others, being lower in the second segment and higher in the third and fifth.

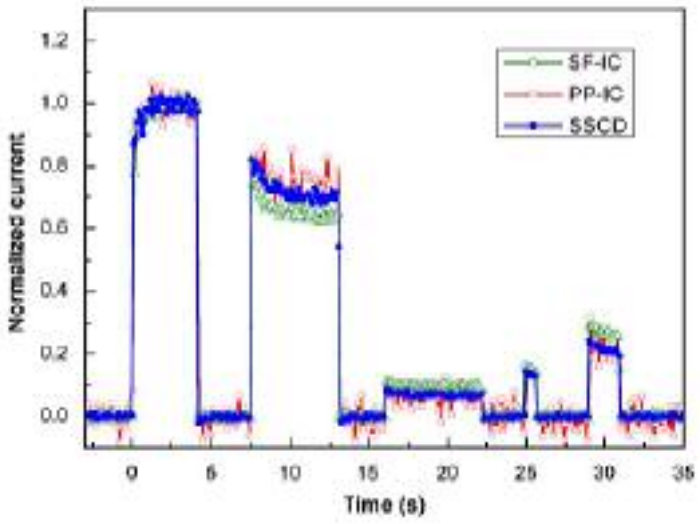

Fig.5.21 Comparison among the SSCD (circles), PP-IC (squares), SF-IC (triangles) normalized signals during the complex beam "B2" at the isocenter. The SSCD and PP-IC signals are quite superimposed, while the SF-IC signal is slightly displaced in some cases.

Such segment is characterized by different dose profiles and dose gradients, so that the response from the larger SF-IC is affected by dose averaging effects, resulting in a higher uncertainty in the local dose determination.

Finally, the total delivered dose was measured in the nine positions using all the available devices. In order to do that, the whole IMRT treatment irradiation was repeated for each detector in each of the examined positions.

The results are summarized in the upper part of Fig.5.22, where the measured doses (normalized respect to the isocenter) are reported. A good agreement between the SSCD (red circles) and the PP-IC reference dosimeter (black triangles) has been obtained in

each position. On the contrary, some discrepancies between the PP-IC and the other dosimeters are observed. This is shown better in the lower part of Fig.5.22, where the percentage deviation from the PP-IC response is reported for all the dosimeters in each of the nine examined positions.

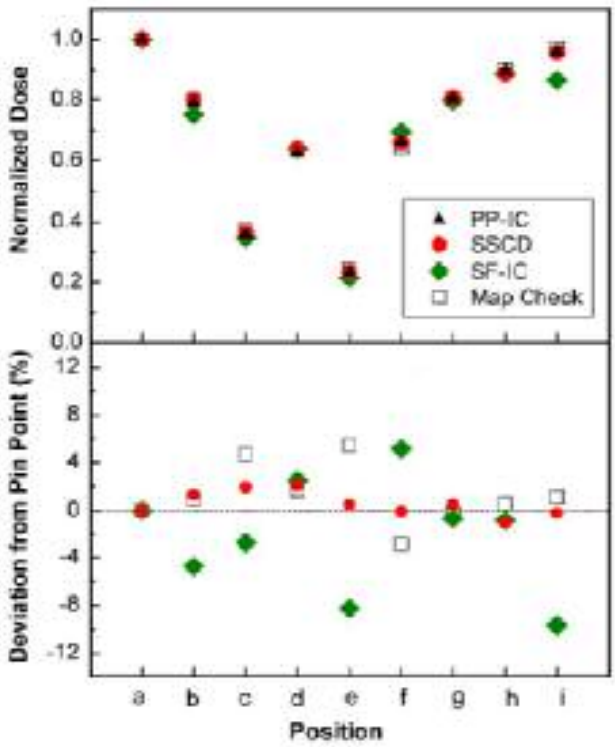

Fig5.22(up) Delivered doses in each of the nine examined positions as measured by the tested dosimeters and the MapCheck during the whole IMRT treatment. The dose values are normalized with respect to the isocenter (position a). (down) Percentage deviation of all the examined detectors from the PP-IC measured dose.

The SSCD signal shows a maximum deviation of about 2% compared with the PP-IC detector. It is worth to point out that such a deviation includes eventual device repositioning errors, which are estimated to be of the order of ±0.5 mm. However, higher deviations are observed for the SF-IC and the MC , which are found to be as high as 10 % and 5% respectively.

Bibliography

[1] A. Boyer, E.B. Butler, T.A. Di Petrillo, M.J. Engler, B. Fraass, W. Grant III, C.C. Ling, D.A. Low, T.R. Mackie, R. Mohan, J.A. Purdy, M. Roach, J.G. Rosenman, L.J. Verhey, J.W. Wong, Int. J. Radiat. Oncol. Biol. Phys. 51 (2001) 880.

[2] P.W. Hoban, M. Heydarian, W.A. Beckham, A.H. Beddoe, Phys. Med. Biol. 39 (1994)1219.

[2] S. Webb, Br. J. Radiol. 76 (2003) 678.

[3] S. Webb, Phys. Med. Biol. 51 (2006) 403.

[4] C. De Angelis, S. Onori, M. Pacilio, G.A.P. Cirrone, G. Cuttone, L. Raffaele, M.Bucciolini, S. Mazzocchi, Med. Phys. 29 (2002) 248.

[5] Y. Garino, A. Lo Giudice, C. Manfredotti, M. Marinelli, E. Milani, A. Tucciarone, G.Verona-Rinati, Appl. Phys. Lett. 88 (2006) 151901.

[6] D. Tromson, C. Descamps, N. Tranchant, P. Bergonzo, M.Nesladek,A. Isambert, Phys. Stat. Sol. (a) 203,12, (2006) 3161.

[7] Absorbed dose determination in external beam radiotherapy: an international code of practice for dosimetry based on standard absorbed dose towater, TRSN. 398 IAEA,n Vienna, 2000.

[8]http://www.ptw.de/1818.html?&no_cache=1&tx_bitptwdwlplus_pi1[id]=data_2&tx_bitptwdwlplus_pi1[pdf]=9f75f45ac34940c128ecbeb5fd3ab4a7 p.20

[9] S. Almaviva, Marco Marinelli, E. Milani, G. Prestopino, A. Tucciarone, C. Verona, G. Verona-Rinati, M. Angelone, M. Pillon, Diamond Relat. Mater. 18, 101, (2009).

[10] D. Letourneau, M. Gulam, D. Yan, M. Oldham, J.W. Wong, Radiother. Oncol. 70, 199, (2004).

[11] S. Almaviva, I. Ciancaglioni, R. Consorti, F. De Notaristefani, C. Manfredotti, Marco Marinelli, E. Milani, A. Petrucci, G. Prestopino, C. Verona, G. Verona-Rinati, Nucl. Instrum. Methods A 608 (2009) 191.

[12] C. Martens, C. De Wagter, W. De Neve, Phys. Med. Biol. 45 (2000) 2519.

Chapter 6

CONCLUSION

The work presented in this thesis shows a CVD single crystal diamond dosimeter in a p-type/intrinsic/metal layered configuration characterized and employed for applications in radiotherapy. The device was tested with no external bias voltage applied. After a pre-irradiation procedure, which is needed to stabilize the device response, sensitivity fluctuation lower than ±0.5% was observed as a function of irradiation time and dose rate over the whole CLINAC DHX Varian accelerator energy range and beam quality. No persistent photocurrents or memory effects were observed in the device response and an excellent linear correlation of the dosimeter output was observed with the delivered dose. The device sensitivity was found to be about 1 nC/Gy, which is comparable to the typical sensitivity of conventional small ionization chambers. The diamond device was tested in a motorized water phantom and connected to an acquisition system commonly used in radiotherapy in order to measure X-ray and electrons dose profiles in water. A very good agreement between the signals from the diamond device and the reference ionization chambers was observed both in the prelimary tests and in the real IMRT treatment plan. During the prelimary tests the SSCD dosimeter showed a higher spatial resolution, a good sensitivity and no need of any correction of its response, while during the IMRT treatment it showed a fast response times comparable with those of both PP-IC and SF-IC detectors. The dose delivered during the prostate cancer IMRT treatment was measured in nine different positions in the water phantom and compared with those measured by the PP-IC, SF-IC and MC commercial devices. A maximum deviation of 2 % from the normalized dose of the reference PP-IC was observed in the case of the SSCD.

The above results indicate that the SSCD dosimeter can successfully be used for application in radiotherapy, possibly overcoming the limitations that prevent the widespread diffusion of diamond-based devices in this field, in particular the long delivery time and high cost of the natural diamond-based devices and the poor dosimetric properties of the polycristalline diamond-based devices.